

NASA
CR
3297
c.1

NASA Contractor Report 3297

LOAN COPY RECD
APW-TECHNICAL
KIRTLAND AFB, NM
0062055

0062055



TECH LIBRARY KAFB, NM

Sensor for Measuring Instantaneous Angle of Attack of Helicopter Blades

P. S. Barna

GRANT NSG-1143
JUNE 1980

NASA



0062055

NASA Contractor Report 3297

Sensor for Measuring Instantaneous Angle of Attack of Helicopter Blades

P. S. Barna

*Old Dominion University Research Foundation
Norfolk, Virginia*

Prepared for
Langley Research Center
under Grant NSG-1143



National Aeronautics
and Space Administration

**Scientific and Technical
Information Office**

1980

SUMMARY

Systematic investigations were performed on a variety of probes to determine their potential for possible application as sensors attached to helicopter blades to measure both the instantaneous angle of attack as well as the dynamic head during actual flight operations. After some preliminary considerations a sensor of essentially spherical shape, about 30 mm in diameter, was designed. The sensor was provided with three pressure ports, and it housed two pressure transducers required for sensing the prevailing pressures acting outside on the surface.

The sensors were subsequently tested in the laboratory under a variety of flow conditions to determine their aerodynamic characteristics. Two series of tests were performed: in the first series the sensor was fixed in space while exposed to steady uniform flow, while in the second series the sensor was made to oscillate, thus simulating the cyclic pitch change of the helicopter blades. While the cyclic pitch frequencies were of about the same magnitude as encountered in flight, the flow velocities during tests fell well below those experienced in a rotating blade. The tests showed that the sensors performed satisfactorily under low subsonic flow conditions with frequencies not exceeding five Hz.

After conclusion of the testing program, some consideration was given to developing theories to predict the performance of the sensor under a variety of flow conditions. The theories appear satisfactory and compare favorably with experimental results at low subsonic speeds. However, the case for higher subsonic velocities experienced under actual flight conditions remains unresolved.

INTRODUCTION

In the field of aeronautical research there are various devices commonly employed to establish flow velocity and its direction from the prevailing pressure measurements. In addition to the well-known pitot tube, used to measure velocity only, there are a variety of tubes, cones and spherical-head sensors which will also measure the flow direction. Most of the existing designs, however, are suitable only for steady flow conditions, that is when the flow properties remain unchanged long enough for observations to be made at leisure (refs. 1 to 7).

In aerodynamic research pertaining to the flow field around helicopter blades one requires sensors capable of very quickly establishing the prevailing pressure with minimum time delay and with high accuracy. More particularly, the problem presented was to design and test a sensor capable of measuring the instantaneous angle of attack and the dynamic head at a certain location of a helicopter blade under actual flight conditions. In addition to the requirement of rapid pressure readings, the design was required to be adequately strong to withstand high rates of accelerations, adequately rigid to move together with the blade with minimum deflection, and light enough to add only a minimum amount of weight without causing interference with the blade motion.

To achieve the desired results, consideration was given to employing miniature pressure transducers capable of operating in the low-pressure range, rugged to withstand high accelerations, and also reliable under a wide range of operating temperatures. Such a transducer would be placed inside the probe in the immediate vicinity of the pressure-sensing ports in order to reduce the length of passages between the ports and the transducers. Placing the transducers inside the head permitted sensing of the pressure at the nearest point of application and allowed transmission of the electrical signal to a remote location where the amplifiers could be set up conveniently.

LIST OF SYMBOLS

a	radius of spherical sensor head
b	sphere coefficient for a real fluid flow
b_o	sphere coefficient for ideal flow, $b_o = 2.25$
b_{12}, b_{23}	sphere coefficients based on measurements
C_{p_i}	pressure coefficient at point i on the surface of a sphere defined as $(p_i - p)/1/2 U^2$
f	frequency, Hz
g	gravitational acceleration, 9.81 m/s^2
L	distance between the sensor head front end to the center of oscillation
p	static pressure at porthole
P_t	total pressure
P	free-stream static pressure
ΔP	pressure differential
ΔP_{ij}	pressure differential between two points i and j
$\Delta P_{12}, \Delta P_{23}$	pressure differentials between portholes 1, 2 and 2, 3, respectively
q	dynamic pressure head, $q = 1/2 \rho U^2$
r	radial direction in the spherical coordinates
R_e	Reynolds number based on sphere diameter, m
S	stagnation point
t	time, s
U	free airstream velocity, m/s
U_r	relative velocity

u, v, w	instantaneous velocity components in x, y, and z directions, respectively
v_t	sensor tangential velocity under oscillating motion, m/s
X, Y, Z	Cartesian coordinates
α	half of the amplitude angle, degrees
β	angle due to rotation of sphere about z axis, degrees
η	instantaneous change of angle due to the sensor's oscillating motion
η_r	relative η
η_r^*	combined relative angle
θ	sensor position angle, degrees
θ_D	displacement angle, degrees
θ_L	lowermost sensor position angle, degrees
θ_U	uppermost sensor position angle, degrees
$\theta_1, \theta_2, \theta_3$	angle between undisturbed free-stream velocity and porthole number 1, 2 or 3, respectively, on the spherical head
μ	dynamic viscosity
ρ	density
ϕ	velocity potential
ψ	stream function
ω	angular velocity

Subscripts

1	porthole one
2	porthole two

3 porthole three
 i,j location of a point on a sphere
 r relative
 t tangential
 U upper extreme position of sensor during a stroke
 L lower extreme position of sensor during a stroke

THEORETICAL CONSIDERATIONS

Application of Steady Potential Theory of Flow Past a Fixed Spherical Object for the Determination of Flow Velocity and Direction

The pressure distribution around a truly spherical object under incompressible steady-flow conditions is given by the relation (ref. 8):

$$p_i - p_\infty = (1 - b_o \sin^2 \theta_i) 1/2 \rho U^2 \quad (1)$$

where the angle θ is measured from the stagnation point S located at the front of the sphere as shown in figure 1(a). This relation is derived from potential flow theory, which yields for the sphere constant b_o the exact value of 2.25.

Since stagnation pressure

$$p_t = p_\infty + 1/2 \rho U^2 \quad (2)$$

Equation (1) may be written as

$$p_i = p_t - b_o q \sin^2 \theta_i \quad (3)$$

where $q = 1/2 \rho U^2$ is the dynamic head of the approaching flow.

In order to establish the magnitude and direction of the flow, it is required to provide three pressure ports on the meridian circle of the spherical object - if employed as a sensor. It is convenient to locate port 1 as the center, while two side ports, 2 and 3, are at equal distance (equal central angles) on each side of the central port 1, as shown in figure 1(b).

It is also useful to assign 90 degrees for the enclosed angle between ports 2 and 3, thus making $\theta_2 + \theta_3 = \pi/2$. Assuming that the flow approaches the sphere at angle $\theta = \theta_1$, as shown in figure 1(c), for Port 1 we write

$$p_1 = p_t - b_o q \sin^2 \theta_1$$

and for ports 2 and 3

$$p_2 = p_t - b_o q \sin^2 \theta_2$$

$$p_3 = p_t - b_o q \sin^2 \theta_3$$

Thus the pressure difference between ports 2 and 3 becomes

$$\Delta p_{23} = b_o q (\sin^2 \theta_3 - \sin^2 \theta_2) \quad (4)$$

and between ports 1 and 2

$$\Delta p_{12} = b_o q (\sin^2 \theta_2 - \sin^2 \theta_1) \quad (5)$$

When the flow approaches the sphere at angle θ , measured from the center port 1, then from geometry: $\theta_3 + \theta = \theta_2 - \theta$ [see fig. 2(b)] and

$$\theta = 1/2(\theta_2 - \theta_3) \quad (6)$$

Employing the identity

$$\sin^2 \theta_i - \sin^2 \theta_j = \sin(\theta_i + \theta_j) \sin(\theta_i - \theta_j)$$

one obtains for $\theta_i = \theta_2$ and $\theta_j = \theta_3$

$$\sin^2 \theta_3 - \sin^2 \theta_2 = \sin 2\theta \quad (7)$$

Similarly, since $\theta_2 = \pi/4 - \theta_1$,

$$\sin^2 \theta_2 - \sin^2 \theta_1 = \frac{1}{\sqrt{2}} \sin \left(\frac{\pi}{4} - 2\theta \right) \quad (8)$$

Substitution of equation (7) into equation (4) leads to

$$\Delta p_{23} = b_o q \sin 2\theta \quad (9)$$

and substitution of equation (8) into equation (5) leads to

$$\Delta p_{12} = b_o q \frac{1}{\sqrt{2}} \sin \left(\frac{\pi}{4} - 2\theta \right) \quad (10)$$

Expanding equation (10) and substituting into equation (9) yields

$$\cos 2\theta = \frac{1}{q b_o} (\Delta p_{23} + 2\Delta p_{12}) \quad (11)$$

Upon dividing equation (9) with equation (11), q and b_o cancel and one obtains

$$\tan 2\theta = \Delta p_{23} / (\Delta p_{23} + 2\Delta p_{12})$$

Thus the flow angle for potential flow is

$$\theta = \frac{1}{2} \tan^{-1} \left\{ \Delta p_{23} / (\Delta p_{23} + 2\Delta p_{12}) \right\} \quad (12)$$

With the flow angle θ thus obtained, the dynamic head q can be calculated by employing either equation (9) or (10).

Application of Unsteady Potential Theory to Flow Past a Spherical Object

A spherical object attached to a helicopter blade as a sensor must follow the blade's cyclic motion. The periodic motion of the sensor superimposed on the steady flow towards the sensor results in unsteady flow. It is anticipated that the sensor will be attached to the blade with a short sting support, hence the oscillating periodic motion of the sensor will take place on a circular arc relative to the blade. The flow model thus essentially consists of a sensor of spherical shape subjected to cyclic motion while immersed into a steady flow as shown in figure 2.

The motion of the sensor may be resolved into translation and rotation. The translation, in turn, may be further resolved into a horizontal (x) and vertical (y) component. Accordingly, the speed of translation has a horizontal (u) and a vertical (v) velocity component, which, added to the rotational velocity, leads to the solution for the momentary pressure distribution under unsteady flow. Rotation takes place about the z axis, as shown in figure 3.

It may be shown that under unsteady flow the pressure in a fluid at any point is generally given by (refs. 9, 10, 11)

$$p(x, t) = p_{\infty} - \rho \left[\frac{\partial \phi}{\partial t} + \frac{1}{2} (\nabla \phi)^2 \right] \quad (13)$$

where the time-dependent velocity potential ϕ for an axisymmetric motion is

$$\phi = \phi(r, \phi, t).$$

The solution for ϕ is known to be

$$\phi = -u(t) a^3 \cos \theta / 2r^2 \quad (14)$$

The instantaneous horizontal speed component $u(t)$ may be resolved into

$$u_\theta = \frac{1}{r} \frac{\partial \phi}{\partial \theta} \quad \text{and} \quad u_r = \frac{\partial \phi}{\partial r}$$

Hence

$$u_\theta = \frac{u(t)a^3}{2r^3} \sin \theta \quad \text{and} \quad u_r = \frac{u(t)a^3}{r^3} \cos \theta$$

On the surface $r = a$ and $u_r = 0$; hence the contribution of u to the instantaneous pressure at point i on the surface becomes

$$p_i(a, \theta_i, t) = p_\infty + \frac{1}{2} \rho \left[\frac{u^2}{4} (q \cos^2 \theta_i - 5) - a \frac{du}{dt} \cos \theta_i \right] \quad (15)$$

Between ports i and j the instantaneous pressure differential (due to u) becomes

$$\Delta p_{i,j}(u) = \frac{1}{2} \rho \left[\frac{q}{4} u^2 (\cos^2 \theta_i - \cos^2 \theta_j) - a \frac{du}{dt} (\cos \theta_i - \cos \theta_j) \right] \quad (16)$$

Similarly, the contribution of the vertical speed component v to the instantaneous pressure on the surface becomes

$$p(a, \theta'_i, t) = p_\infty + \frac{1}{2} \rho \left[\frac{v^2}{4} (q \cos^2 \theta'_i - 5) - a \frac{dv}{dt} \cos \theta_i \right] \quad (17)$$

hence the pressure difference between ports i and j (due to v) becomes

$$\Delta p_{i,j}(v) = \frac{1}{2} \rho \left[\frac{q}{4} v^2 (\cos^2 \theta'_i - \cos^2 \theta'_j) - a \frac{dv}{dt} (\cos \theta'_i - \cos \theta'_j) \right] \quad (18)$$

Rotation of the sphere results in an instantaneous surface velocity $a(d\beta/dt)$ which must be resolved into the x and y directions. If rotation alone is considered, the relative angle η_r enclosed between the main flow direction and the resulting relative velocity V_r is given by

$$\eta_r = \tan^{-1} \left\{ \frac{a \frac{d\beta}{dt} \cos \beta}{U + a \frac{d\beta}{dt} \sin \beta} \right\} \quad (19)$$

while the dynamic head of the relative velocity becomes

$$q_r = \frac{1}{2} \rho V_r^2 = \frac{1}{2} \left[\left(U + a \frac{d\beta}{dt} \sin \beta \right)^2 + \left(a \frac{d\beta}{dt} \cos \beta \right)^2 \right] \quad (20)$$

Hence the pressure differential between ports i and j (due to rotation) becomes

$$\Delta p_{i,j}(\beta) = b_o q_r \left[\sin^2(\beta_j + \eta_r) - \sin^2(\beta_i + \eta_r) \right] \quad (21)$$

In order to combine the effects of translation and rotation, a combined relative angle η_r^* may be found which includes the horizontal, vertical, and rotational instantaneous velocities. This may be attained by adding all horizontal and vertical velocities, as shown in figure 3, and thus the relative angle becomes

$$\eta_r^* = \tan^{-1} \left\{ \frac{v + a \frac{d\beta}{dt} \cos \beta}{U + u + a \frac{d\beta}{dt} \sin \beta} \right\} \quad (22)$$

Similarly, the combined relative dynamic head must include all components; hence

$$q^* = \frac{1}{2} \rho \left[\left(U + u + a \frac{d\beta}{dt} \sin \beta \right)^2 + \left(a \frac{d\beta}{dt} \cos \beta \right)^2 \right] \quad (23)$$

Finally, the combined pressure differential between ports i and j becomes

$$\Delta p_{i,j}^* = b_o q^* \left[\sin^2(\beta_j + \eta^*) - \sin^2(\beta_i + \eta^*) \right] \quad (24)$$

With these relations a computer program can be written to calculate η^* , q^* and $\Delta p_{i,j}^*$.

Method of Simple Superposition of Velocity Vectors

A different method from the potential flow theory is obtained by the simple superposition of the instantaneous sphere velocity due to its oscillation with the oncoming free flow. (Figure 2 shows a spherical sensor fitted to a sting oscillating about an axis of symmetry $o-o'$ with its center of oscillation located at o' .) At any port i on its surface, the relative velocity v_r will be the resultant of the free-stream velocity U and the instantaneous tangential velocity v_t . For a given instantaneous angle θ :

$$v_t = L \frac{d\theta}{dt}$$

Thus the resultant velocity v_R becomes

$$v_r = \left[(U + v_t \cos \theta)^2 + (v_t \sin \theta)^2 \right]^{1/2} \quad (25)$$

and the relative angle of incidence

$$\eta = \tan^{-1} \left\{ \frac{v_t \sin \theta}{U + v_t \cos \theta} \right\} \quad (26)$$

Thus the instantaneous angle of attack enclosed (at i) between V_r and the axis of symmetry becomes

$$\alpha_i = \theta + \eta \quad (27)$$

Assuming that pressure varies with time as the probe oscillates (that is, the pressure distribution on the sphere adjusts instantaneously to the velocity changes), then

$$p_i = p_t - b_o q(t) \sin^2 \alpha_i \quad (28)$$

where both the dynamic head $q(t) = 1/2 \rho V_r^2$ and the angle α_i are time dependent. Thus the time-dependent pressure differential between ports i and j becomes

$$\Delta p_{i,j} = b_o q(t) (\sin^2 \alpha_j - \sin^2 \alpha_i) \quad (29)$$

Sinusoidal Oscillations

In order to illustrate the potential flow solution, let us first assume sinusoidal oscillations and let

$$\theta(t) = \theta_0 - \alpha \sin(2\pi ft) \quad (30)$$

Assuming that the port is at radius L from the center, one obtains the translational components

$$u = V_t \sin \theta = L \frac{d\theta}{dt} \sin \theta \quad (31)$$

$$v = V_t \cos \theta = L \frac{d\theta}{dt} \cos \theta \quad (32)$$

The assumption of sinusoidal motion leads to simple solution.

Deviation from Potential Flow Theory

Since viscosity enters "real" flow problems, it is anticipated that boundary-layer buildup and time delays may change the results predicted from potential flow theory. Since the ports are located at the front portion of the sphere, the effects of boundary-layer buildup and separation on the pressure distribution are less marked there than at the rear. Therefore, for the front of the sphere, under steady flow conditions, one may assume a "quasi-potential" flow solution which would predict the pressure distribution defined by equation (3) with the exception that the sphere constant b_0 , calculated with the ideal flow, would be replaced by real b . More particularly, assuming that $b = b_{23}$ for p_{23} and $b = b_{12}$ for p_{12} , one obtains by equations (9) and (10)

$$\Delta p_{23} = b_{23} q \sin 2\theta \quad (33)$$

and

$$\Delta p_{12} = b_{12} q \frac{1}{\sqrt{2}} \sin \left(\frac{\pi}{4} - 2\theta \right) \quad (34)$$

Upon expanding equation (34) and combining with equation (33) one obtains

$$\cos 2\theta = \frac{1}{q} \left(\frac{\Delta p_{23}}{b_{23}} + 2 \frac{\Delta p_{12}}{b_{12}} \right) \quad (35)$$

Upon dividing equation (33) with equation (35) one obtains

$$\tan 2\theta = \frac{\Delta p_{23}}{\Delta p_{23} + 2 \frac{b_{23}}{b_{12}} \Delta p_{12}} \quad (36)$$

thus

$$\theta = \frac{1}{2} \tan^{-1} \left\{ \frac{\Delta p_{23}}{\Delta p_{23} + 2 \frac{b_{23}}{b_{12}} \Delta p_{12}} \right\} \quad (37)$$

In comparing equation (37) with equation (12), one finds that in potential flow the angle θ depends only on the pressure differences Δp_{23} and Δp_{12} , while in the quasi-potential flow it also depends on the value of the sphere constants b_{23} and b_{12} .

Time delays are anticipated to affect the pressure differences calculated with the unsteady potential flow theory. These delays are attributed to inertia effects of the boundary layer, and the discrepancy between theory and practice becomes large at higher frequencies.

The velocity distribution near an oscillating wall has been treated by Stokes and Raleigh (ref. 11), and similar consideration may apply to the motion of the oscillating sphere. Accordingly, owing to the no-slip condition at the wall, the fluid velocity there must equal that of the wall. Therefore, the motion of the first layer nearest the wall must assume the instantaneous velocity of the sphere, while other layers built upon the first one suffer a delay because their motion is activated only by the viscosity and the decreasing velocity gradient between adjacent layers. Thus it may be anticipated that when the oscillating sphere, having reached dead end, suddenly changes its direction, the boundary layer keeps moving forward for a short period in the same direction the surface was moving before the change took place. While these phenomena are recognized, they have not been treated analytically because of their complexity.

REASONS FOR EXPERIMENTS

Potential flow theory applies to the flow around a spherical object only if the object is of truly spherical shape all the way around. For the sphere to be employed as a sensor, however, it had to be provided with a support which, in this particular application, was a simple sting attached to the rear. Once the sting was attached to the sphere, it changed the shape of the sphere, and this in turn was dependent on both the thickness and on the length of the support. It was anticipated that the pressure distribution would be affected to some extent also when the sting assumed various angles of attack, the effects of which cannot

readily be predicted from the existing potential flow theory. Therefore it became necessary to perform experiments.

The experiments were divided into two categories: tests under steady and tests under unsteady flow conditions. In the steady flow experiments, the main concern was to check the validity of assumption for quasi-potential flow and to establish the sphere constant values as a function of sting support and Reynolds number. In the unsteady flow tests, the main concern was to study the effects of frequency and free-stream velocity on the pressure differences p_{12} and p_{23} and to establish a practical testing procedure that could be employed under actual flight conditions.

EXPERIMENTS UNDER STEADY FLOW CONDITIONS

Studies of Pressure Distribution

To obtain the pressure distribution, a spherical object of 6.35-cm (2.5-in.) diameter was placed into the airstream. The sphere was made of aluminum and was supported by a horizontal hollow shaft press-fitted into the "side" of the sphere right up to its center. A single pressure tapping was radially drilled into the surface of the sphere at a right angle to the axis of the hollow shaft, the hole also extending to center, as shown in figure 4(a). The shaft was set at a right angle to the airstream, and, by rotating it about its axis, the pressure distribution around the sphere could be obtained. Since the diameter of the shaft was 9.5 mm (0.375 in.), its interference with the airstream was considered minimal; however, it had to be reinforced for rigidity with a sleeve that extended through the tunnel walls. The sleeve fitted into the arbor extending from the turntable and was held in position by set screws. The angle of incidence was measured with a protractor provided with a Vernier scale so that the angle was measured with an accuracy of 0.1 degree.

The pressure experienced on the surface of the sphere propagated through the port to the center from where it was transmitted through the hollow shaft to a sensitive manometer. A pitot-static tube was employed near the sphere to measure the velocity of the stream and to provide the local pressure used as reference to the pressure on the sphere surface.

Two types of experiments were performed. In the first type, the sphere alone was tested at various Reynolds numbers. In the second type of test, the sphere was provided with a "tail" to simulate the sting support. The tail consisted of a hollow circular cylinder located either diagonally opposite the center port or diagonally opposite the side ports. The experiments were first performed at the outlet of the open-end wind tunnel and were subsequently repeated in the closed-circuit wind tunnel. The experimental setup in the closed tunnel is shown in figure 4b, and the setup at exit of the open tunnel is shown in figure 5.

Prior to each test the sphere was visually aligned so that the center hole faced the airstream. To check the accuracy of the visual alignment, the sphere was rotated to an angle, say 10 degrees, and a pressure measurement was taken. Subsequently, it was rotated back into the opposite direction to -10 degrees and the pressure was again recorded. If the center was correctly aligned, the two pressure readings gave substantially the same result. An adjustment was made if the readings proved unequal, and the process was repeated until the desired result was obtained.

To study the effect of the tail, tests were performed with the tail located opposite the center port or opposite either of the two side ports. This was easily achieved by drilling and tapping three holes exactly diagonally opposite the ports located at the face of the sphere. All tests performed with the 4.4 cm (1.75-in.) diameter tail were subsequently repeated with a 3.5-cm (1.375-in.) diameter tail [both tails were 15.2-cm (6-in.) long].

During each test the air velocity was kept constant and the incidence angle was varied by small steps, generally two to five degrees at a time. When the slope of the curves was steep, the increments were only one-half degrees or less as required. Air velocity was varied between 15.2 m/s (50 ft/s) and 70 m/s (200 ft/s), that is, between the Reynolds number range 0.62 to 2.5×10^5 . All test runs were made with the sphere turning in one direction and were repeated in the opposite direction.

RESULTS

The results are presented in four sets of graphs. Figure 6 shows the conventional pressure distribution around 180 degrees of the isolated sphere, and the results are compared with the findings of another investigator (ref. 12). Figures 7 and 8 show results between ± 75 degrees.

Figures 9 and 10 show the pressure distribution between angles ± 75 degrees with the tail located diagonally opposite port 1 (center port) for both tails, 4.4-cm (1.75-in.) and 3.5-cm (1.375-in.) diameter, respectively. Figures 11 and 12 show results of port 2, that is, when the tail was displaced by 45 degrees from the centerline. Figures 13 and 14 show results for port 3 similar to those obtained for port 2, except for the change in the sign of the angles. For both ports the measurements were taken between ± 105 and $+20$ degrees (for port 2 the range was -105 to $+20$ and for port 3, -20 to $+105$ degrees).

It appears from figures 6 to 8 that pressure distribution is sensitive to Reynolds number effects and also to the level of turbulence present in the airstream (ref. 13). However, the magnitude of sensitivity also depends on incidence. Between 0 and 30 degrees the pressure coefficient falls from unity (1.0) to approximately 0.6 for all spheres tested; and, in this range variation, the pressure coefficient proves to be insensitive to viscous effects. With increasing incidence, however, the sensitivity gradually increases and becomes greatest between 50 and 80 degrees. In further increasing the incidence, the sensitivity decreases again and becomes relatively small between 80 and 180 degrees. Furthermore, the sensitivity also manifests itself in a shift of the zero pressure¹, located at the intersection of the pressure distribution curve with the horizontal axis. It was noticed that a marked change in the negative pressure peaks always occurred between 70 and 80 degrees. The shift in the zero pressure point may be observed from inspection of the graphs: at $R_e = 1.4 \times 10^5$ the intersection point is about ± 45 degrees (fig. 7), while the point shifts to 43.6 degrees at $R_e = 2.6 \times 10^5$ as shown in figure 8.

¹ Zero pressure is experienced when the difference between the free-stream pressure and surface pressure decreases to zero.

The presence of the tail substantially lowered the value of $-C_p$ min. With the 3.49-cm tail C_p min = -1.0 at $Re = 0.91 \times 10^5$ (fig. 9a), while -1.15 is experienced at 1.4×10^5 (fig. 9b), and 1.23 at 2.5×10^5 (fig. 9c). With increasing Reynolds number, zero first shifts from ± 44.7 degrees (fig. 9a) to ± 44.5 degrees (fig. 9b), then further decreases to about ± 41 degrees at 2.5×10^5 (fig. 9c). Similar results were found with the 4.4-cm tail (ref. 14).

Experiments conducted at lower Reynolds numbers indicated some instability in the pressure which occurred at ± 50 degrees when the 3.5-cm tail was attached. The manometer oscillated periodically and showed at one time a value of -0.2 and a moment or two later -0.3, and so 2 values appear for the same incidence in figures 9a, and 9b. This instability was not observed in the closed tunnel at $R_e = 2.5 \times 10^5$. With the 4.4-cm tail, instability occurred around 52 degrees at low Reynolds numbers, but no instability was experienced at higher speeds (see figs. 9c and 10b).

Studies on port 2 are shown in figures 11 and 12, where the pressure distribution between angles of -105 and ± 20 degrees is presented. The resulting curves are superimposed for ready identification of the effects of Reynolds numbers ranging between 0.91 to 2.6×10^5 . Peculiarities manifest themselves in the negative pressure range at lower Reynolds numbers; in addition to the shape changes of the curves, the shift in zero pressure angle and the surges resulting from instability, there also appears to be a break in the continuity around 45 degrees. This was observed only in the open tunnel. Once the Reynolds number attained a value of 2.4 to 2.6×10^5 , the pressure distribution curve became rather "regular," free of bumps and surges with the pressure coefficient attaining a minimum value of approximately -1.3 at -90 degrees. To facilitate interpretation of the results, the various positions of the tail relative to the horizontal reference line are also shown in figures 11 and 12. Similar results were obtained for port 3, as shown in figures 13 and 14.

The effects of both viscosity and turbulence level on transition from laminar to turbulent flow in the boundary layer are well known. It is therefore logical to assume that the zero pressure point is also affected by both. Because of the difference of turbulence level between the open and closed tunnels, separate experiments were conducted in the closed tunnel to study the effect of Reynolds number on the location of the zero pressure point. In other words, restricting tests to one tunnel eliminated the influence of turbulence level on transition by the other tunnel.

Results of these experiments are presented in figure 15 where the zero pressure incidence angle is plotted against Reynolds numbers between 0.55 and 2.6×10^5 . It appears that below $R_e = 1.2 \times 10^5$ the changes are small. However, a sudden drop appears at 1.2×10^5 followed by a gradual decrease with increasing Reynolds number. The curves flatten out after $R_e = 1.8 \times 10^5$ and the zero point remains fixed at 41.5 degrees.

APPLICATIONS OF RESULTS

From the pressure distribution tests, the sphere constants b_{23} and b_{12} can be established. This entails the application of the results to a pair of ports, either 1 and 2 or 2 and 3, which need to be located at set angles. It was convenient to fix 45 degrees as the set central angle between ports then the central angle between ports 2 and 3 became a right angle. The procedure for obtaining the sphere constant was first to establish the angles enclosed by the portholes with the airstream when the sphere was set to an incidence θ . For example, when considering side ports 2 and 3, if $\theta = -20$ degrees, then for port 3 the angle $\theta = +25$ degrees and for port 2, $\theta = -65$ degrees. Second, for these angles the pressure coefficient C_p was found from the experimental results. Thus at $R_e = 2.6 \times 10^5$ the coefficients $C_{p2} = -0.85$ and $C_{p3} = +0.61$ were found. Their difference $\Delta C_{p23} = C_{p2} - C_{p3} = -1.46$. The procedure was repeated for incidence angles ranging from -30 to +30 degrees in convenient (5-degree) steps. For convenience, table 1 gives the values of θ_1 , θ_2 ,

θ_3 at various incidences. Finally, the resulting ΔC_{p23} values were plotted against $\sin 2\theta$ for the side ports 2 and 3 as shown in figure 16, and ΔC_{p12} values were plotted against $\frac{1}{\sqrt{2}} \sin(45 - 2\theta)$ for the side ports 1 and 2, as shown in figure 17. The sphere constants were obtained from the slopes of the curves.

It appears from figure 16 that for side ports 2 and 3 and with the 4.4-cm tail, the sphere constant $b_{23} \approx 2.25$ at the high Reynolds number of 2.6×10^5 , a result which completely agrees with the value of 2.25 predicted from potential flow theory. At the same Reynolds number, the center and side port constant $b_{12} \approx 2.23$, which is a value only 0.9 percent off 2.25. For lower Reynolds numbers, however, the sphere constants assume lesser values, depending on the Reynolds number, as shown in figures 16 and 17.

In the determination of the sphere constant b_{12} , only the linear portion of the curve was used. As it appears from figure 17, the top end of the curves turn around and form a loop, and the size of the loop seems to depend on the Reynolds number. It is noted that the function $\sin(45 - 2\theta)$ attains a maximum value of 1 when the angle $\theta = -22.5$ degrees, so the extreme of the horizontal abscissa ends at $\frac{1}{\sqrt{2}} = 0.707$. Since the experiments were conducted with angles up to 30 degrees, all angles below -22.5 degrees will cause the function $\sin(45 - 2\theta)$ to have values inboard of the extreme; hence b_{12} may not be considered constant below -22.5 degrees.

Test on Spherical Probes Equipped with Transducers

While the tests performed on the larger 6.35-cm (2.5-in.) spherical object were aimed to study the pressure distribution around the meridional plane, the tests of the smaller, 3.2-cm (1.25-in.) spherical sensor were aimed at finding how close the complete sensor unit equipped with pressure transducers would agree with the pressure distribution obtained on the larger spherical object.

The pressure transducer and sensor design received thoughtful attention, and the ultimate selection was the Patterson gage (ref. 15), a small device which essentially consists of a variable air-gap inductance

type of electrical pressure gage of cylindrical shape, about 1.2 cm (0.5 in.) in diameter and about 1-cm (0.4-in.) thick, capable of measuring pressure fluctuations at fairly high frequencies by using stretched flat diaphragms. Patterson gages were chosen because they were found compact and rugged as well as being insensitive to temperature changes. The effect of an accelerating force normal to the diaphragm is claimed to be of the order of one percent of full scale per 100 g.

Two Patterson gages were employed inside the spherical head. One measured the pressure differences $p_1 - p_2$ between ports 1 and 2 and the other measured $p_2 - p_3$ between ports 2 and 3 respectively, as shown schematically in figure 18(a). Each gage fitted snugly into a machined recess of the spherical "head." The head and its cylindrical support (sting or tail) were carefully machined; there were three separate pieces making up the head, which were fitted together making one unit after the gages were placed into their respective places, as shown in figure 18(b). The electrical leads were permitted to leave at the end of the support which was held by a massive, cylindrical holder. Each face of the gage was hermetically sealed against any possible air leak with suitable O rings. The diameter of the ports was 0.343 mm (0.0135 in.), and the central angle enclosed between ports was 45 degrees. A photograph of the sensor is shown in figure 18(c).

The Equipment Employed for Steady-Flow Testing of the Spherical Sensor

A special induction tunnel was constructed for the steady flow testing of the spherical sensor. It consisted of a bell-mouth intake, parallel test section, and diffuser leading to the suction side of a centrifugal fan (blower), which was driven by a 4-speed electric motor rated 11 kW (15 HP). The test section was built of 2.54-cm (1-in.) thick, clear plastic with internal dimensions of 15.2×20.3 cm (6 × 8 in.) with a length of 30.5 cm (12 in.). A honeycomb was placed into the intake to reduce fluctuations of the approaching stream, and at outlet a foam rubber isolator was inserted between the diffuser and the fan to prevent

vibration. The air flow was induced by suction, and air speeds up to 92 m (300 ft)/s could be obtained. A schematic plan of this small tunnel is shown in figure 19(a).

The sensor was held inside the test section by a vertical support which interconnected two turntables. These tables consisted of two circular discs situated opposite each other which fitted flush into the recessed top and bottom of the test section with their axis being concentric. The vertical support fastened to each disc was eccentrically located, and the eccentricity was about 10 cm (4 in.). The two discs could be turned together from the outside of the tunnel by a pair of lever arms which were connected by a handle outside the tunnel. The arms were long enough to clear the walls allowing angles of turning up to ± 32 degrees. Details of the test section are shown in figure 19(b), and a photograph of the tunnel is shown in figure 19(c).

Results of Tests on Spherical Sensor Under Steady-Flow Conditions

Prior to the tests on the sensors, the transducers were calibrated. This simple procedure essentially consisted of setting up a pressure difference between a chamber and ambient air pressure. By accurately measuring this pressure differential with a standard manometer simultaneously with the pressure transducer a calibration was obtained. The transducer gage was connected to a carrier and amplifier unit, and a 2-channel BRUSH 220-type chart recorder was employed to obtain the pressure difference signals in terms of mV on a strip chart. A sample record is shown in figures 20(a) and (b). It appears that the curve obtained shows linearity between $\pm 2 \text{ N/m}^2 \times 10^3$.

The tests were performed on sensors in the induction tunnel at various speeds and at angles varying between -22 to +32 degrees. The results are shown in figure 21, where the nondimensional pressure differential $\Delta p_{23}/q$ and $\Delta p_{12}/q$ are plotted against incidence in the range of Reynolds numbers 0.473 to 1.86×10^5 . While the results for Δp_{23} shown in figure 21(a) are very close to the theoretical "sphere" coefficient, $b_{23} = 2.25$, the results shown in figure 21(b) for $\Delta p_{12}/q$ are about 18 percent lower, resulting in $b_{12} \approx 1.85$.

EXPERIMENTS WITH OSCILLATING SENSOR

Details of the Wind Tunnel and Oscillating Mechanism

The wind tunnel employed for testing the 3.2-cm sensor was an open-ended, straight through-flow tunnel with a contraction ratio of 4.7:1. It essentially consisted of a large air intake, with an axial flow fan followed by a diffuser and a well-shaped contraction. The fan was driven by an 11-kW (15-HP) motor directly with a floating shaft arrangement that permitted the air to enter without any obstruction. A honeycomb and a screen were fitted across the largest cross section of the tunnel, thus producing a low turbulence stream at exit. Details of the tunnel are shown in figure 22.

For the purpose of the experiments described in this report, the tunnel exit was provided with a transform duct changing the circular cross section to rectangular shape; this was followed by a short parallel duct to which the steel frame holding the oscillating mechanism was fitted. A short flexible wall, inserted between the exit and the parallel duct, served as a vibration isolator.

The mechanism producing the oscillatory motion essentially consisted of a Scotch Yoke, a mechanism in which the circular motion of a pivot is transformed into a reciprocating motion. The pivot is usually inserted into an elongated slot cut into a crosshead and provided with two parallel guides. As the pivot rotates, it translates sideways in the slot while the slot translates parallel with itself. To obtain even speed the drive system was provided with a disc acting as a flywheel. A T-shaped groove was diagonally milled into the flywheel, and into this groove a sliding nut was fitted to which the pivot was mounted. By changing the position of the nut relative to the center of rotation of the flywheel, the radius of the circulatory motion of the pivot acting as a crank could be varied, and with this mechanism the amplitude of the oscillations could be varied. In addition it was found necessary to provide the mechanism with two springs, thus providing a counterbalance to the weight of the crosshead in the experimental setup. The Scotch Yoke mechanism was actuated by a

373-W (0.5-HP) variable speed electric motor through a vee belt drive. The reciprocating motion from the yoke was transferred to a cylinder horizontally stretched across the tunnel section to which the sensor was attached by a holder. While the yoke produced a reciprocating motion, the cylinder oscillated about its own axis. This motion was attained by employing a lever-arm attached to the cylinder that was actuated by the yoke at one end, while a vertical link pivoted to the other end actuated the lever arm attached to the cylinder, as shown in figure 23. The system was capable of producing oscillations up to 12 Hz. In order to measure the variation of the displacement angle θ with time, a potentiometer was fitted to one end of the oscillating cylinder. A view of the Scotch Yoke mechanism is shown in figure 24, and a complete view of the test rig fitted to the end of the open tunnel is shown in figure 25.

Method of Testing

The transducers built into the sensor were first electrically balanced allowing a one-hour warming up period for the amplifying system. After the sensors were fitted into the holder of the oscillating cylinder, the extreme angles θ_U and θ_L were set up by manually turning the drive shaft. When the dead end positions were reached, a clinometer was placed on the sensor and the angle of incline was measured with an accuracy of ± 0.1 degree. The instantaneous pressure responses of the transducers $\Delta p_{23} = p_2 - p_3$ and $p_{12} = p_1 - p_2$ were recorded on channel one, while the instantaneous displacement angle was recorded on channel two. Prior to running the tests the reference lines were established by running the strip chart for a short period of time.

From the strip chart passed out by the recorder the frequency was determined from the linear speed of the paper. Intersection of the undulating line with the paper grid helped to determine the instantaneous angle of oscillation while the other two lines determined the instantaneous pressure differentials. A sample of such a record is shown in figure 20.

The experiments were performed either by setting the air speed constant and varying the frequency or by setting the frequency constant and varying the airspeed for a specified constant amplitude and initial displacement angle.

In all tests the steady airflow velocity was measured with a standard pitot-static tube located halfway between the oscillating sensor and the tunnel wall.

Experimental Results

The sensor was tested within a frequency range $1 < f < 5$ with the air-speed varying from $U_\infty = 11.6 \text{ m/s}$ (38 ft/s) to 30 m/s (100 ft/s). Higher frequencies were also attempted, but it was found that at higher frequencies (starting above 5) the signals on the strip chart became more and more ill defined and fuzzy as frequency was increased. In order to keep the variety of tests within reasonable limits, in some tests the angle of amplitude of oscillations ($2\alpha = \theta_L + \theta_U$) was kept constant, while the angle of displacement ($\theta_D = \alpha - \theta_L$) was varied stepwise. From the many experiments performed, table 1 presents a selection of samples for Reynolds numbers ranging from 0.55 to 1.74 with the frequency ranging from 1.59 to 5.05 Hz. Results of these tests are shown in figures 26 to 28. In these figures either the nondimensional pressure differential $\Delta p_{23}/q$ or $\Delta p_{12}/q$ was plotted against the instantaneous position angle θ of the sensor. The extreme position of this angle signifies the "dead end" of the oscillating motion, viz $+\theta_L$ and $-\theta_U$, and the sign signifies that angles above the horizontal reference line are taken as negative while below the line the angles are counted as positive. During a complete cycle, it appears that a loop is formed. During a downstroke, starting from $-\theta_U$, one follows (from left to right) the upper points of observations until the bottom of the downstroke $+\theta_L$ is reached; when turning around during the upstroke, one follows the lower observation points (from right to left).

In the tests presented in figures 26 to 28, the sensor oscillated between the angles $\theta_U = -8.62$ and $\theta_L = +10.55$ degrees measured from the horizontal reference line, thus having an amplitude $2\alpha = 19.17^\circ$ and

displacement $\theta_D = +0.96^\circ$. In figures 26 and 27 the nondimensional pressure differentials $\Delta p_{23}/q$ and $\Delta p_{12}/q$ are plotted against θ for a constant frequency with a variation of the Reynolds number. In figure 28, however, the Reynolds number was kept constant and results were plotted for two different frequencies. It appears from these graphs that the pressure loops vary in width and the higher the frequency the wider they are for a specified airflow; for a specified frequency it is the other way around: the higher the air velocity the narrower the loops become.

It appears from the results that the loops formed by the pressure differentials are affected by the relative airspeed experienced at the ports during the sensor's oscillatory motion. It was found that during the downstroke the observation points fell above those points which were obtained during the upstroke. This may be explained by considering that the relative airspeed is the resultant vector of the components U (free airstream velocity) and of the instantaneous tangential speed of the sensor V_t . During the entire downstroke the vector V_t points into a downward direction, thereby turning the oncoming stream upward from the horizontal by an angle $+\Delta\theta$. In other words, during the downstroke the incidence increases, bringing the stagnation point closer to port 3 and resulting in a higher positive p_3 and more negative p_2 than would be experienced without oscillation, as shown on the pressure distribution diagram in figure 29(a). The opposite holds for the upstroke, when the V_t vector points upwards, thereby turning the oncoming stream downwards from the horizontal by an angle $-\Delta\theta$ and decreasing the incidence. This results in a lower positive p_3 and less negative p_2 , as shown in figure 29(b). The value of $\Delta\theta$ depends on the frequency of the sensor and on the magnitude of the free airstream.

Comparison of Experiments with Theories

Based on the theories presented earlier, prediction of sensor performance appears to be in close agreement with the experiments. The theories also confirm the existence of the loops discussed in the preceding section. Various oscillating frequencies, air velocities, amplitudes,

and displacement angles were selected for the purpose of presenting samples of flow conditions. These results are presented in figures 30 to 32.

Figures 30 and 31 show results of the nondimensional pressure differential $\Delta p_{23}/q$ plotted against position angle θ . Figure 30 shows the results for lower Reynolds number $R_e = 0.365 \times 10^5$, while figure 31 shows results for a higher Reynolds number $R_e = 0.635 \times 10^5$. In figure 30(a), the frequency was $f = 2.43$ Hz and in figure 30(b) $f = 3.57$ Hz. In figure 30 the relevant angles were $\theta_L = +7.5^\circ$, $\theta_U = -25.5^\circ$, amplitude $2\alpha = 33^\circ$ and displacement $\theta_D = -9^\circ$. In figure 31(a), the relevant angles changed to $\theta_L = -4^\circ$, $\theta_U = 37.2^\circ$, $2\alpha = 33.2^\circ$, $\theta_D = 20.6^\circ$, and the frequency was $f = 2.72$ Hz. The frequency in figure 31(b) was $f = 4.03$ Hz.

Figure 32 shows results of the nondimensional pressure differential p_{12}/q plotted against position angle θ , for a Reynolds number $R_e = 0.635 \times 10^5$, and the relevant angles were $\theta_L = -9.6^\circ$, $\theta_U = +10^\circ$, $2\alpha = +19.6^\circ$, $\theta_D = 0.2^\circ$. The frequency for figure 32(a) was $f = 1.84$, and for figure 32(b), $f = 5.05$.

Inspection of figures 30 to 32 shows close agreement between both theories, and the agreement of both theories seems to be close with the experiments. It appears, however, that Theory II is closer to the experimental points during the downstroke while Theory I in some cases is closer to the points observed during the upstroke.

CONCLUSIONS

A sensor was designed for the instantaneous determination of flow direction and magnitude of an airstream flowing in the vicinity of an aircraft. Application of such a sensor to a helicopter blade under actual operational conditions was a major consideration of the design. Tests were performed on a model and on an actual sensor under both steady and unsteady flow conditions, and the responses have been carefully recorded and analyzed. Furthermore, theoretical studies have been made to predict the performance of the sensor under a variety of flow conditions. Ultimately, the experimental results were compared with theoretical predictions.

The following conclusions were drawn:

Steady-Flow Tests on Both the Model and Sensor Head

1. The results of the experiments on the model consisting of a 6.35-cm diameter sphere show that the Reynolds number has a marked effect on the pressure distribution, while the presence of the tail, representing a sting support, has only a minor influence.
2. Reynolds number effects are manifested both in a shift in the location of the zero pressure point experienced on the sphere's surface and in the shape of the distribution curves.
3. These effects ultimately influence the sphere constants b_{23} and b_{12} inasmuch as their values fall below the theoretically predicted value of 2.25 for the lower Reynolds numbers. However, for $R_e = 2.6 \times 10^5$, the experimentally obtained sphere constants appear to be remarkably close indeed to 2.25. Therefore, satisfactory data will result if the operation of sensors is confined to Reynolds numbers of this value or greater.
4. The central angle of 45 degrees permits the sphere to be used as a probe for sensing flow direction within the range of +30 to -22.5 degrees.
5. Sensors with central angles less than or greater than 45 degrees can also be designed which may provide a different angular range but probably with reduced output. Lower output is of little concern. Improved linearity is important, especially if coupled with insensitivity to viscosity effects.
6. Calibration of the sensor, consisting of a 3.2-cm spherical head with a sting support, show that the transducers built into the head furnished answers similar, if not completely identical, to the pressure distribution curves obtained on the model. The b_{23} sphere (or sensor) coefficient is slightly lower than that experienced with the model, but the b_{12} coefficient is considerably lower, thereby indicating that the b_{12} coefficient is more sensitive to viscous effects. It is noted that the sensor's range lies between +30 and -22.5 degrees.

Tests with the Sensor Under Oscillating Conditions

7. The sensor output on the strip charts proved satisfactory in the frequency range $0 < f < 5$ Hz, but above 5 Hz the lines on the charts showed increased sensitivity to vibrations which may not be the fault of the sensor but of the mechanical drive system.

8. Comparison of experimental results with theory shows a satisfactory agreement. Both the experiments and the theoretical results show that under oscillating conditions the pressure differentials form a loop for the points recorded during downstroke and upstroke. The curves differ because during downstroke the instantaneous tangential speed of the spherical sensor increases the angle of incidence, while during the upstroke it decreases the incidence, resulting in a larger pressure differential during downstroke than during upstroke. The width of the loop was found to depend on the free airstream and the frequency of oscillations.

9. In the theoretical calculations of the pressure differentials Δp_{23} and Δp_{12} , the sphere coefficients have an important influence. It was found for the results presented the theory fitted best to the experimental points when $b_{23} = 2.03$ and $b_{12} = 1.79$ (as noted on the various graphs).

10. Some disagreement between theory and experiment appears which is thought to have been caused by certain time lag phenomena due to unsteady inertial effects of the mechanical system and to boundary-layer effects so far unaccounted in the theories.

It appears from these conclusions that the sensor described here has a definite application in exploring unsteady flow fields in the vicinity of aircraft. In a particular application to helicopter blades it may be quite easily feasible to measure the angle of attack and the dynamic head during actual flight operation assuming that the forward speed of the craft, the rotational speed of the rotor, and the blade angles due to the cyclic motion are simultaneously measured.

The tests covered a range of Reynolds numbers from 0.4 to about 2.6×10^5 in the low Mach number range. Since helicopter blades move at higher Mach numbers, it is recommended to extend these tests to cover the higher Mach number range as well.

REFERENCES

1. Bryer, D.W.; Walshe, D.E.; and Garner, H.C.: Pressure Probes Selected for Three-Dimensional Flow Measurement. Reports and Memoranda No. 3037, British ARC, 1955.
2. Liu, Henry Weiyuan: Design, Calibration and Application of a Sensor for Measuring Time Dependent Angle of Attack of Helicopter Blades. PhD dissertation, Old Dominion University, 1978.
3. Nowack, C.F.R.: Improved Calibration Method for a Five-Hole Spherical Pitot Probe. *J. Phys. E: Scientific Instruments*, Vol. 3, 1970, pp. 21-26.
4. Thurtell, G.W.; Tanner, C.B.; and Wesely, M.L.: Three-Dimensional Pressure-Sphere Anemometer System. *J. Appl. Meteor.*, Vol. 9, 1970, pp. 379-385.
5. Wesley, M.L.; Tanner, C.B.; and Thurtell, G.W.: An Improved Pressure-Sphere Anemometer. *Boundary-Layer Meteorology*, Vol. 2, 1972, pp. 275-283.
6. Montoya, E.J.: Wind Tunnel Calibration and Requirements for In-Flight Use of Fixed Hemispherical Head Angle-of-Attack and Angle-of-Sideslip Sensors. NASA TN D-6986, 1973.
7. Bennett, J.C.: Use of Five-Hole Pneumatic Probe in Unsteady Flows. *Progress in Astronautics and Aeronautics*, Vol. 53, 1977, pp. 71-82.
8. Yuan, S.W.: Foundation of Fluid Mechanics. Prentice-Hall, Inc., 1967, pp. 233-236.
9. Batchelor, G.K.: An Introduction to Fluid Mechanics. Cambridge Univ. Press (New York), 1967, pp. 449-453.
10. Karamcheti, K.: Principles of Ideal-Fluid Aerodynamics. John Wiley and Sons, Inc., 1966, pp. 278-290.
11. Lamb, H.: Hydrodynamics. 6th ed., The MacMillan Co. (New York); reprinted by Dover Publications, Inc., New York, 1945, pp. 110-125.
12. Fage, A.: Experiments on a Sphere at Critical Reynolds Numbers. Reports and Memoranda No. 1766, British ARC, 1936.
13. Goldstein, S.: Modern Developments in Fluid Dynamics, Vol. 1, Dover Ed., 1965, pp. 263-264.
14. Hoerner, S.: Versuche mit Kugeln Betreffend Kennzahl, Turbulenz und Oberflächenbeschaffenheit. *Luftfahrtforschung*, Vol. 12, No. 1, 1935.

15. Patterson, J.L.: A Miniature Electrical Pressure Gage Utilizing a Stretched Flat Diaphragm. NASA TN-2659, 1951.
16. Sokolnikoff, I.S.; and Redheffer, R.M.: Mathematics of Physics and Modern Engineering, 2nd ed. McGraw-Hill Book Co., 1966.

Table 1. Samples of the Oscillating Sensor Program

Test Number	R_e range, $\times 10^5$	Incidence θ range, degrees	Frequency f range, Hz
1	0.552 to 1.739	-8.62° to 10.55°	1.59
2	0.552 to 1.159	-8.62° to 10.55°	2.92
3	0.552 to 1.739	-8.62° to 10.55°	3.46
4	1.159 to 1.739	-8.62° to 10.55°	2.92
5	0.635	-8.62° to 10.55°	4.81

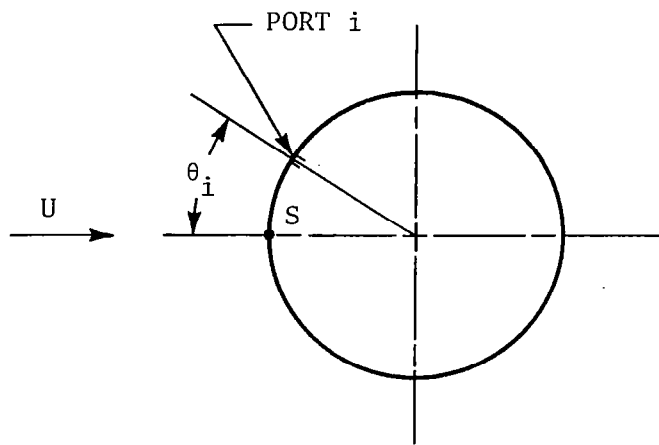


Figure 1(a). Spherical object provided with one port.

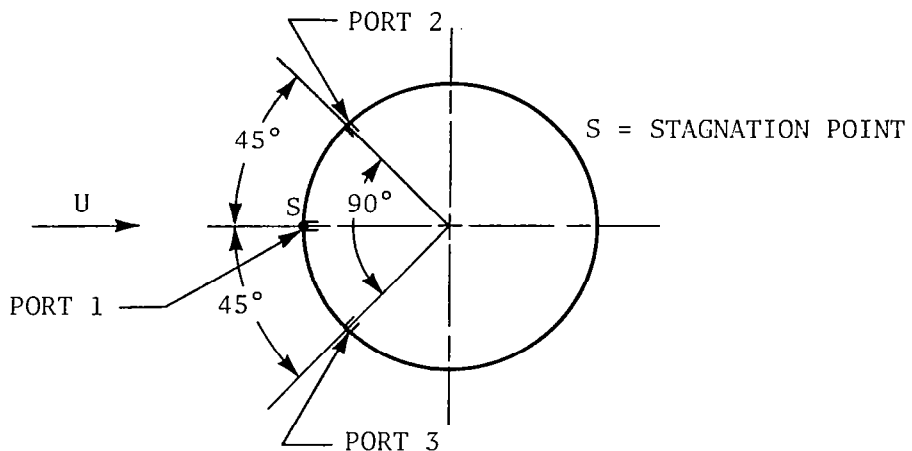


Figure 1(b). Spherical object provided with three ports; airflow at zero incidence.

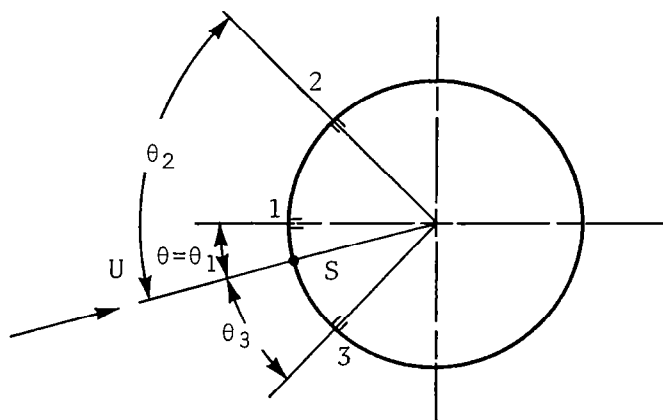


Figure 1(c). Spherical object with approaching airflow U at incidence θ .

Figure 1. Location of ports and the stagnation point S on sphere.

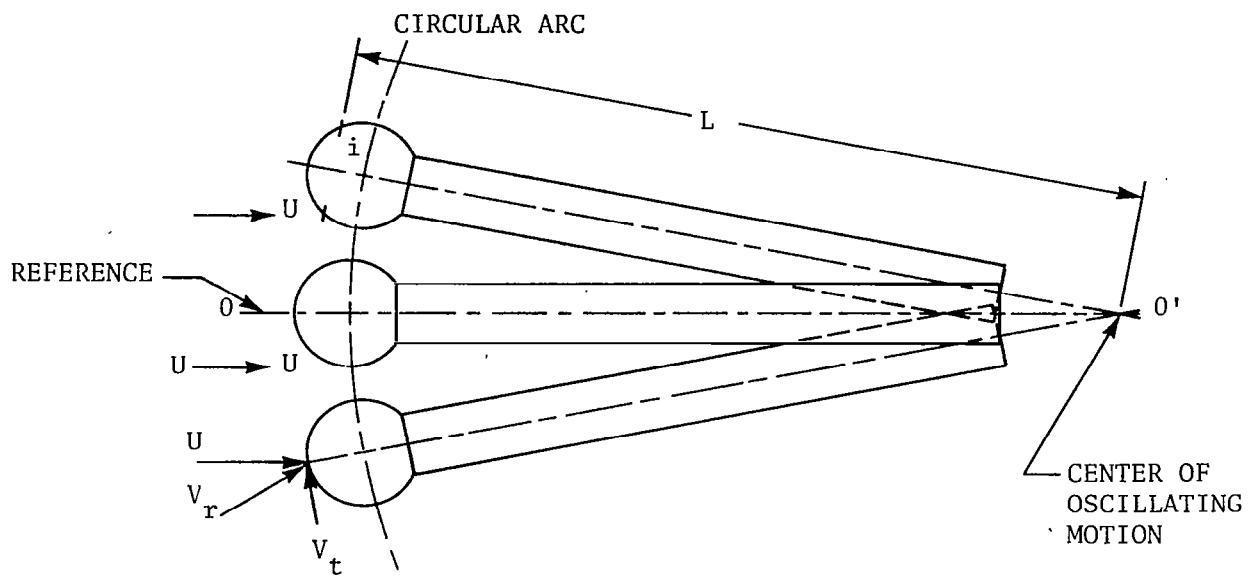


Figure 2. Schematic diagram of oscillating sensor motion.

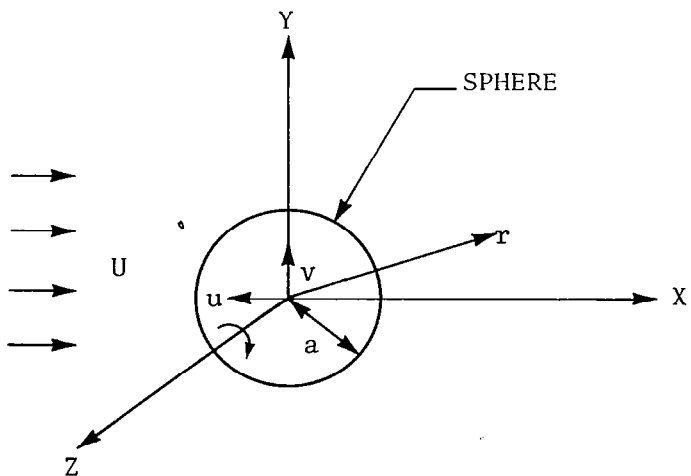
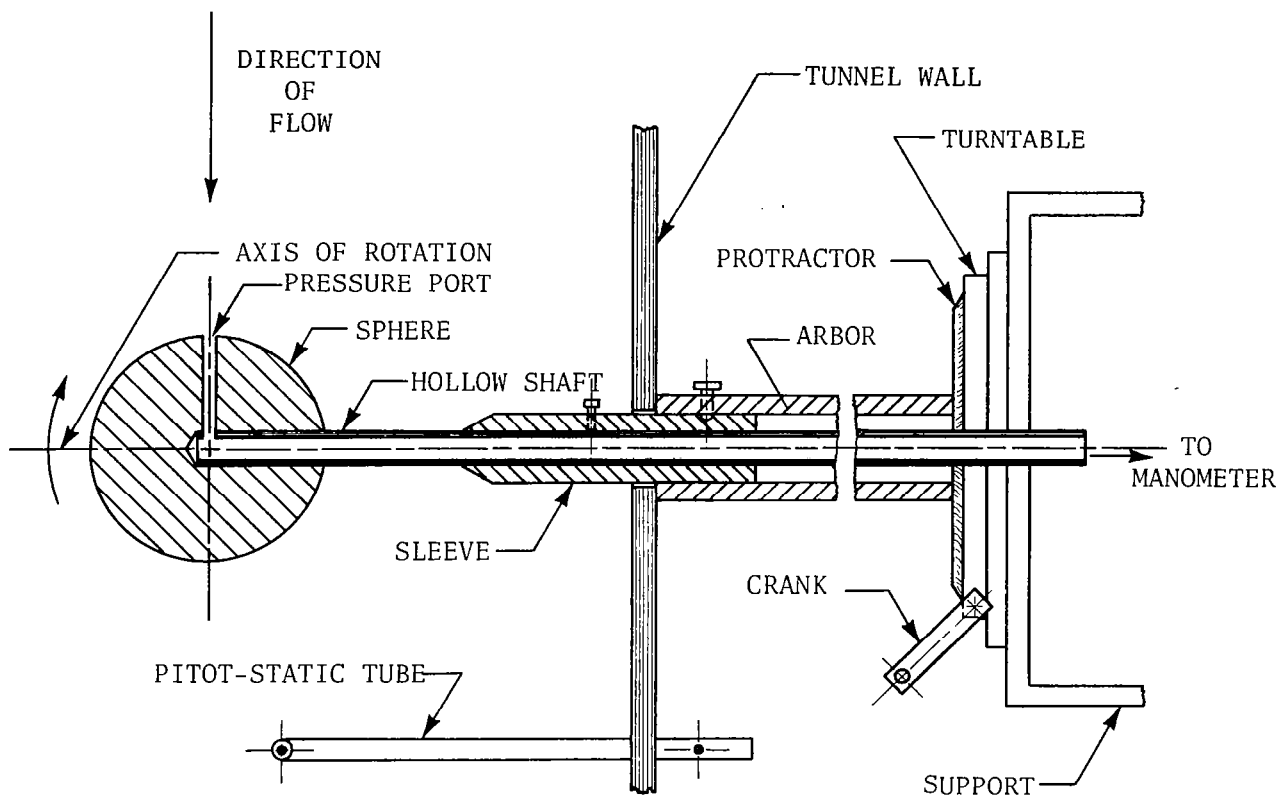
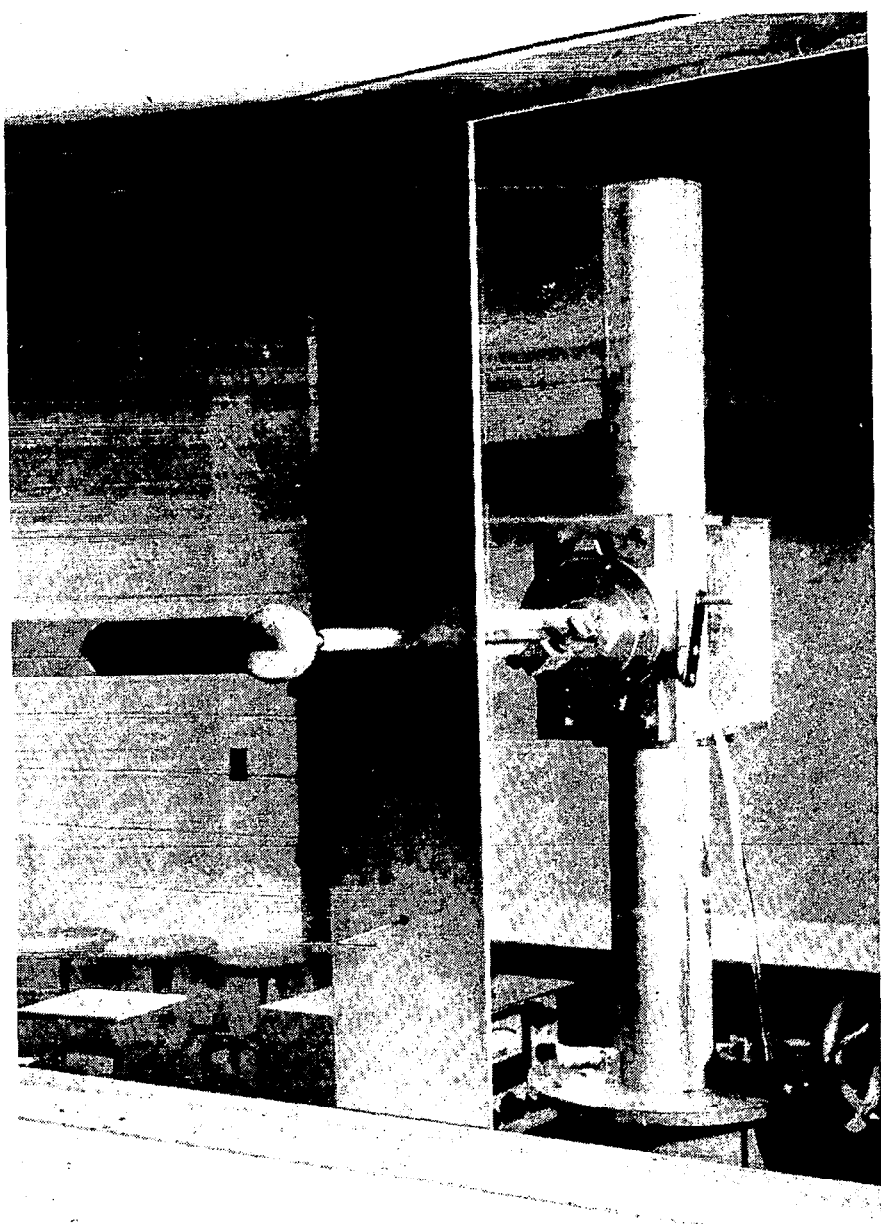


Figure 3. Components of sphere motion.



(a) Schematic arrangement.

Figure 4. Sphere setup for experiments inside return circuit wind tunnel.



(b) Photograph of setup.

Figure 4. (Concluded).

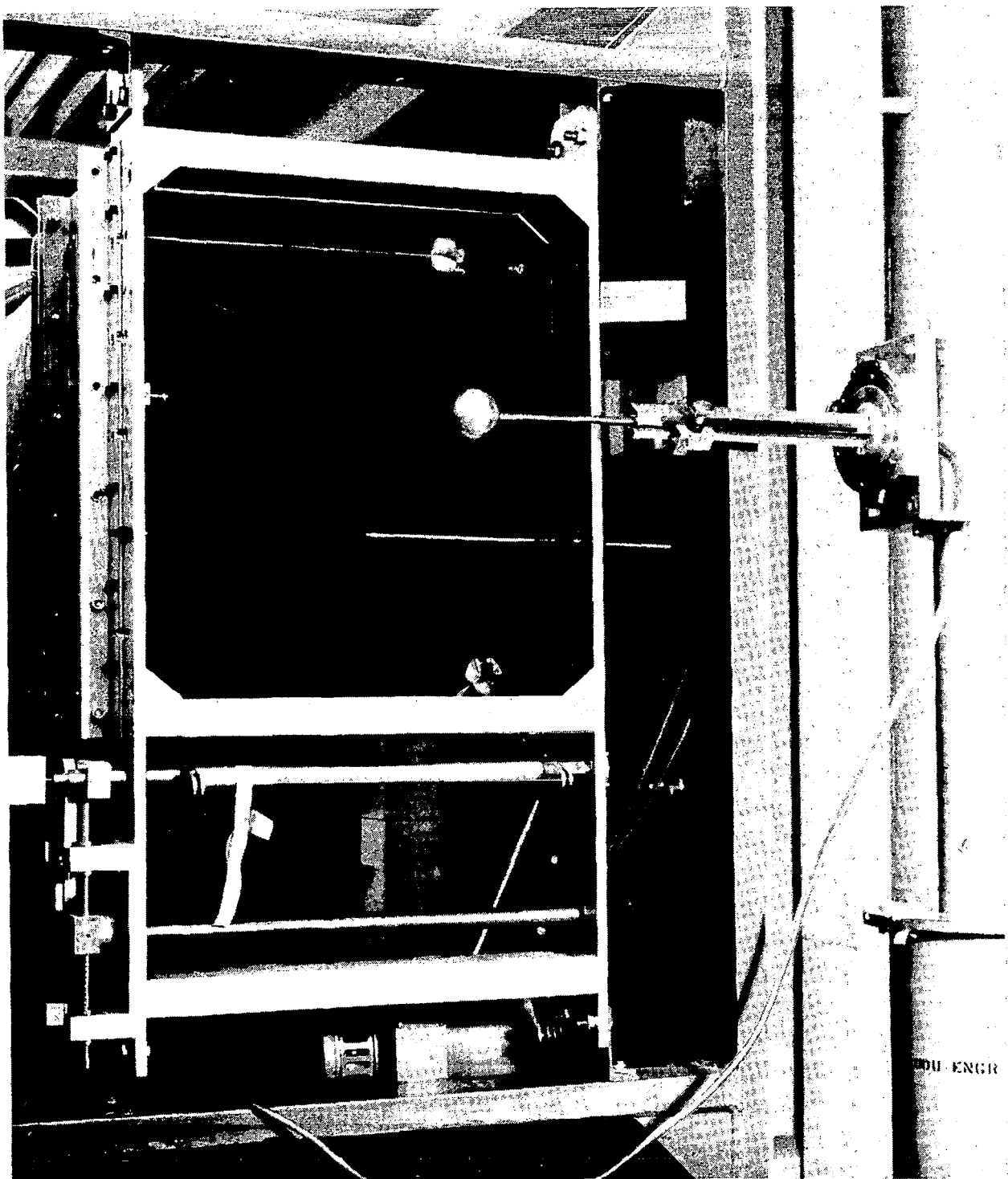


Figure 5. Experimental setup in the open wind tunnel (sphere without tail).

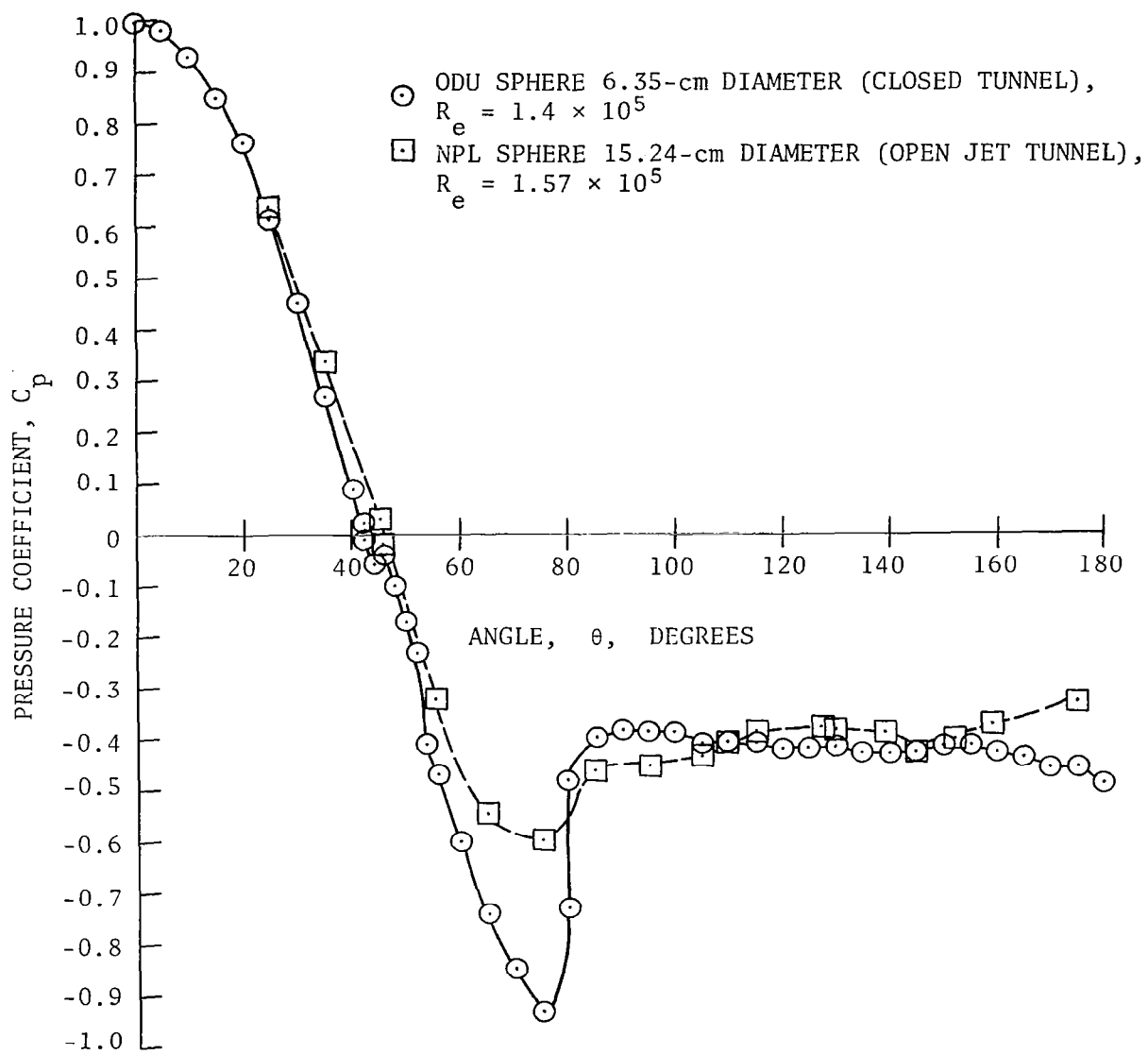


Figure 6. Comparison between the pressure distribution obtained at the ODU large wind tunnel and that obtained at NPL (England) at about the same Reynolds number.

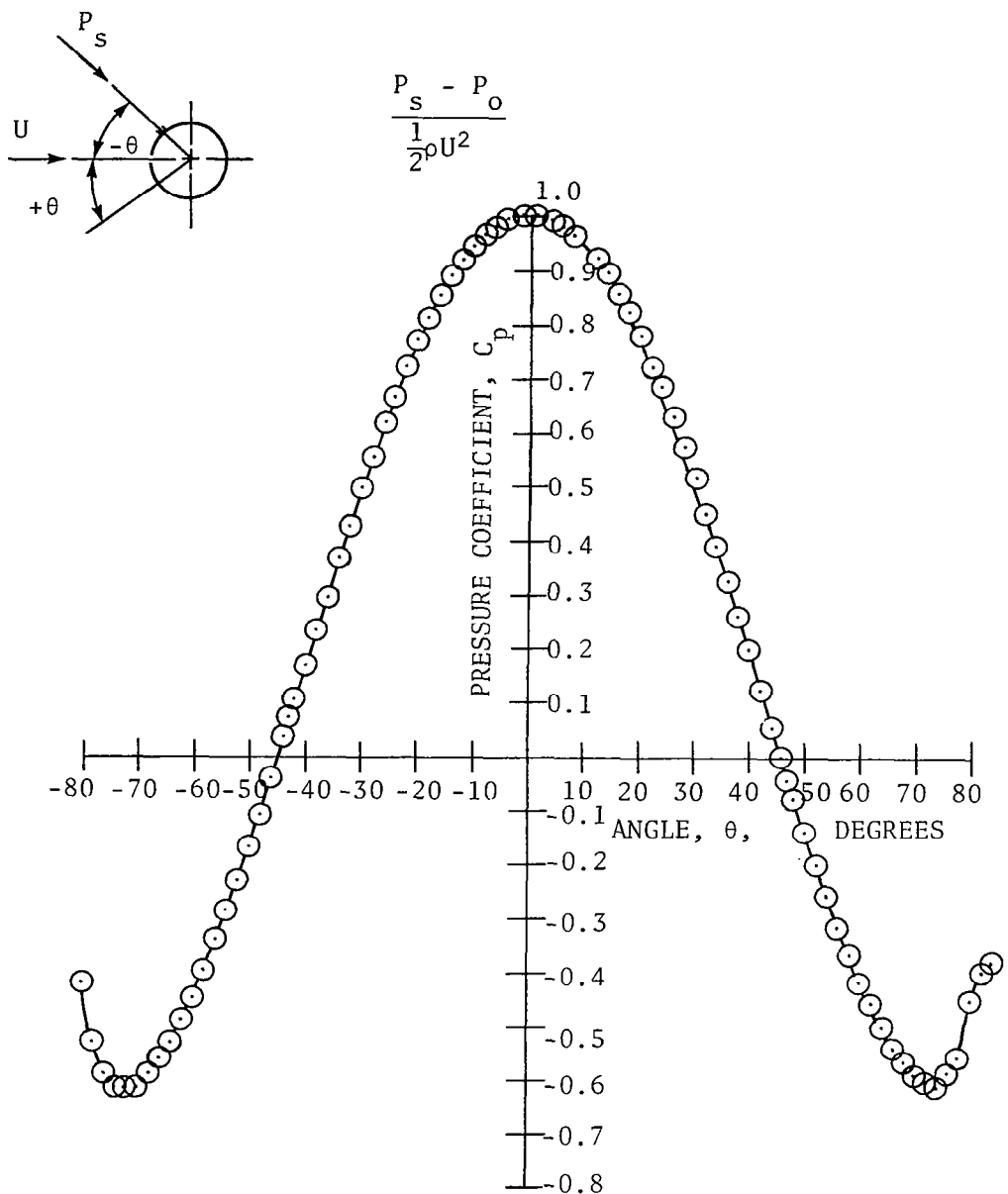


Figure 7. Pressure distribution around a 6.35-cm sphere without tail at $R_e = 1.4 \times 10^5$ obtained in the open wind tunnel.

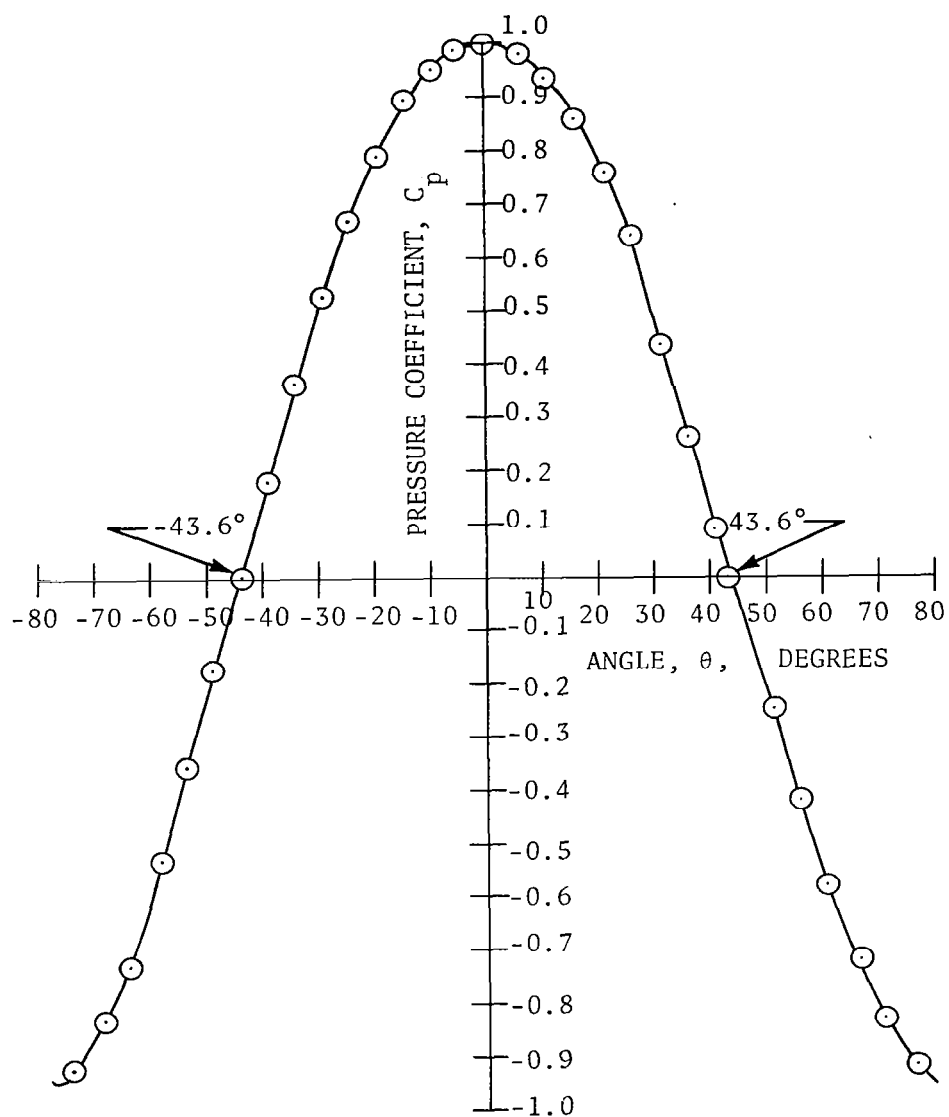
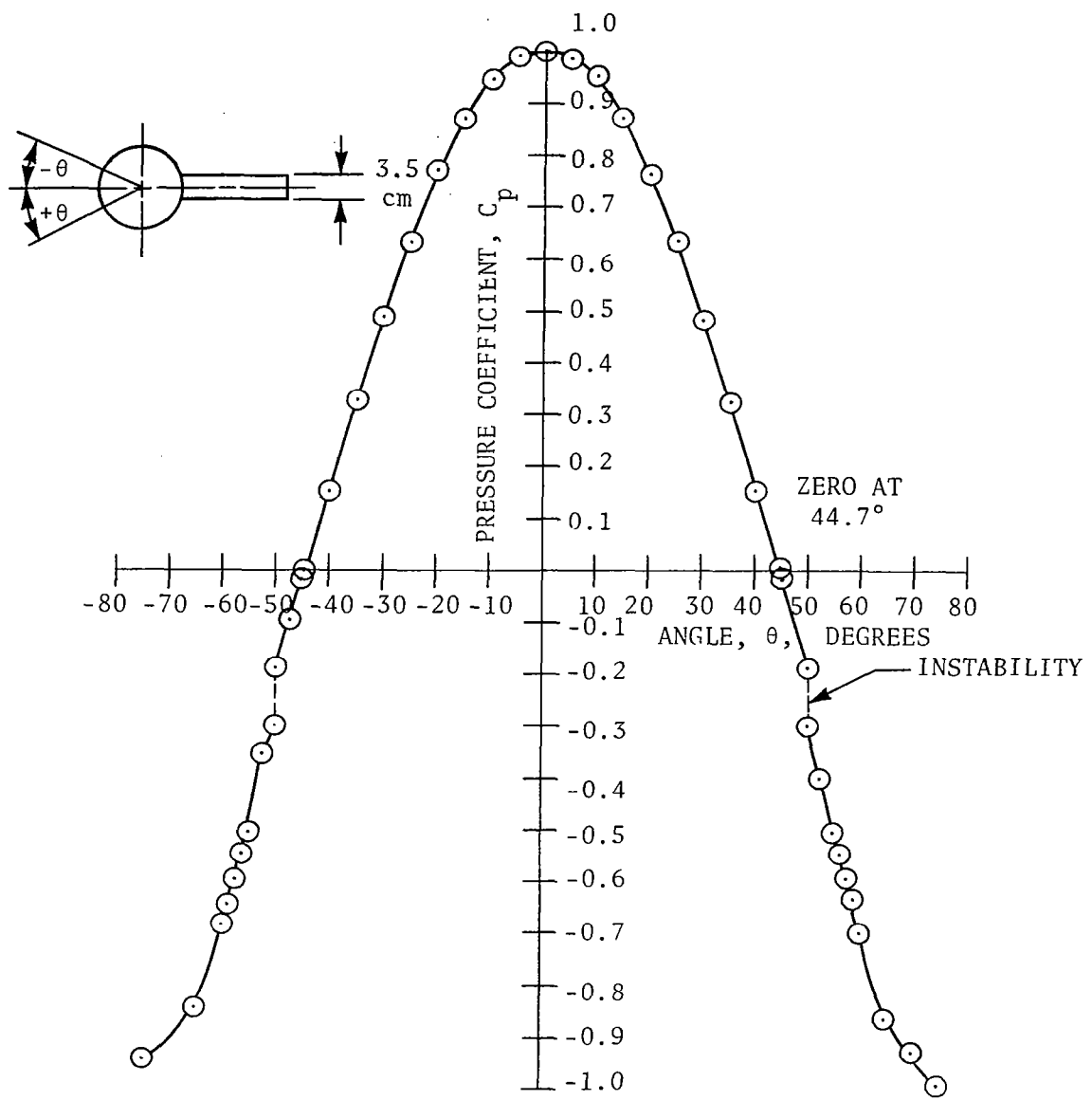
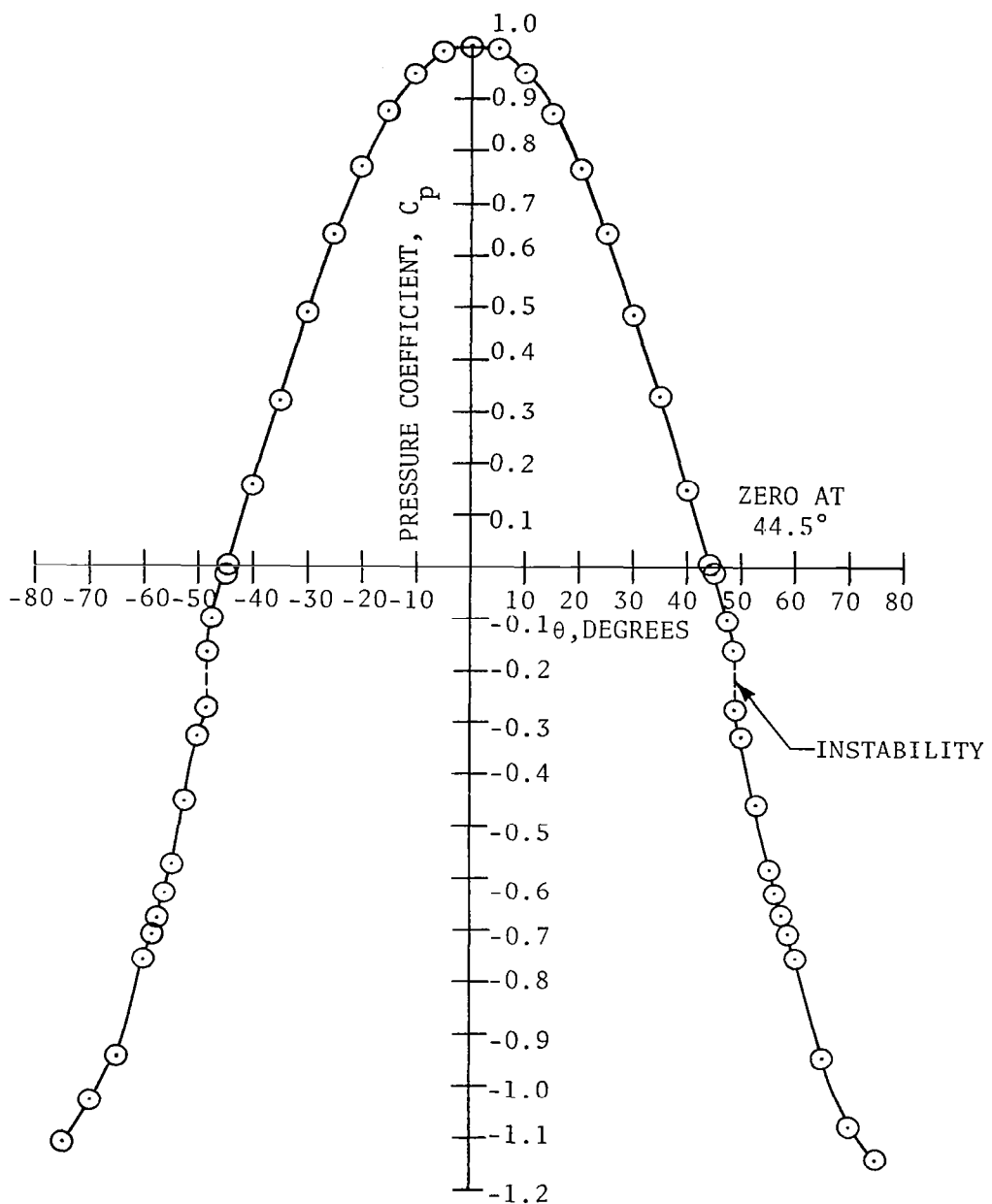


Figure 8. Pressure distribution around a 6.35-cm sphere without tail at $R_e = 2.6 \times 10^5$ obtained in the closed wind tunnel.



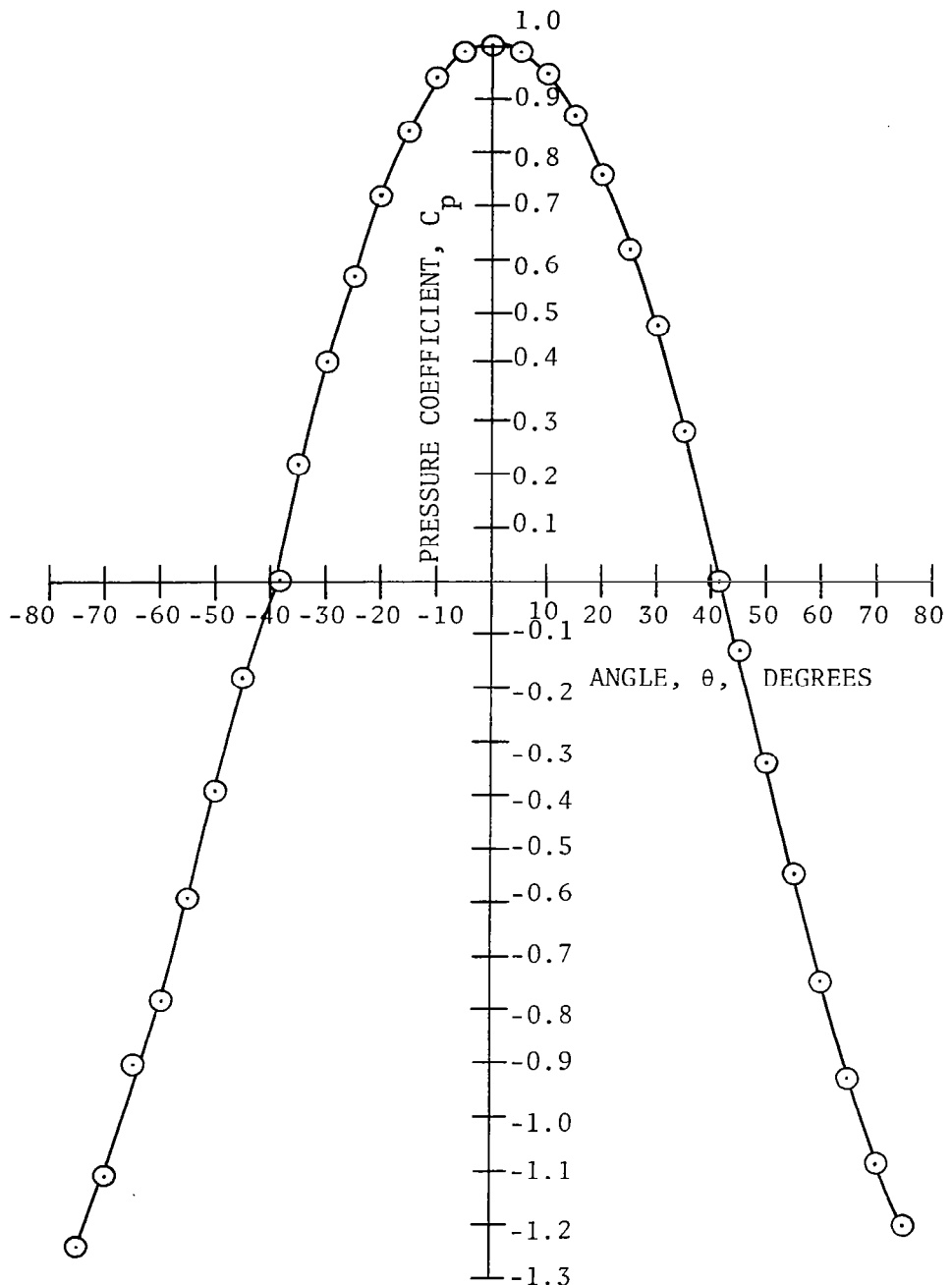
(a) $R_e = 0.91 \times 10^5$; open wind tunnel.

Figure 9. Pressure distribution around a 6.35-cm sphere fitted with a 3.5-cm tail.



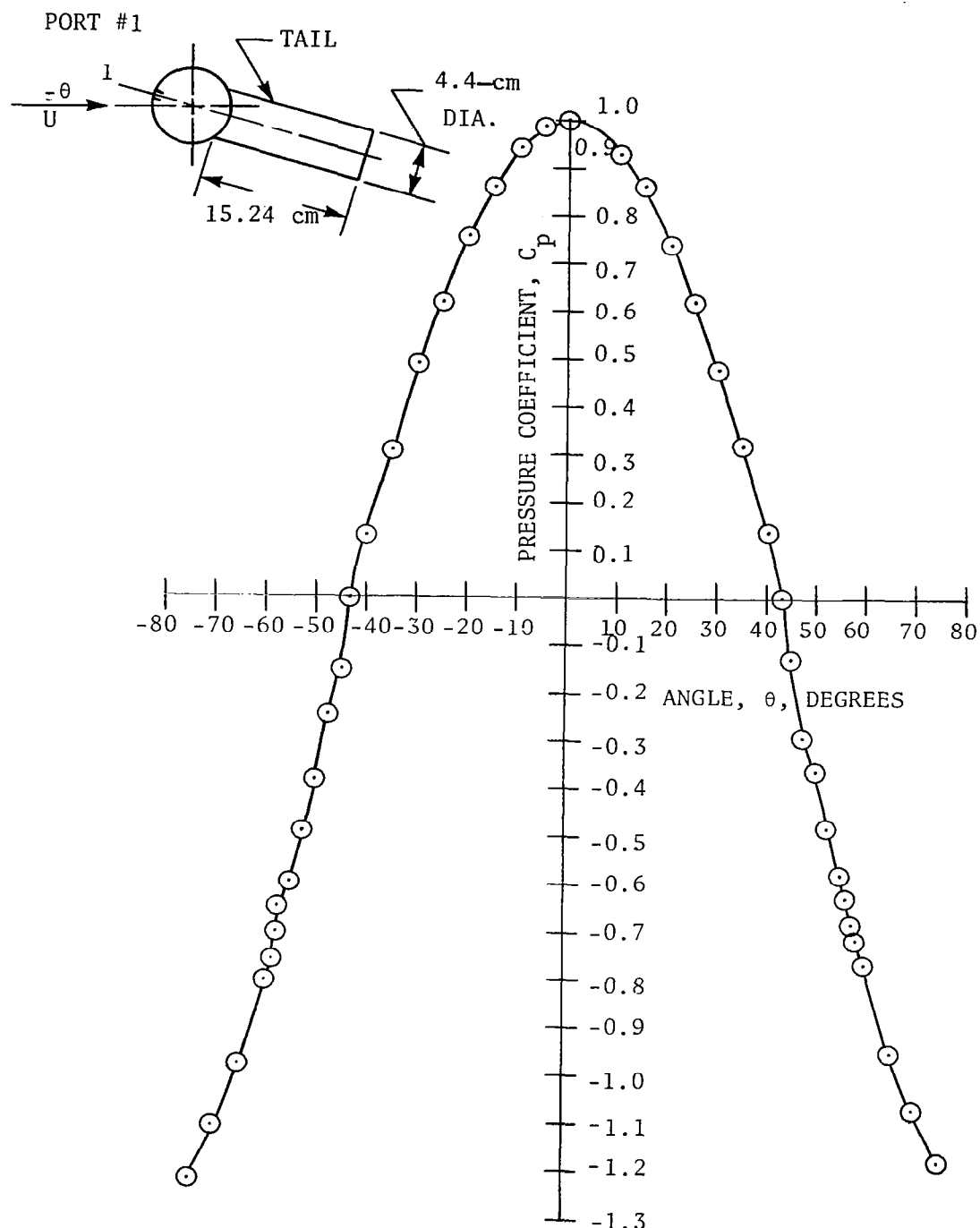
(b) $R_e = 1.4 \times 10^5$; open wind tunnel.

Figure 9. (Continued).



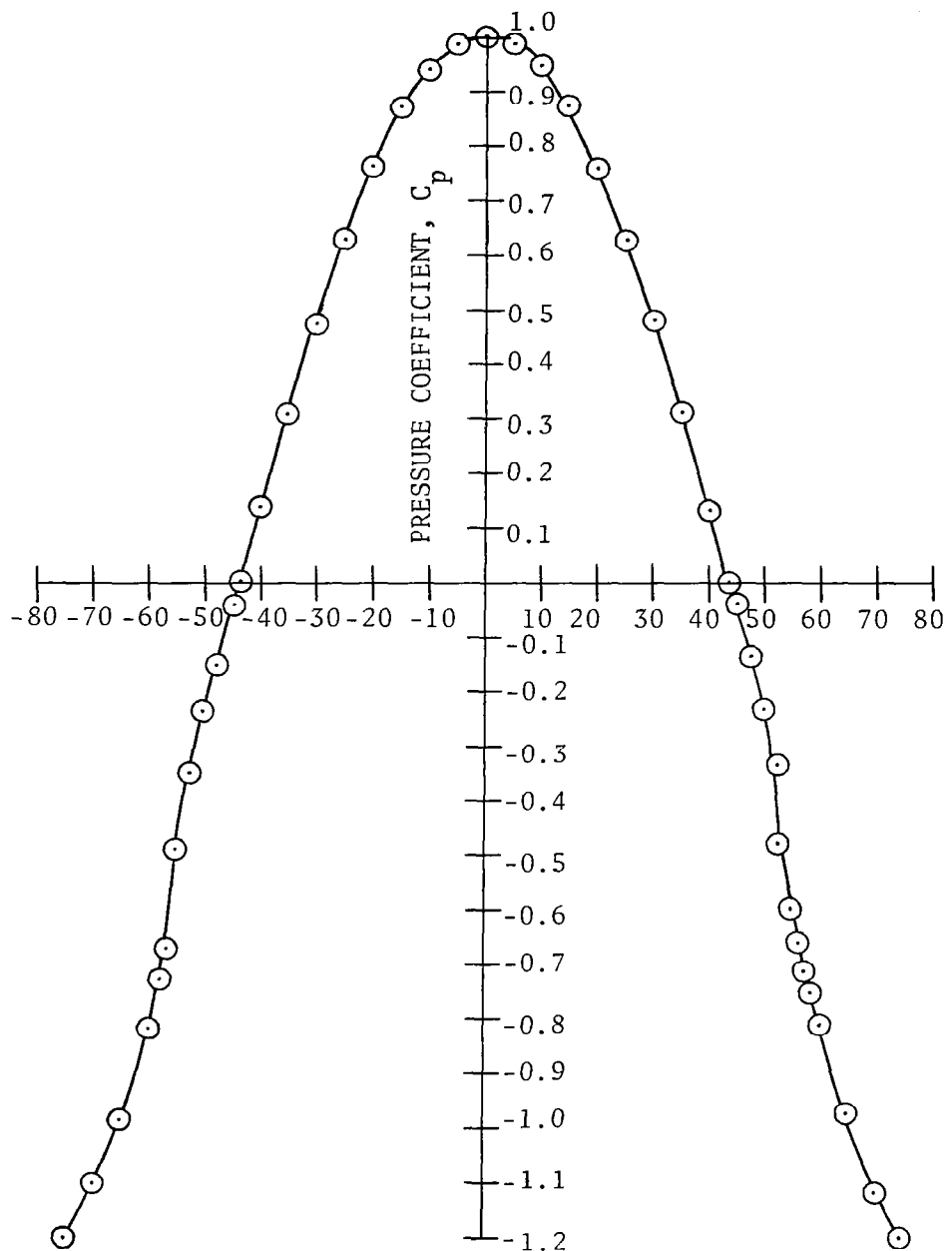
(c) $R_e = 2.6 \times 10^5$; closed wind tunnel.

Figure 9. (Concluded).



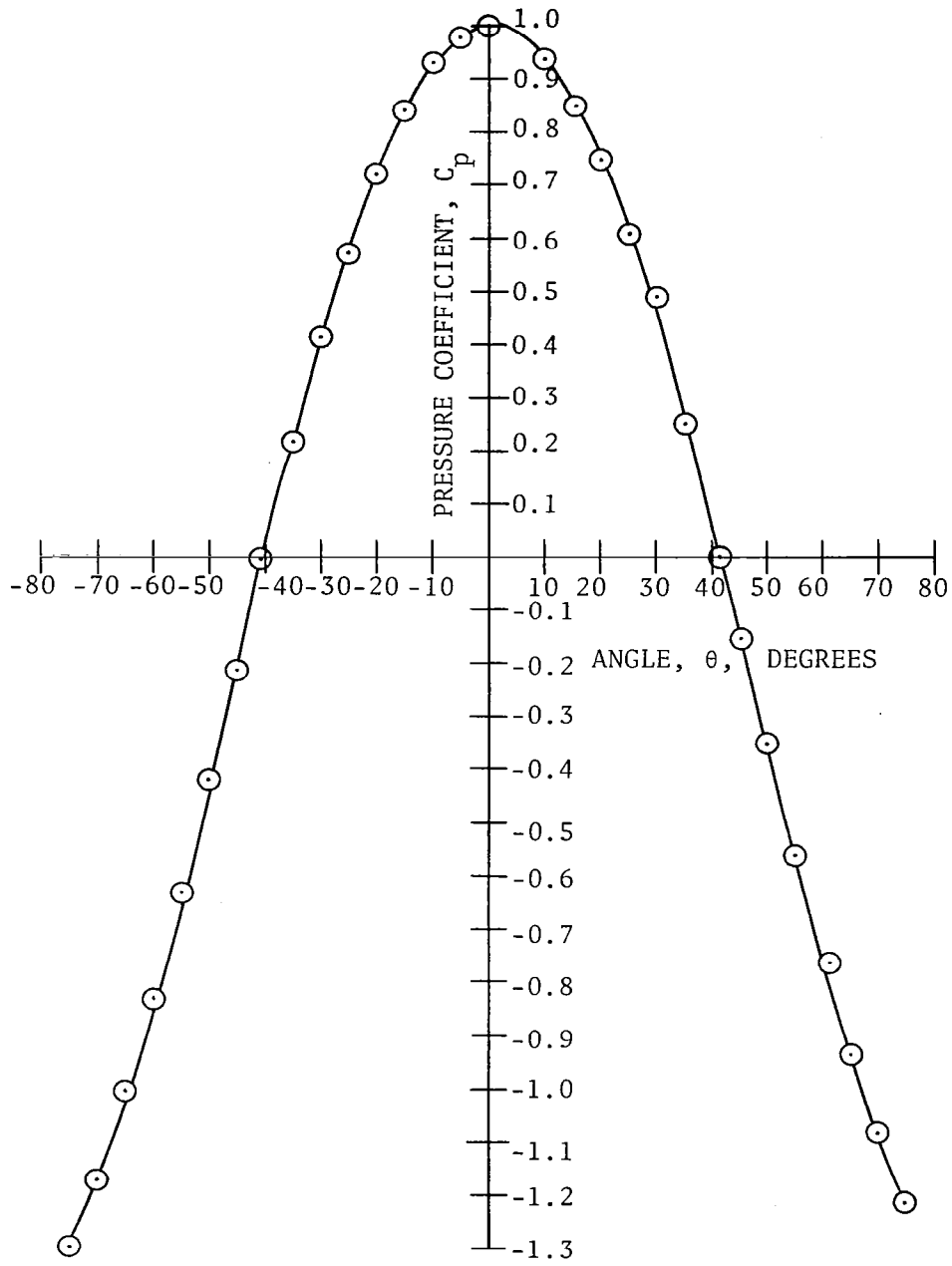
(a) $R_e = 0.91 \times 10^5$; closed wind tunnel.

Figure 10. Pressure distribution around a 6.35-cm sphere fitted with a 4.4-cm tail.



(b) $R_e = 1.4 \times 10^5$; open wind tunnel.

Figure 10. (Continued).



(c) $R_e = 2.6 \times 10^5$; closed wind tunnel.

Figure 10. (Concluded).

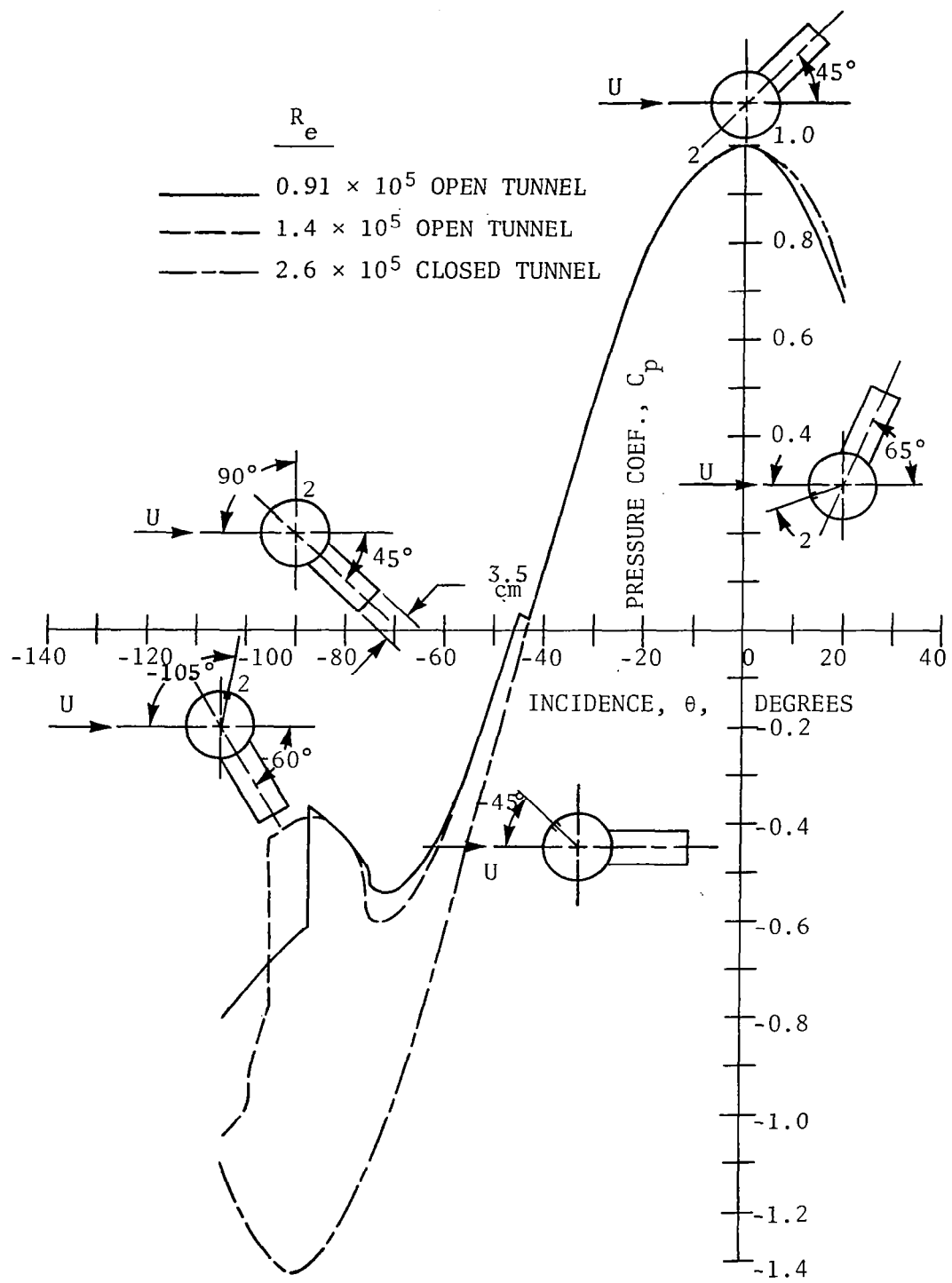


Figure 11. Pressure distribution around a 6.35-cm sphere fitted with a 3.5-cm tail, port 2.

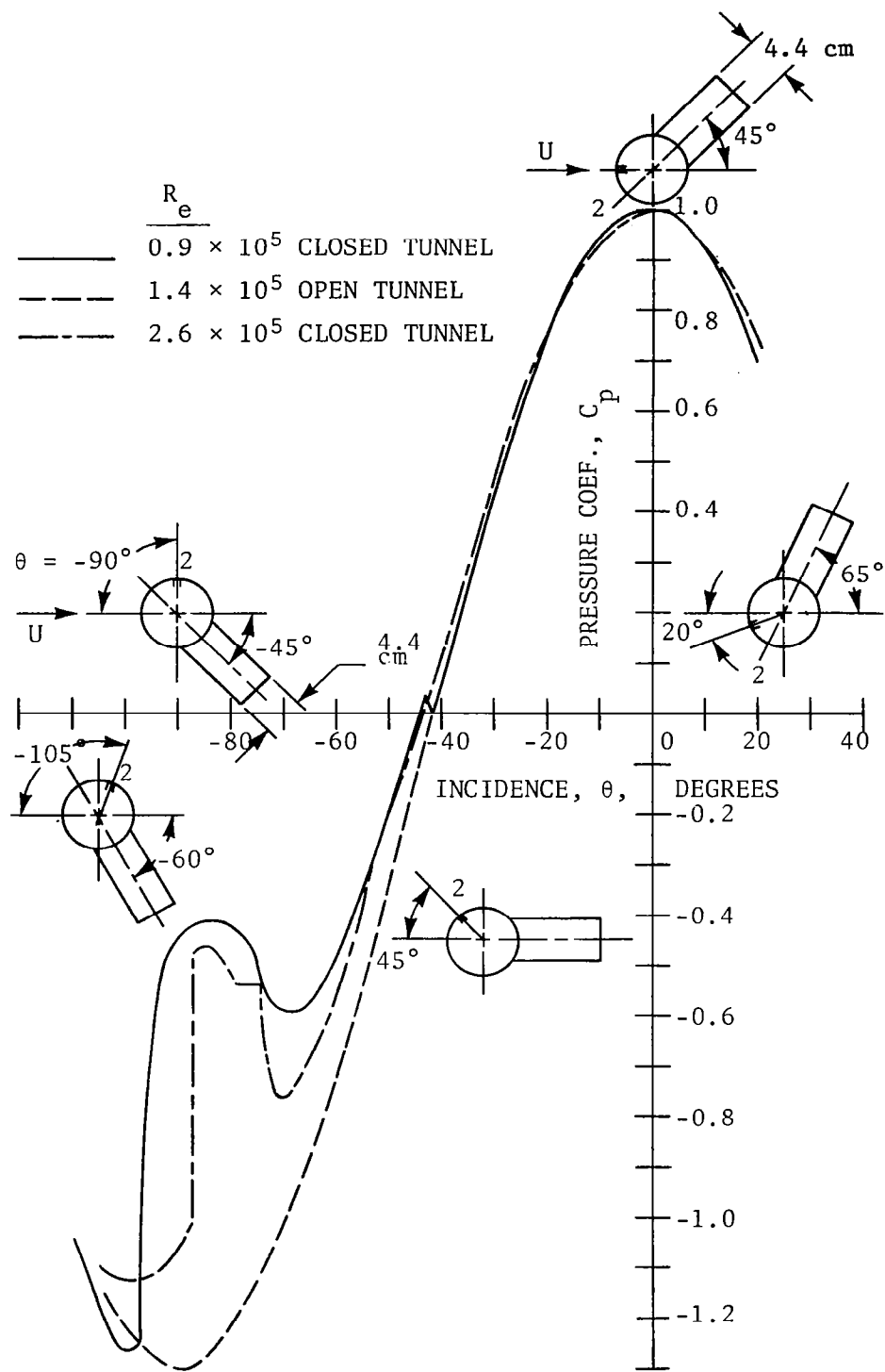
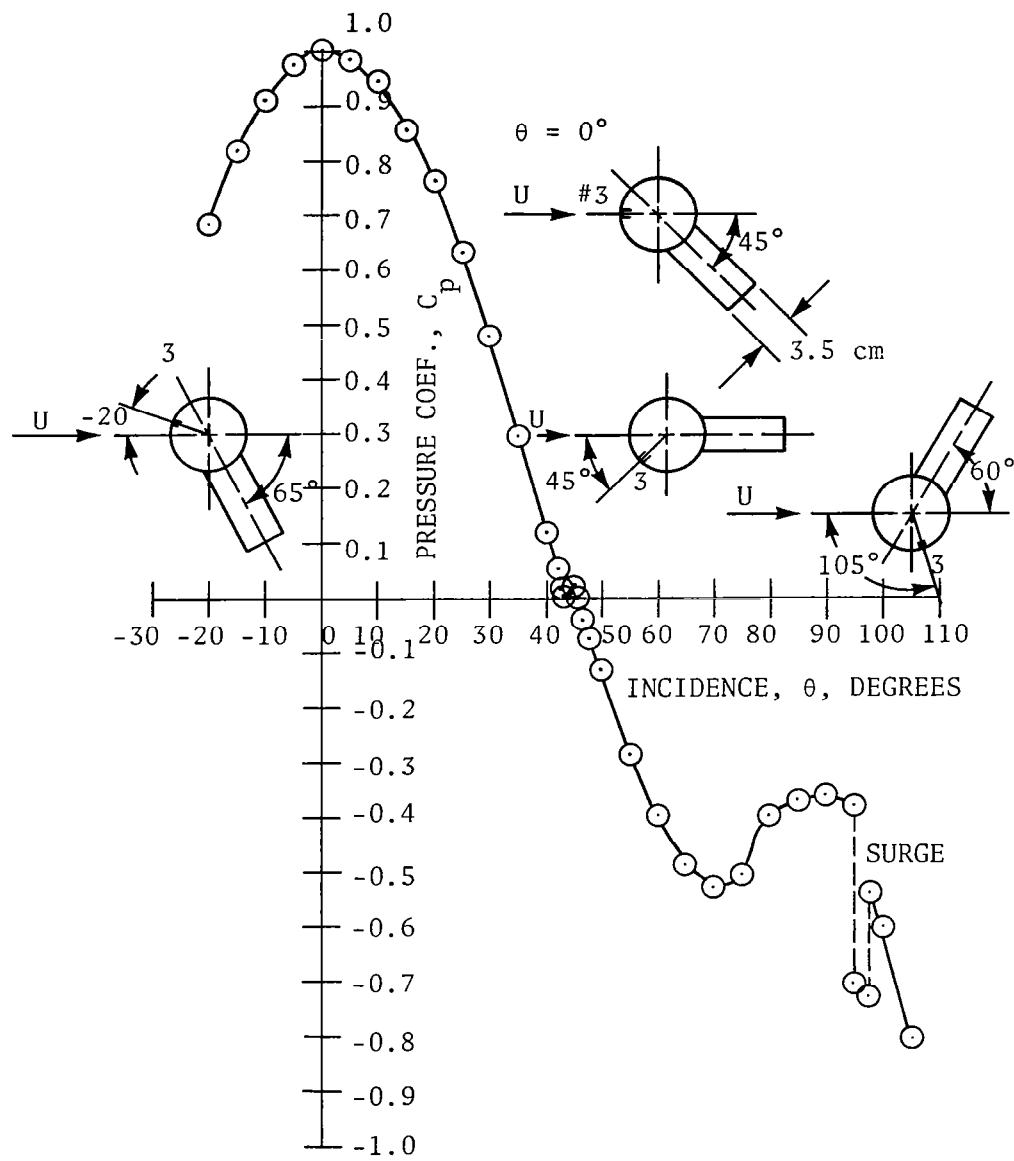
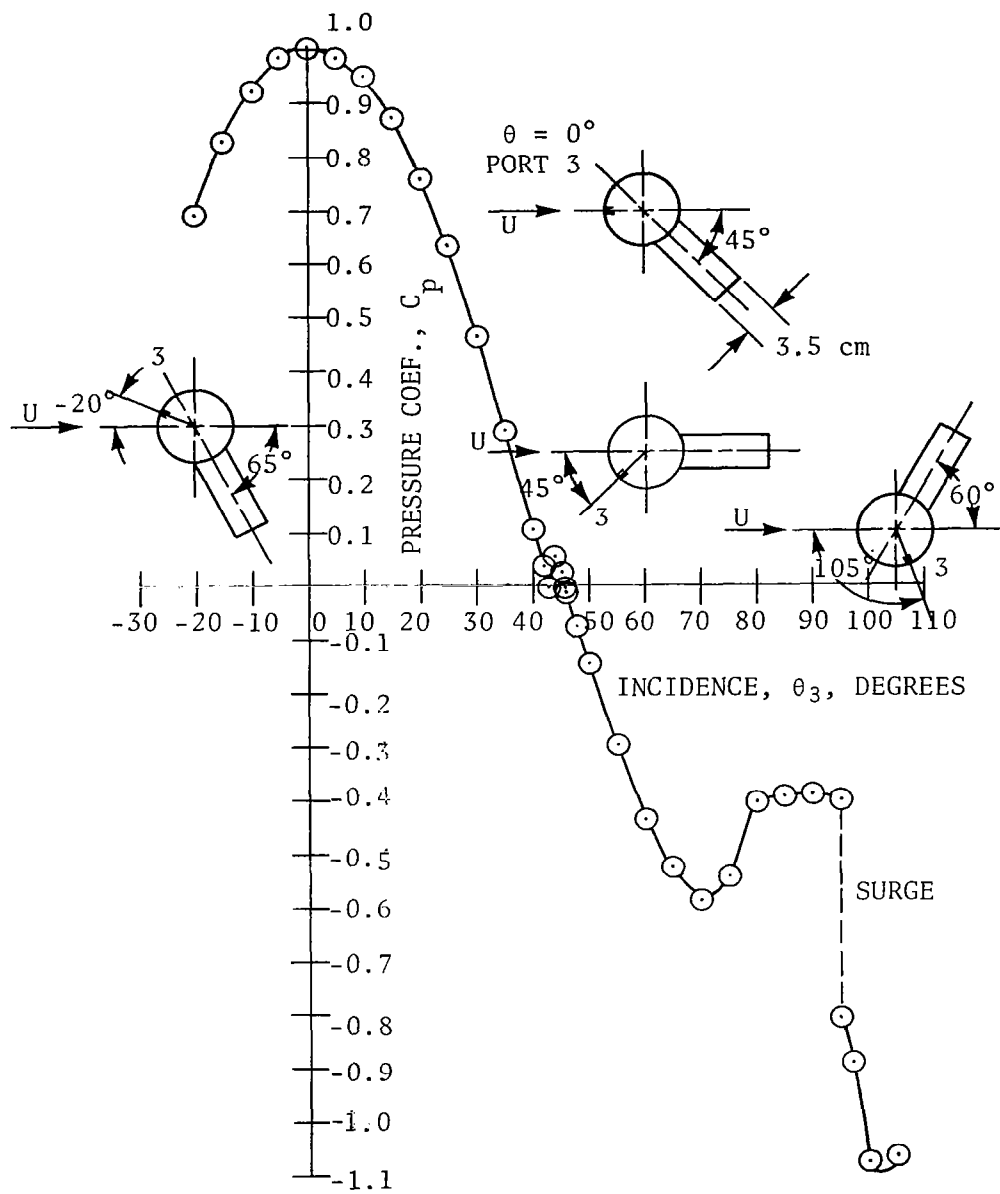


Figure 12. Pressure distribution around a 6.36-cm sphere fitted with a 4.4-cm tail, port 2.



(a) $R_e = 0.91 \times 10^5$; open wind tunnel.

Figure 13. Pressure distribution around a 6.35-cm sphere fitted with a 3.5-cm tail, port 3.



(b) $R_e = 1.4 \times 10^5$; open wind tunnel.

Figure 13. (Concluded).

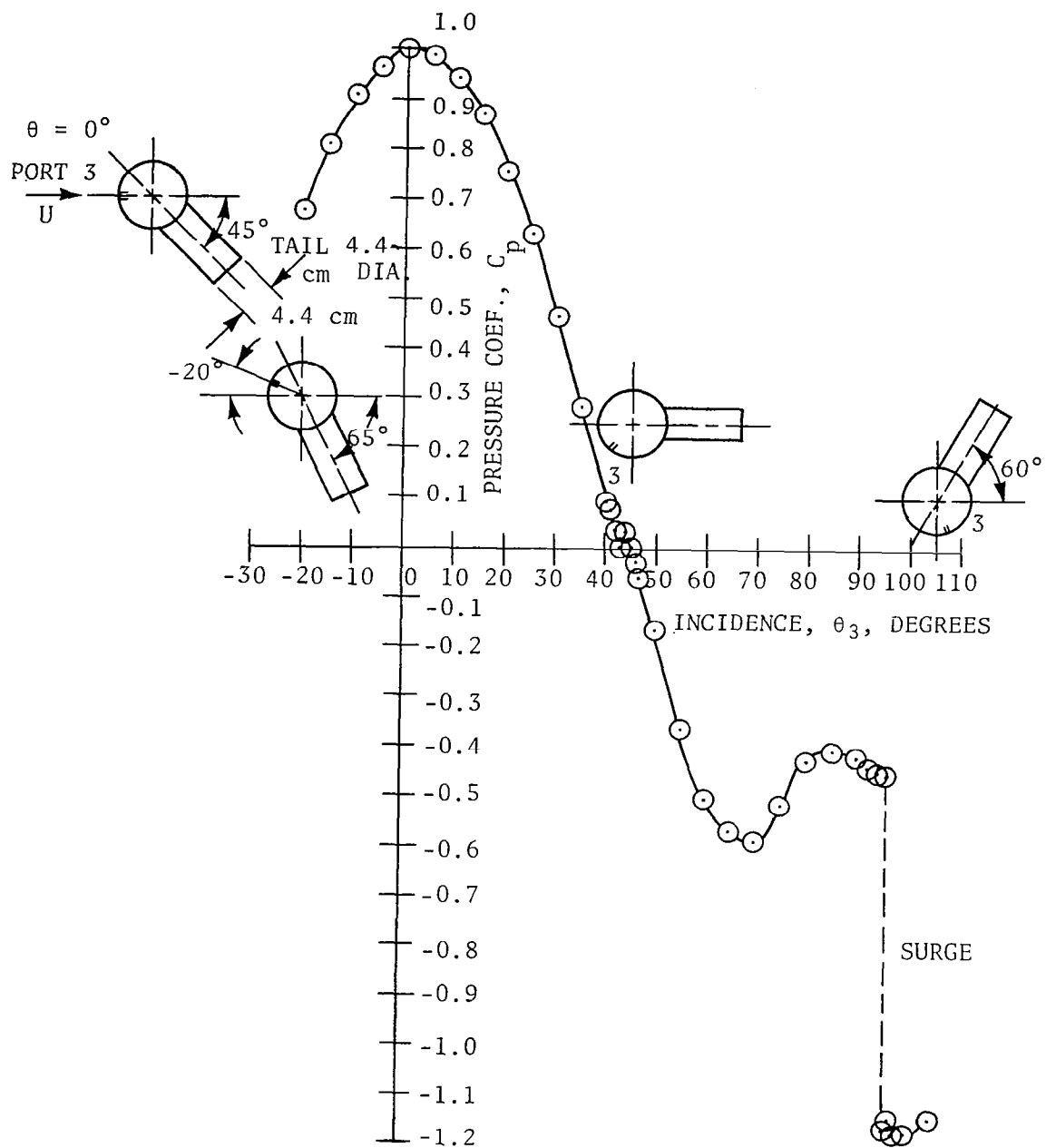


Figure 14. Pressure distribution around a 6.35-cm sphere fitted with a 4.4-cm tail, port 3.

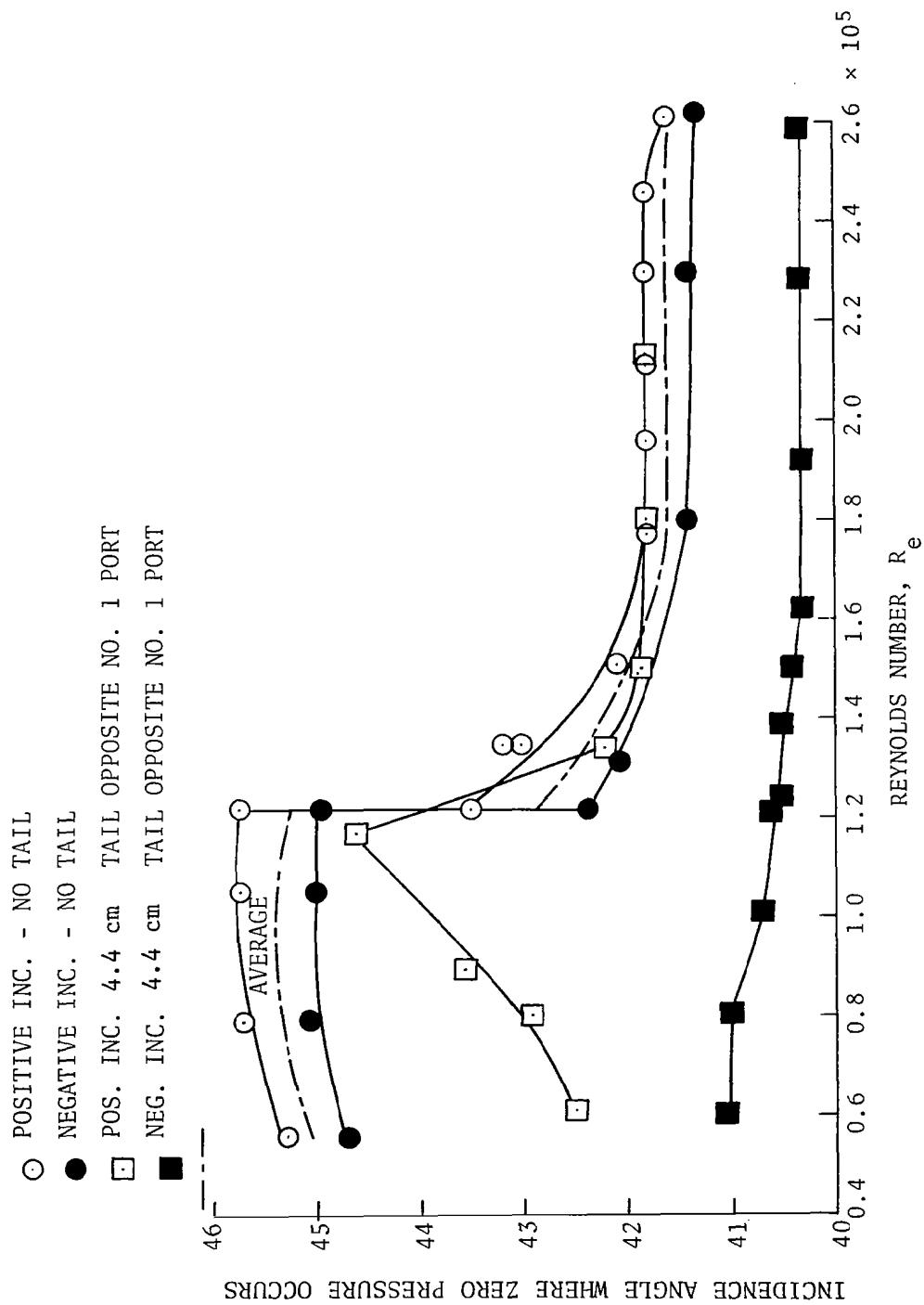


Figure 15. Variation of zero pressure point on the surface of the sphere with Reynolds number (tests in closed wind tunnel).

$\frac{R_e}{e}$	b_{23}	TAIL DIA.	WIND TUNNEL
2.6×10^5	2.25	4.4 cm	CLOSED
1.4×10^5	1.93	4.4 cm	OPEN

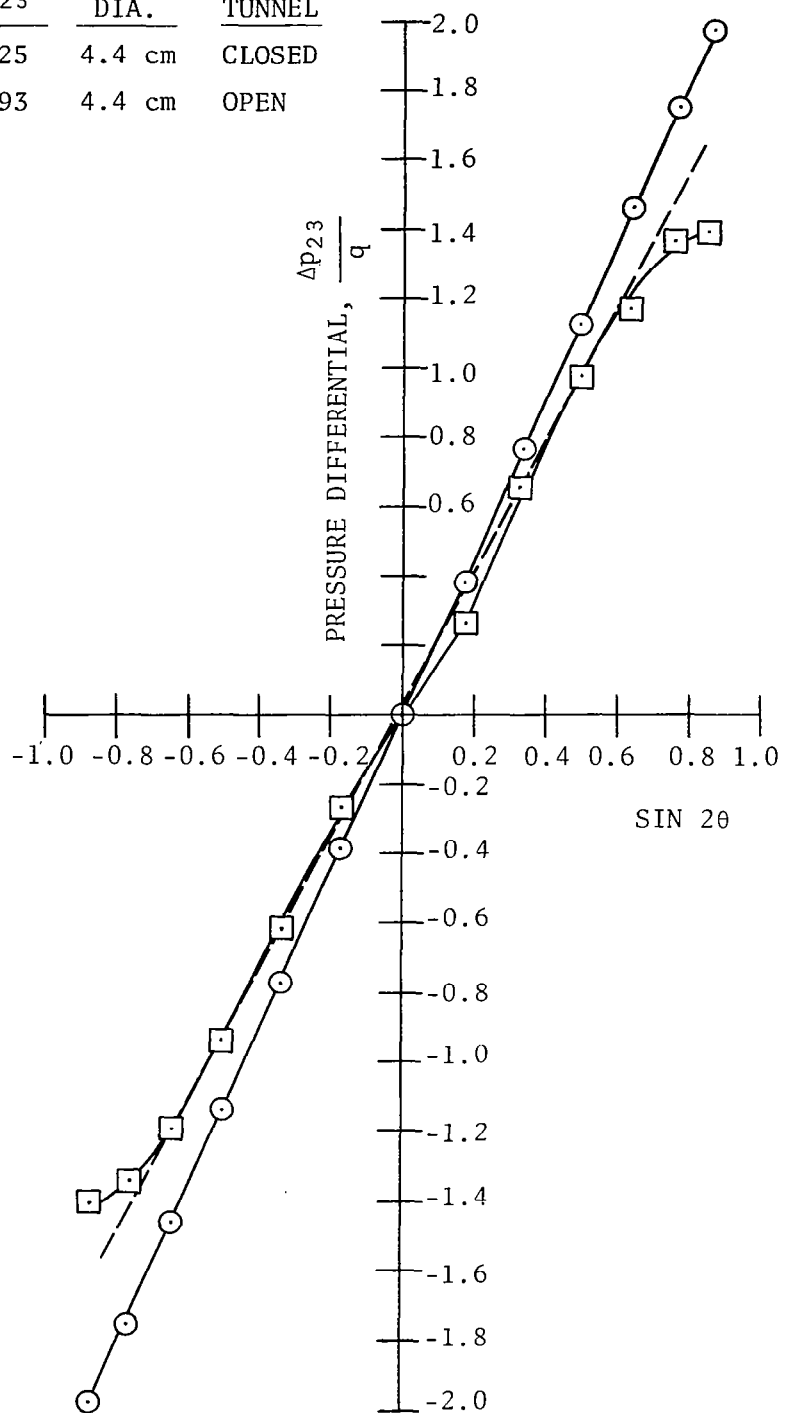


Figure 16. Variation of pressure differential $\Delta P_{23}/q$ with Reynolds number for the 6.35-cm sphere tested in the open and closed wind tunnels with tail attached.

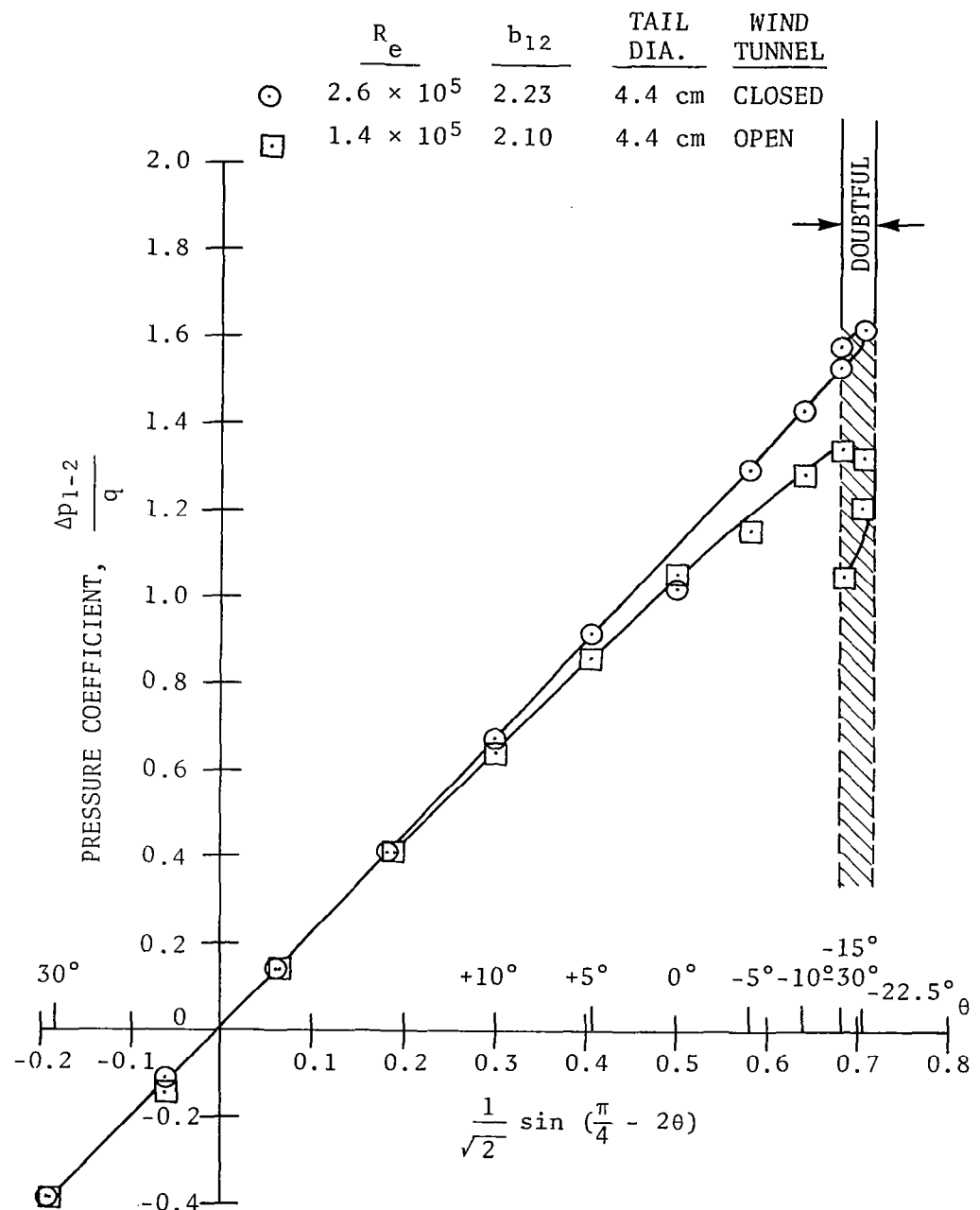
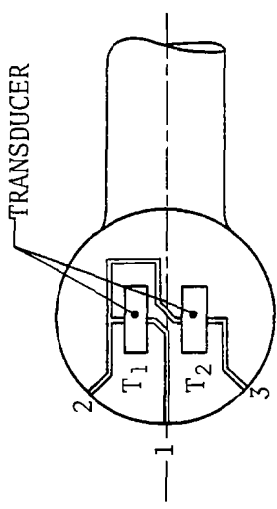
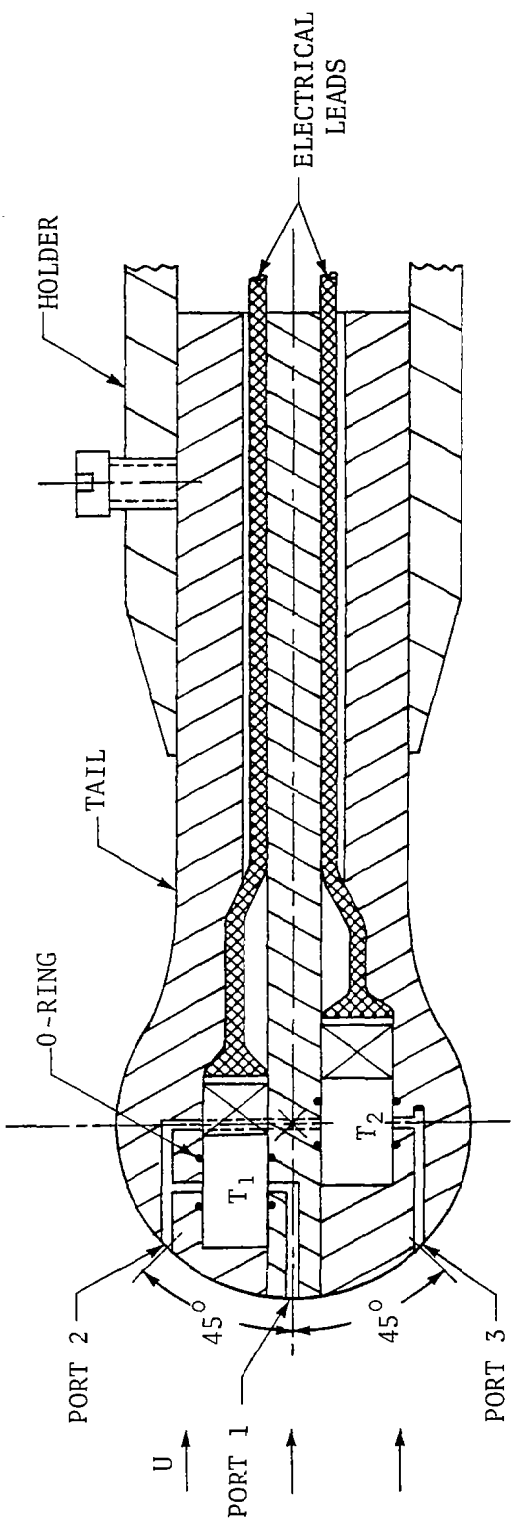


Figure 17. Variation of pressure differential $\Delta p_{12}/q$ with Reynolds number for the 6.35-cm sphere tested in the open and closed wind tunnels with tail attached.



(a) Schematic arrangement of transducers inside spherical head showing ports (1, 2, and 3).



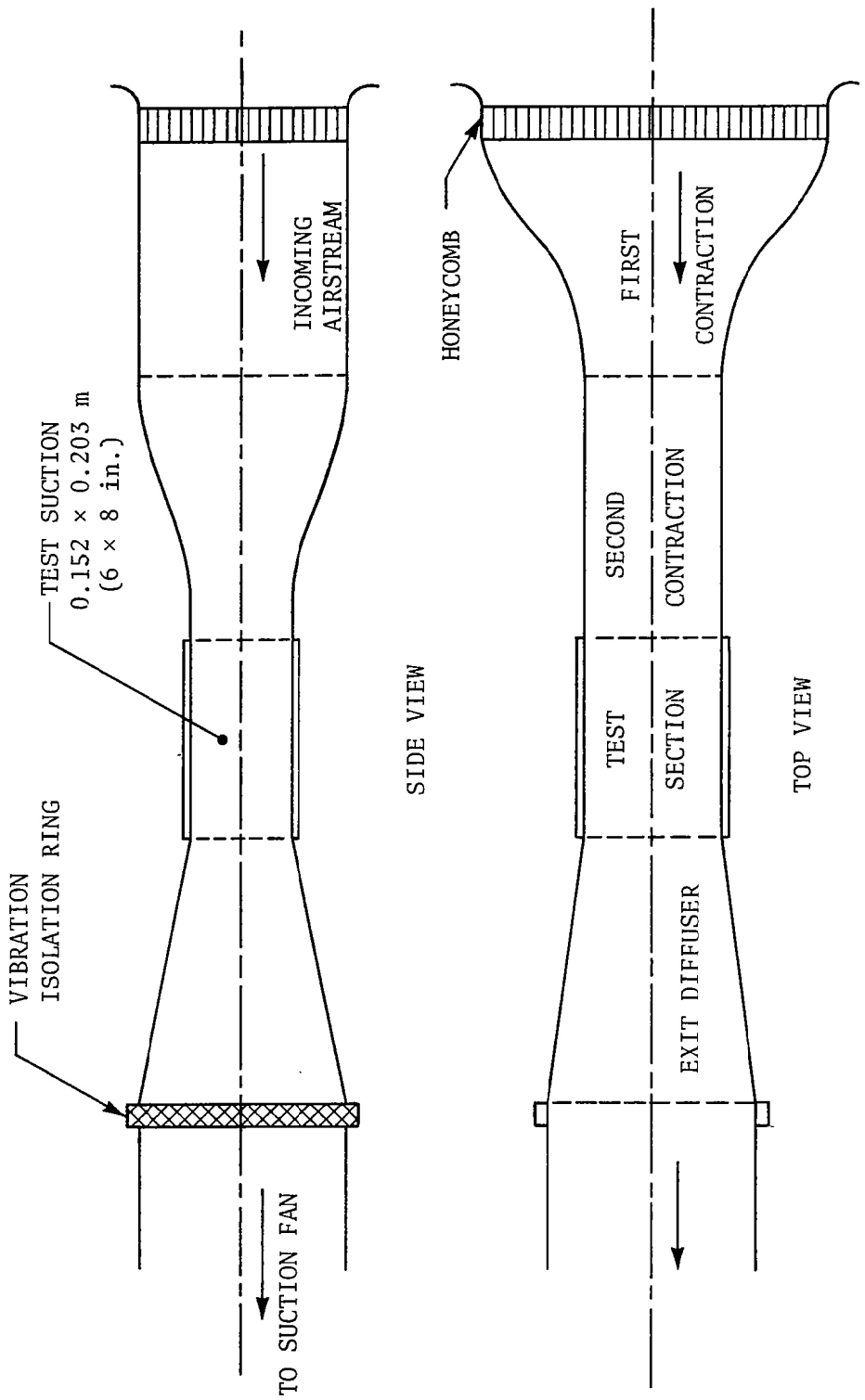
(b) Cross section of spherical head, complete with tail and holder.

Figure 18. Details of sensor design.



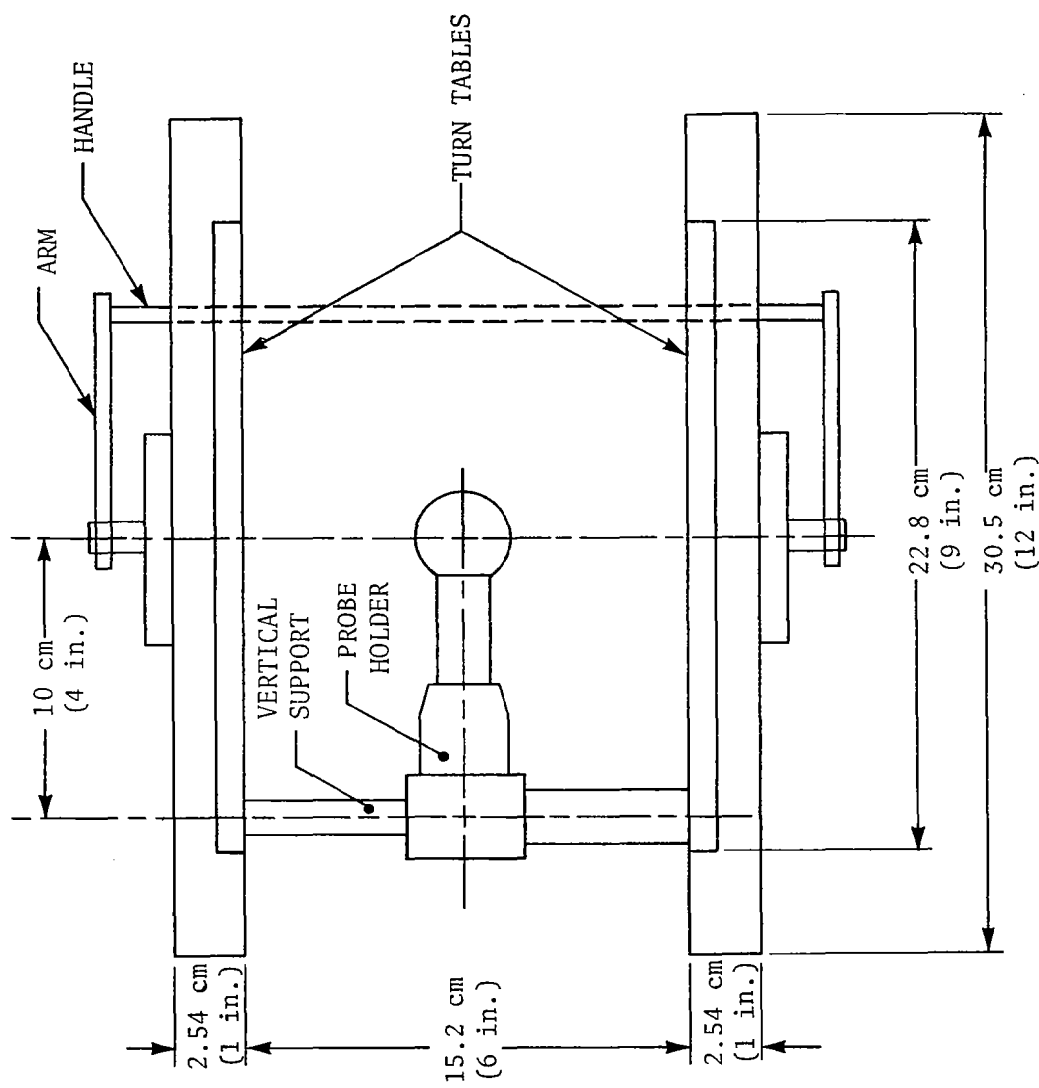
(c) View of the sensor.

Figure 18. (Concluded).



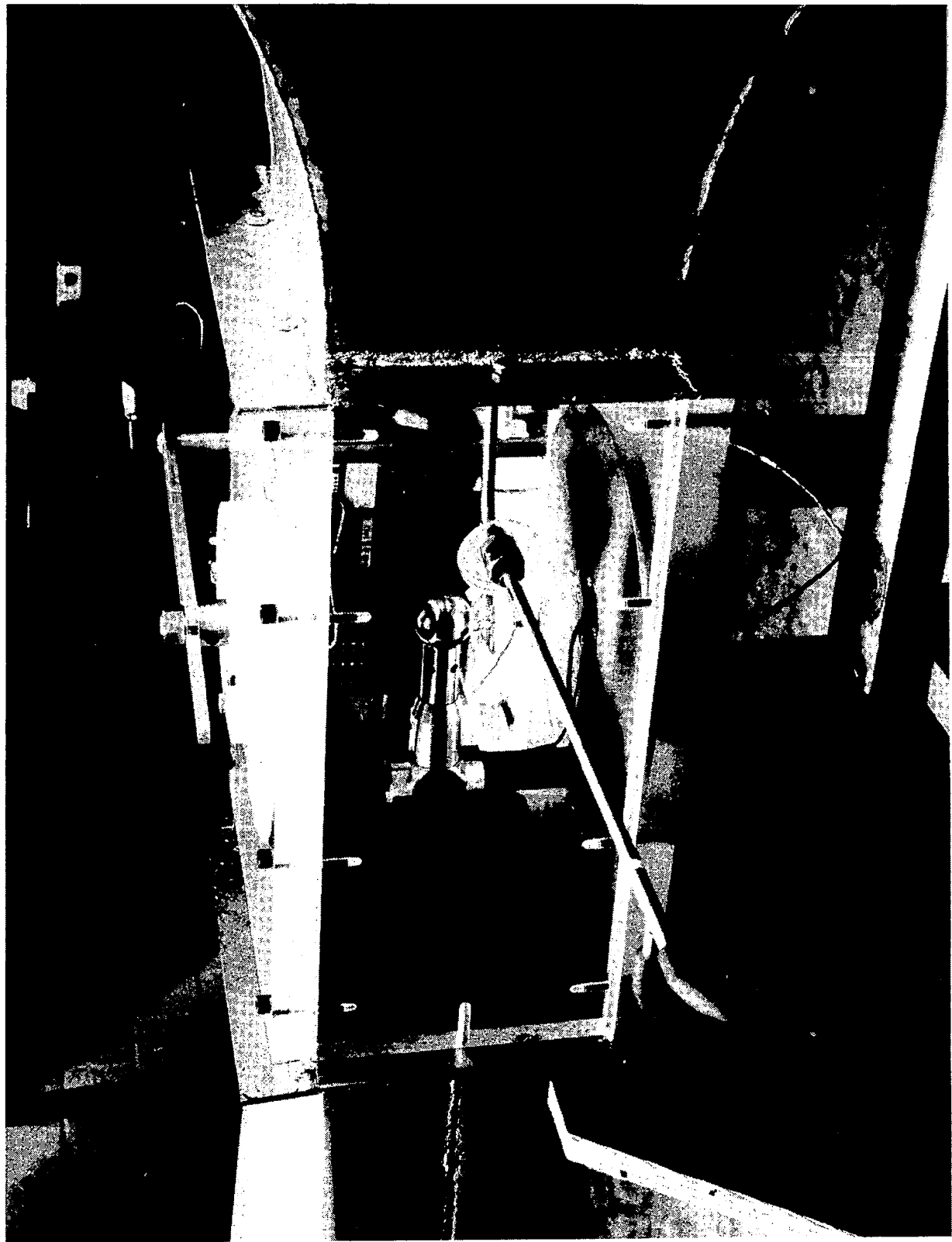
(a) Schematic arrangement of the tunnel.

Figure 19. Design of the induction wind tunnel.



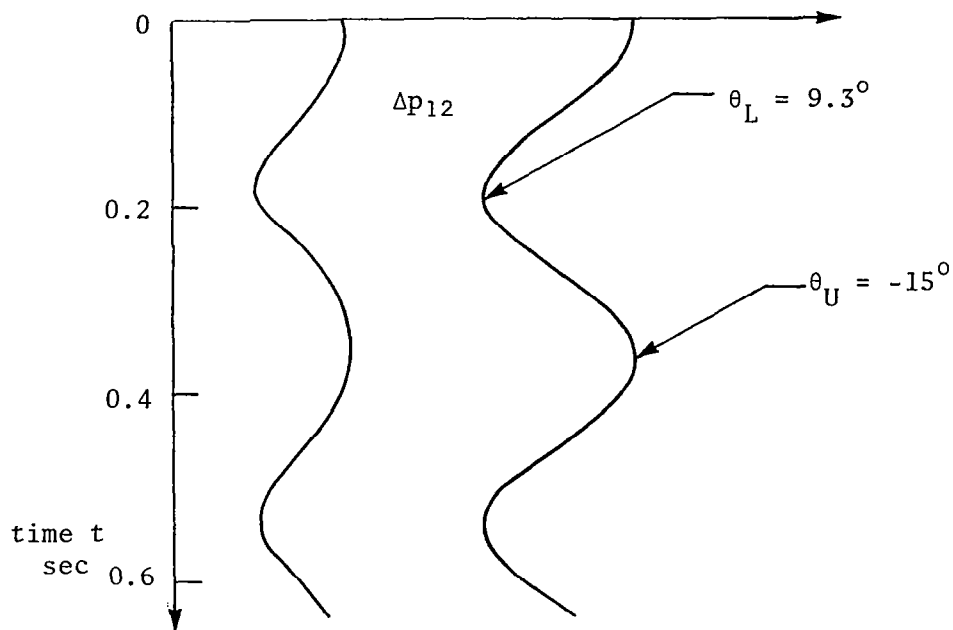
(b) Details of the test section.

Figure 19. (Continued).



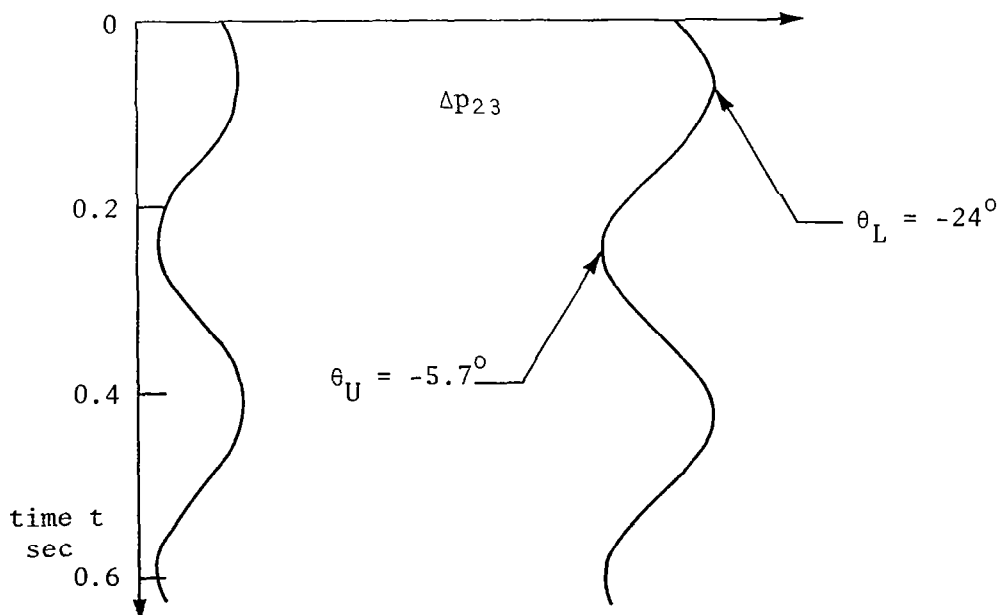
(c) View of sensor setup inside the induction tunnel.

Figure 19. (Concluded).



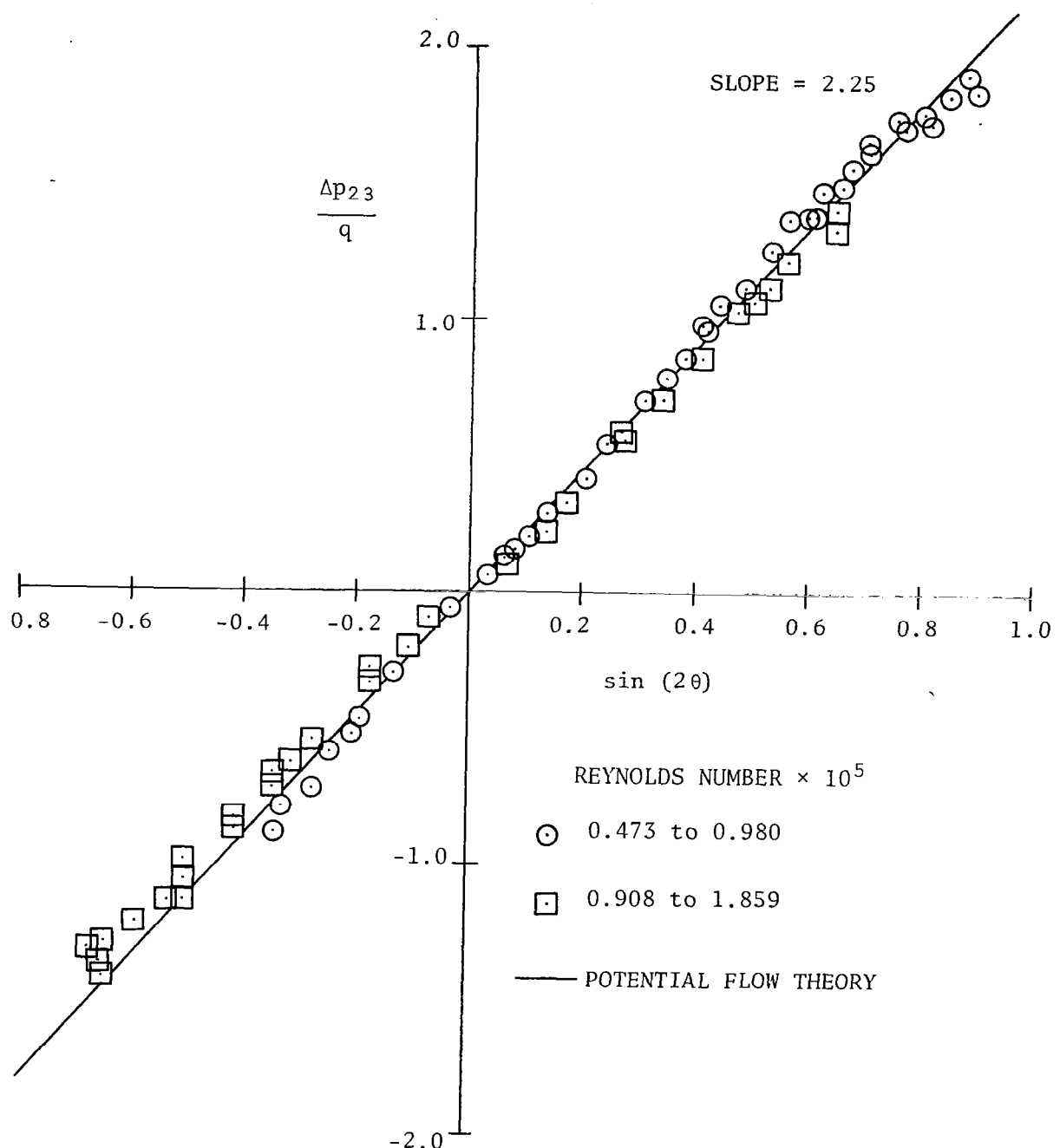
(a) Strip chart output for Δp_{12} .

Airspeed $U = 17.53 \text{ m/s}$, $f = 2.94 \text{ Hz}$.



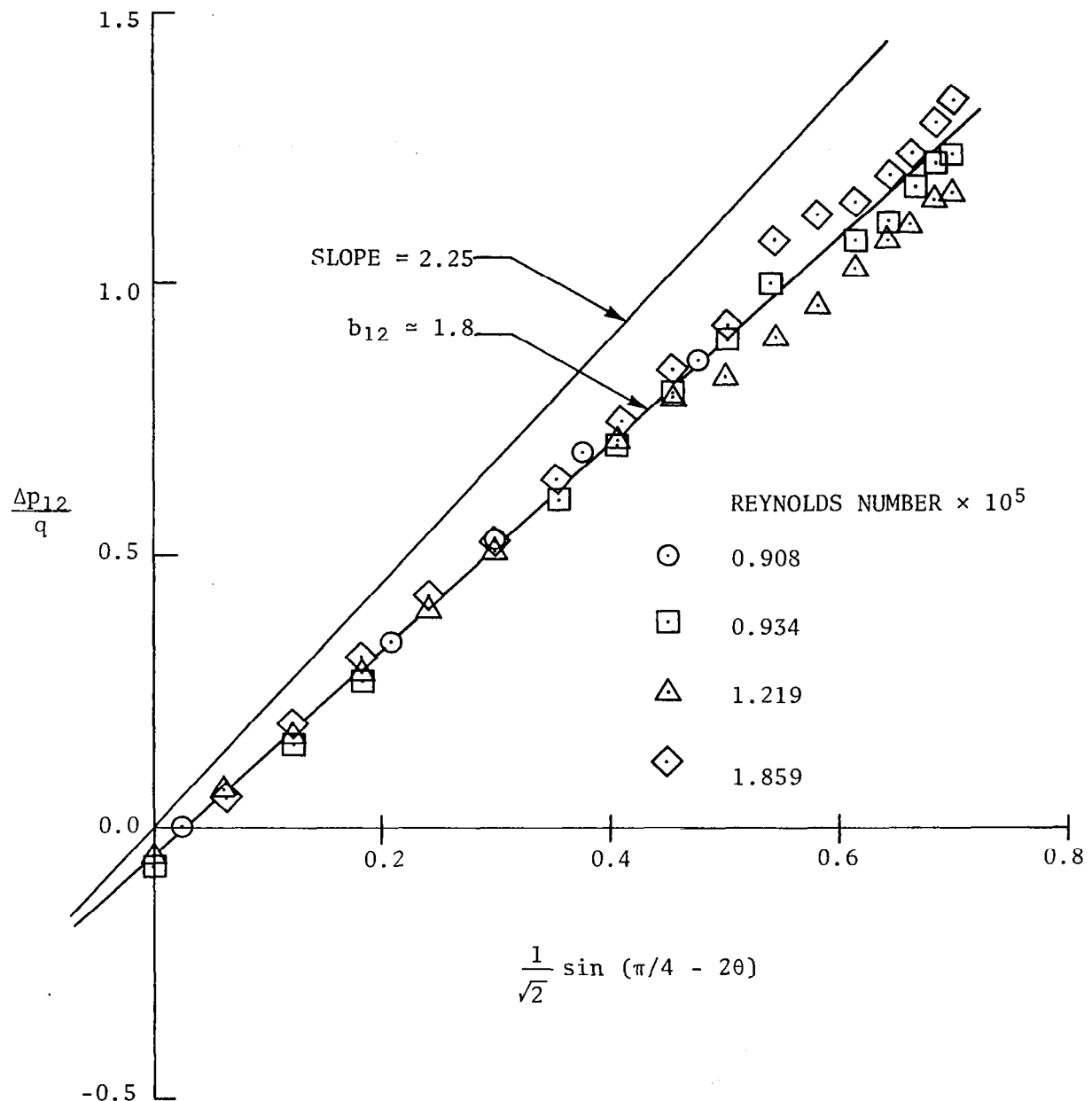
(b) Strip chart output for Δp_{23} .
Airspeed $U = 30.5 \text{ m/s}$, $f = 2.84 \text{ Hz}$.

Figure 20. Samples of observations recorded on strip chart of time-dependent pressure differentials Δp_{12} and Δp_{23} .



(a) Nondimensional pressure differential $\Delta p_{23}/q$.

Figure 21. Variation of pressure differentials with angle of attack and Reynolds number under steady flow conditions.



(b) Nondimensional pressure differential $\Delta p_{12}/q$.

Figure 21. (Concluded).

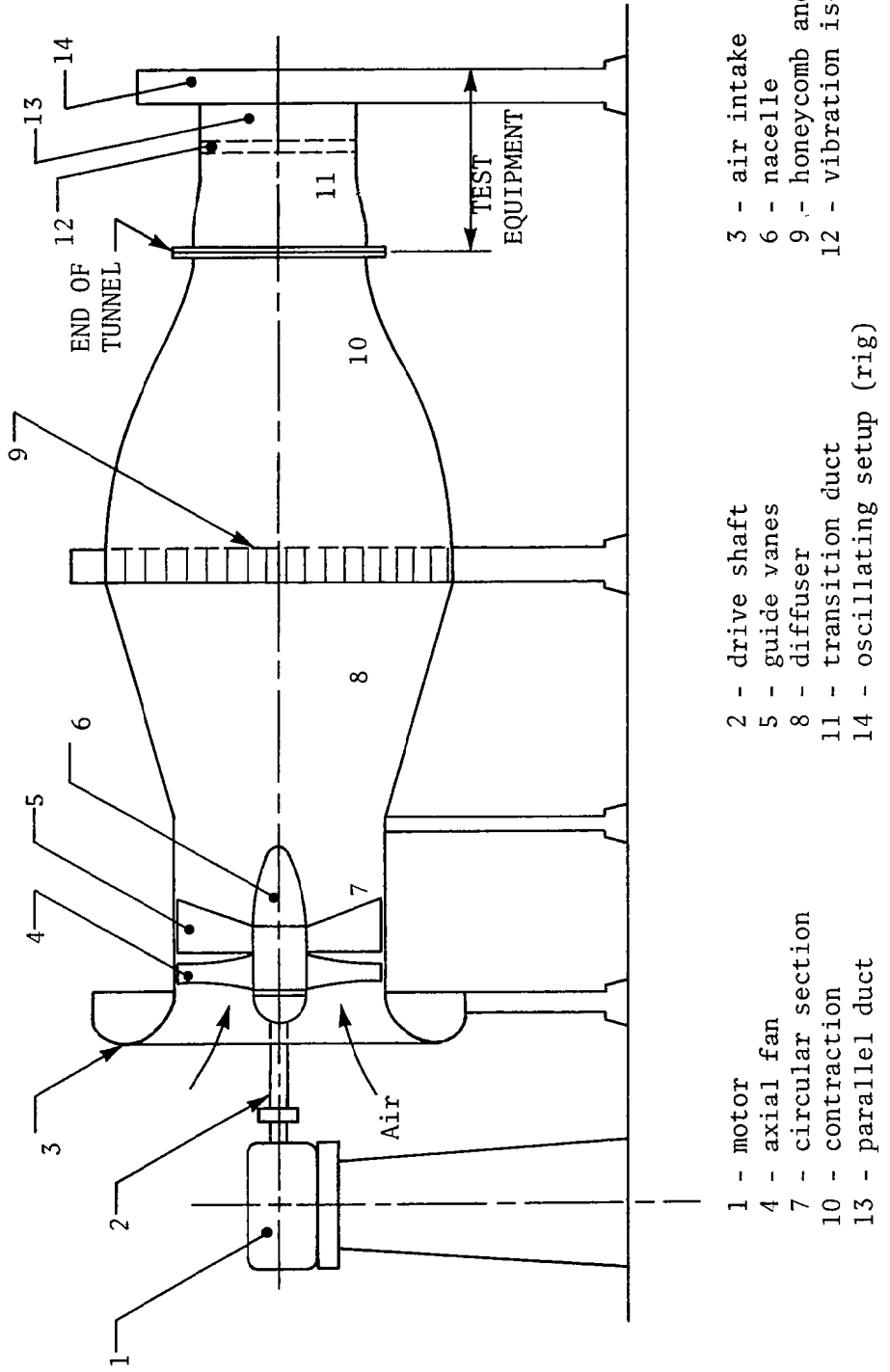


Figure 22. General arrangement of the open-ended wind tunnel and the test equipment.

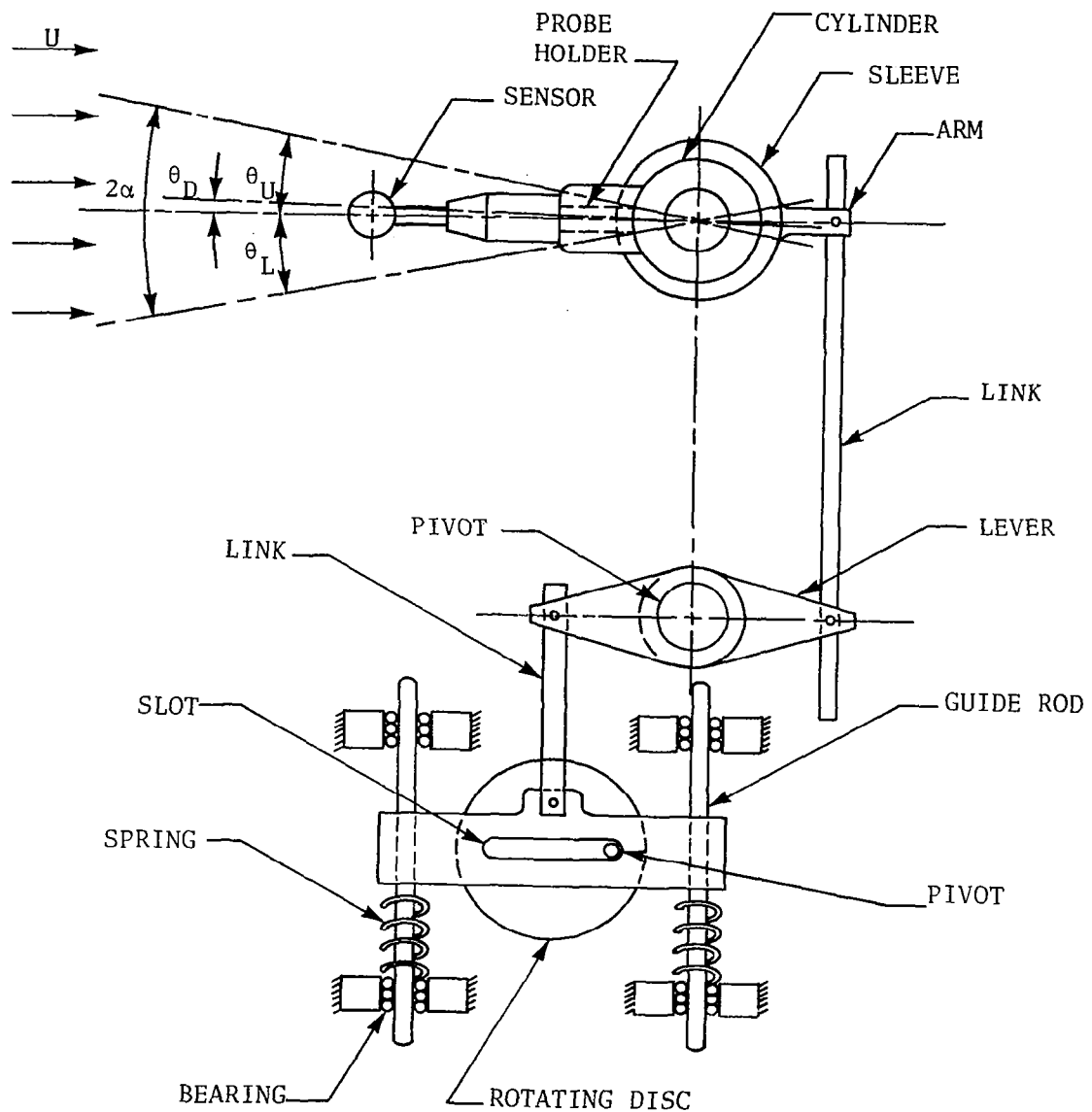


Figure 23. Schematic arrangement of the Scotch Yoke and actuating mechanism for producing oscillating motion.

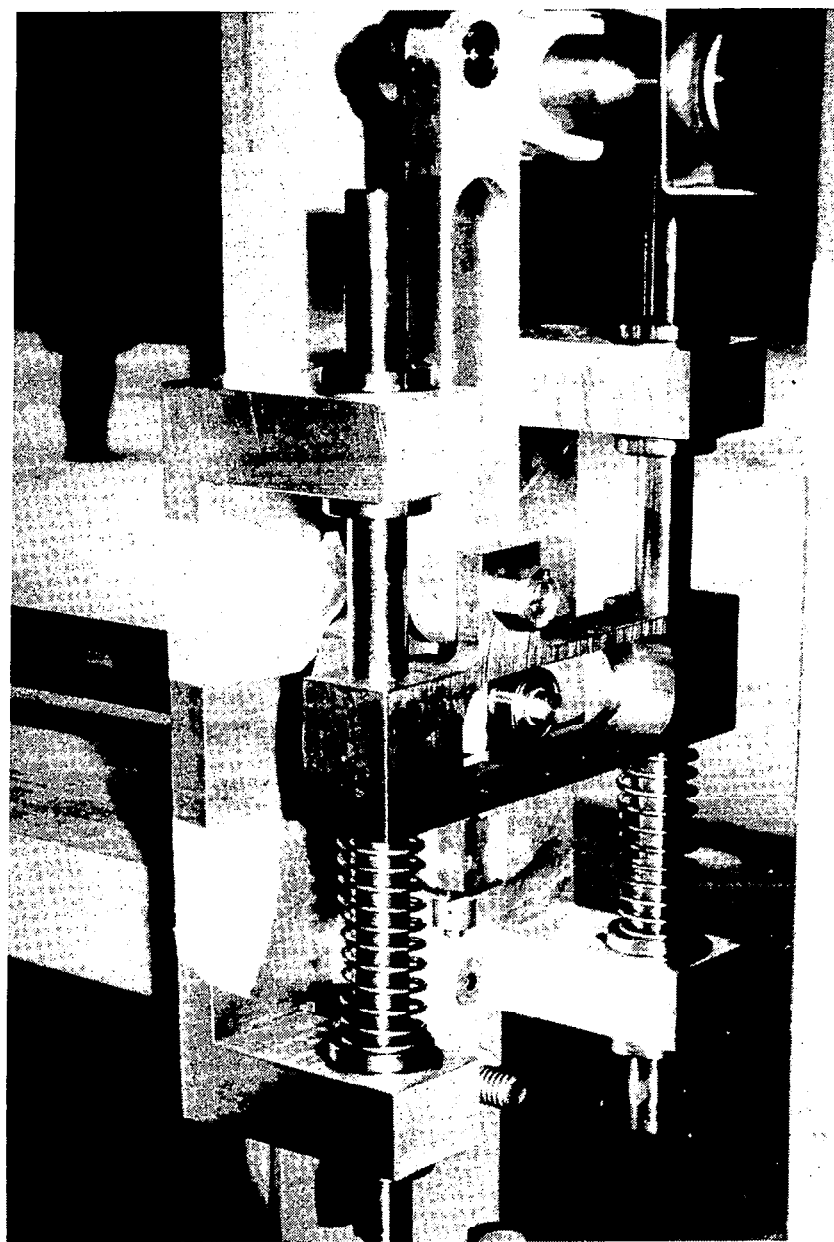


Figure 24. View of the Scotch Yoke mechanism.

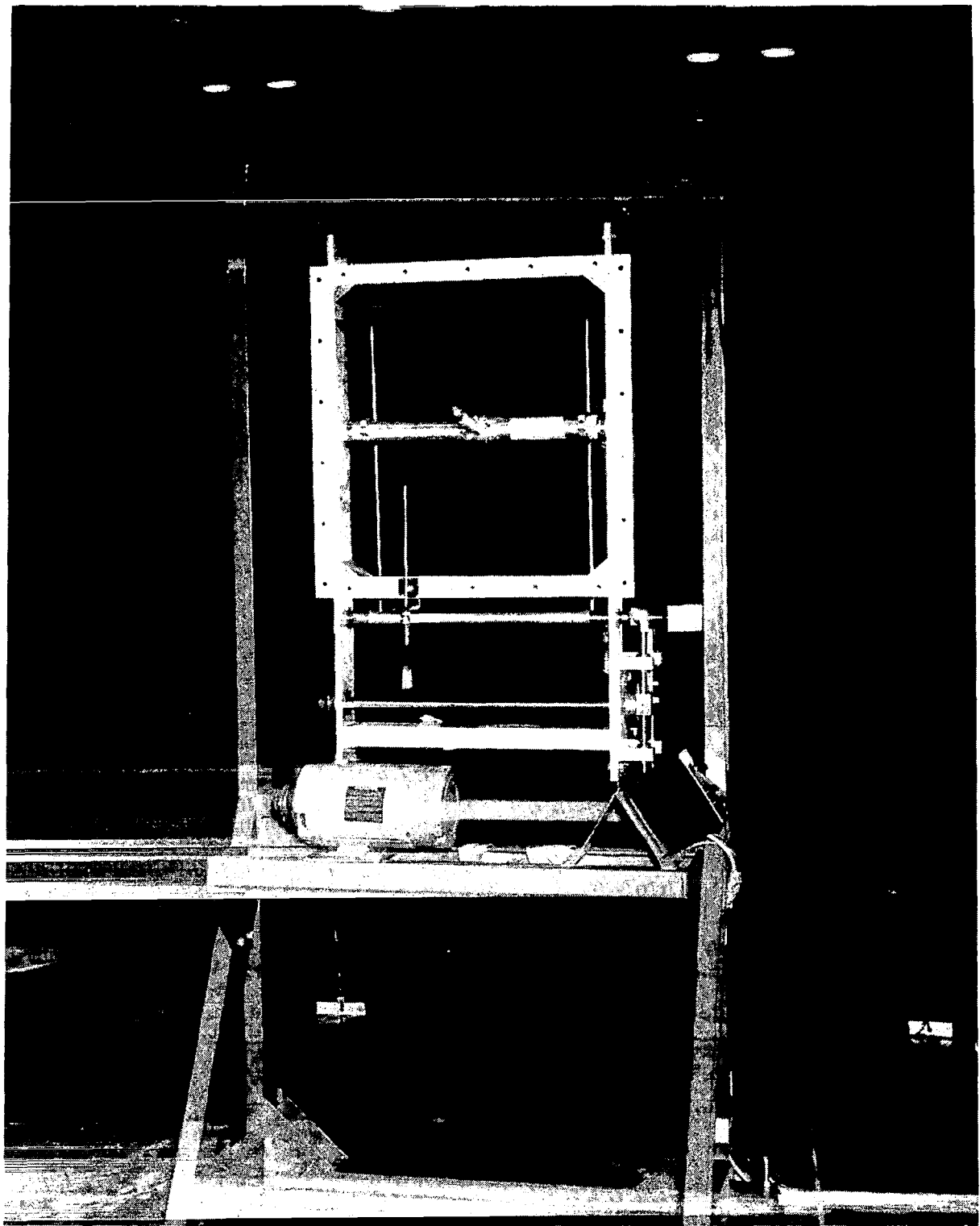


Figure 25. View of the complete test rig fitted to the end of the open wind tunnel.

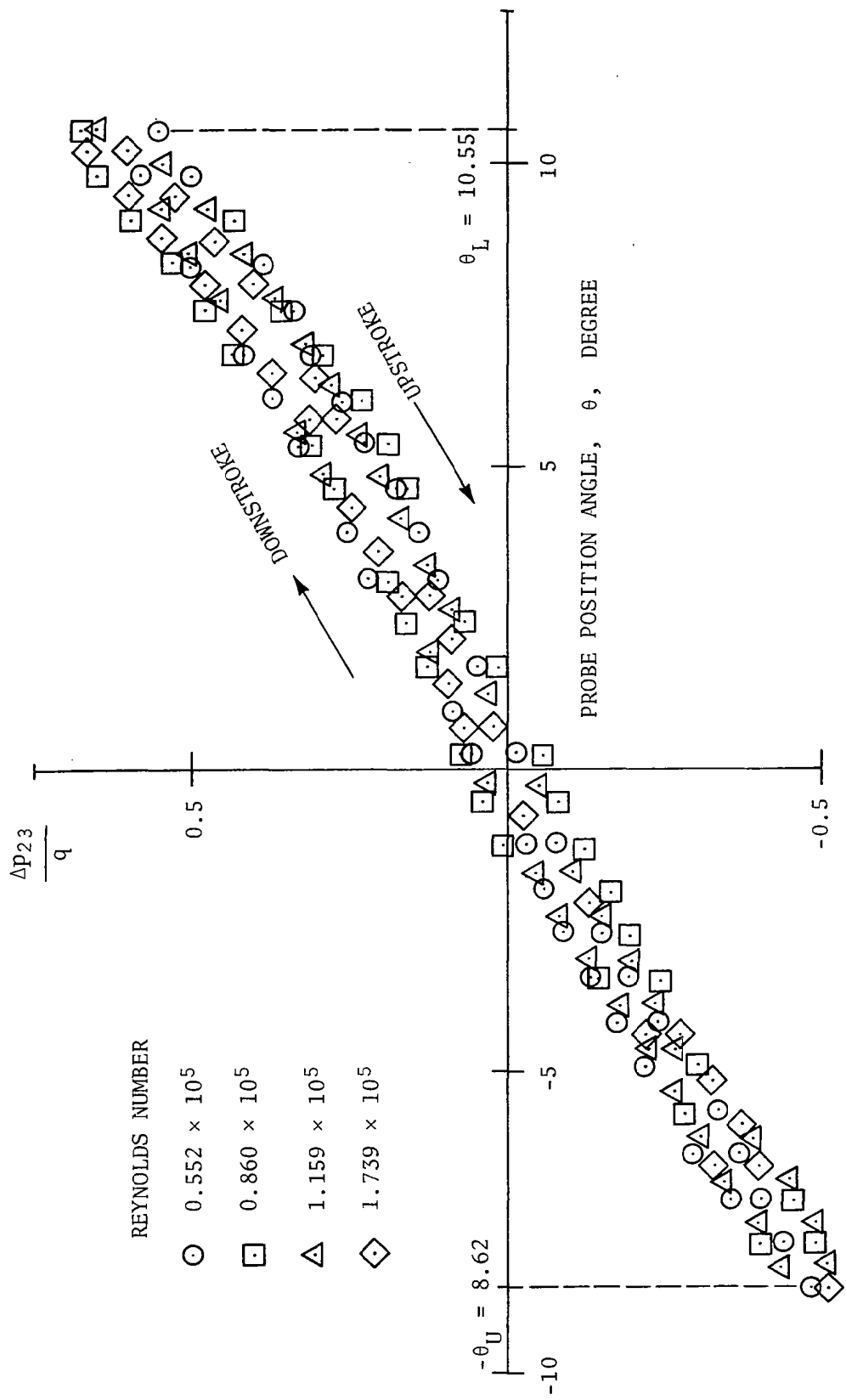
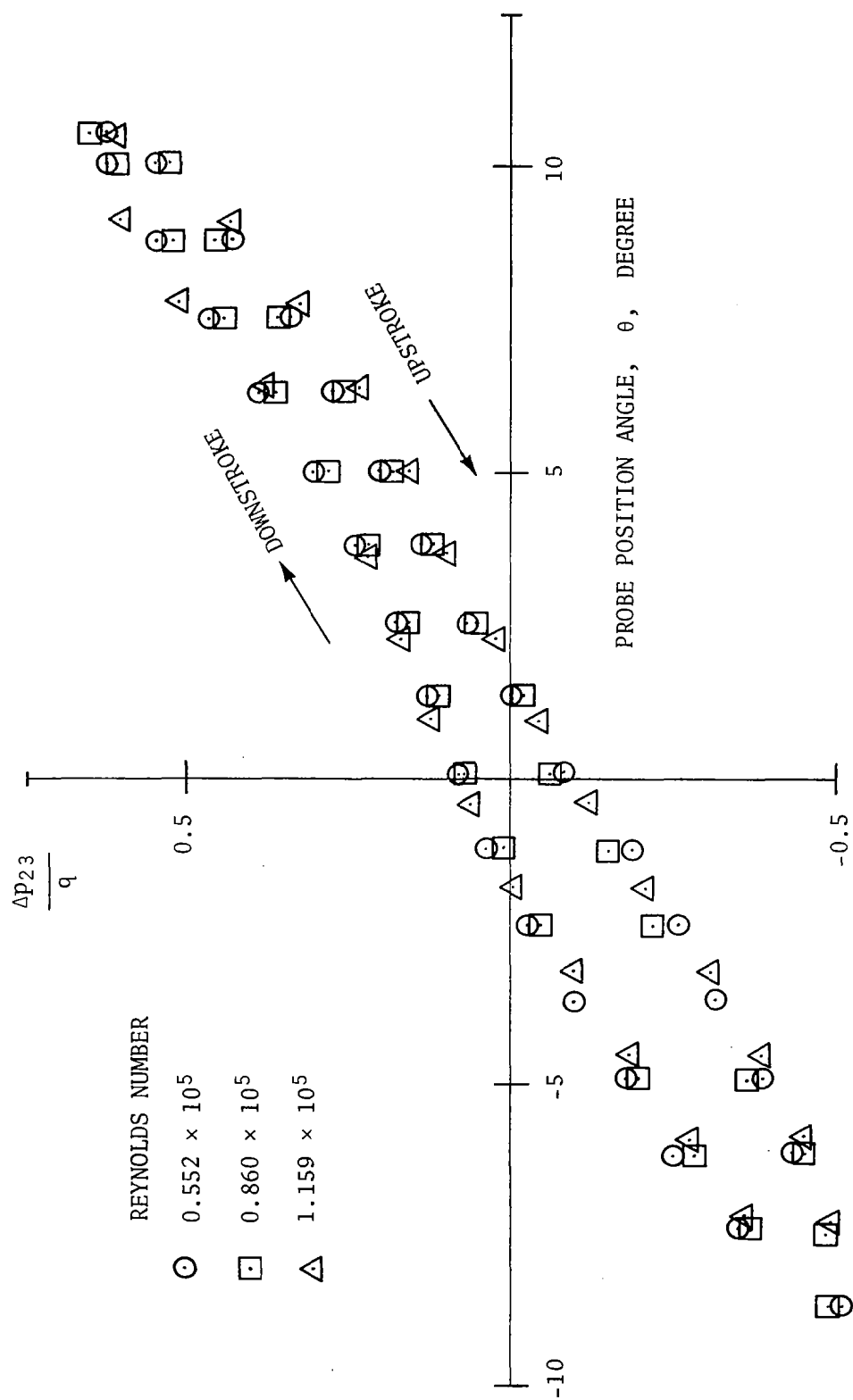
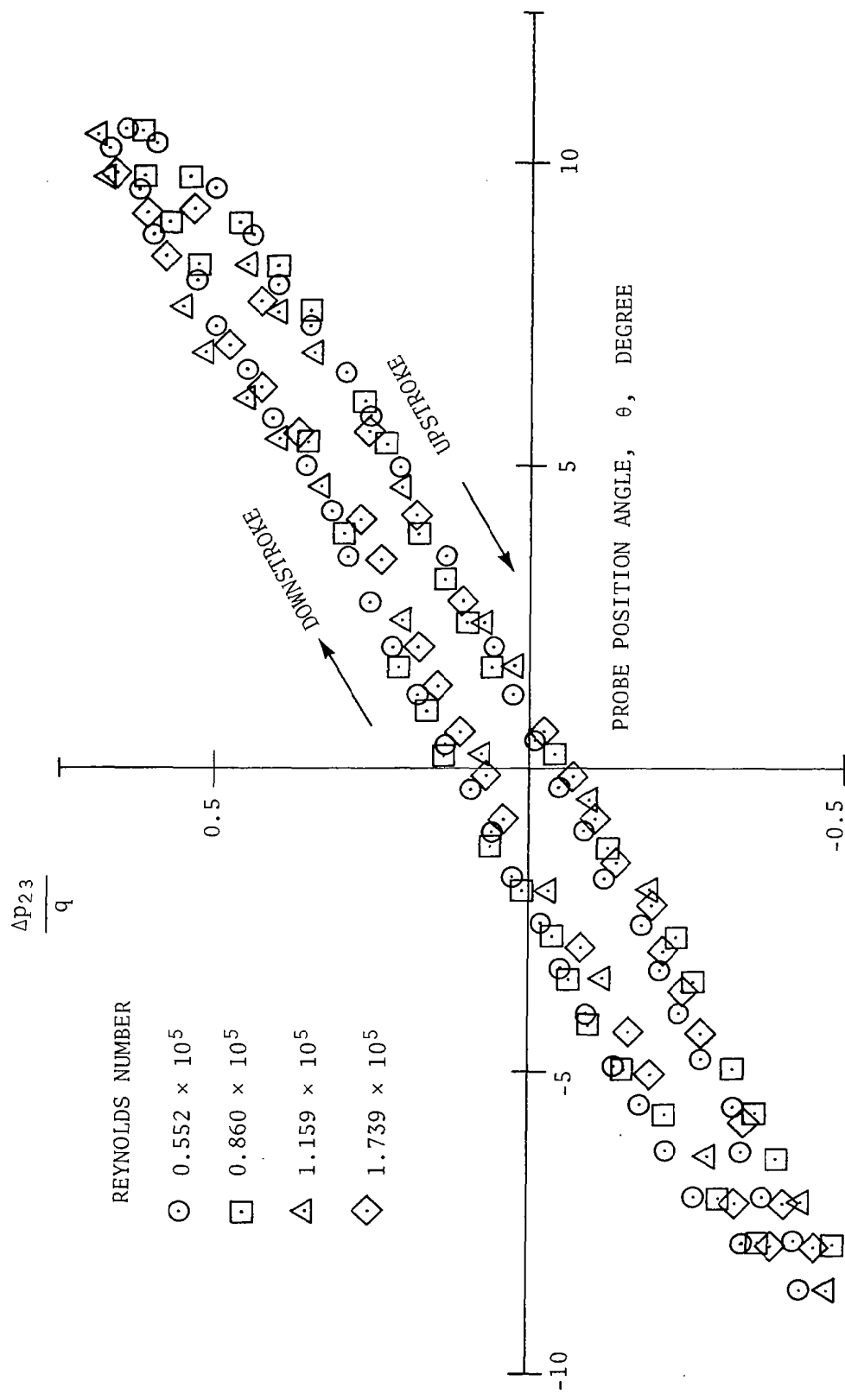
(a) Frequency $f = 1.59$ Hz.

Figure 26. Variation of pressure differential $\Delta p_{23}/q$ during a complete cycle under oscillating sensor motion at a constant frequency and various R_e numbers.



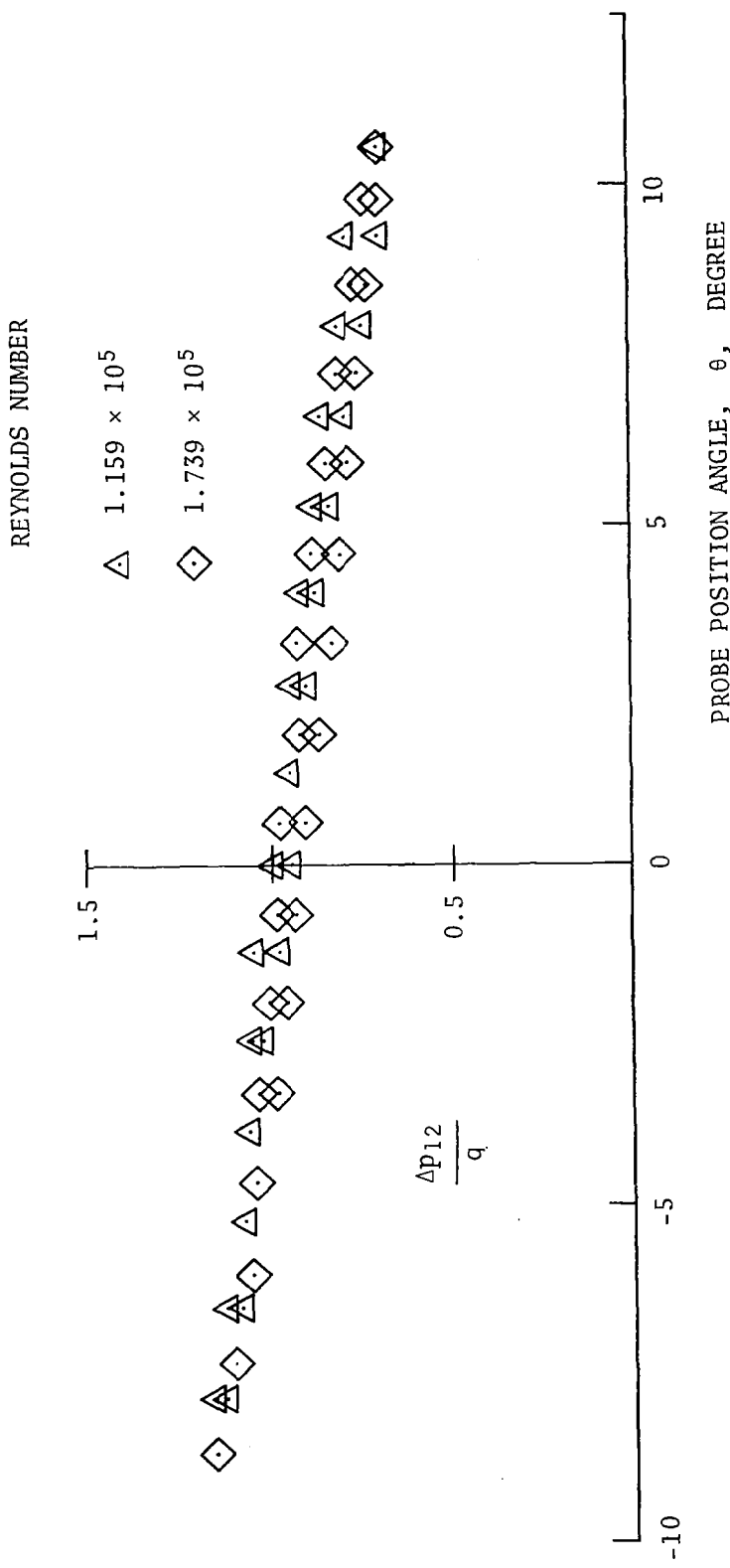
(b) Frequency $f = 2.92$.

Figure 26. (Continued).



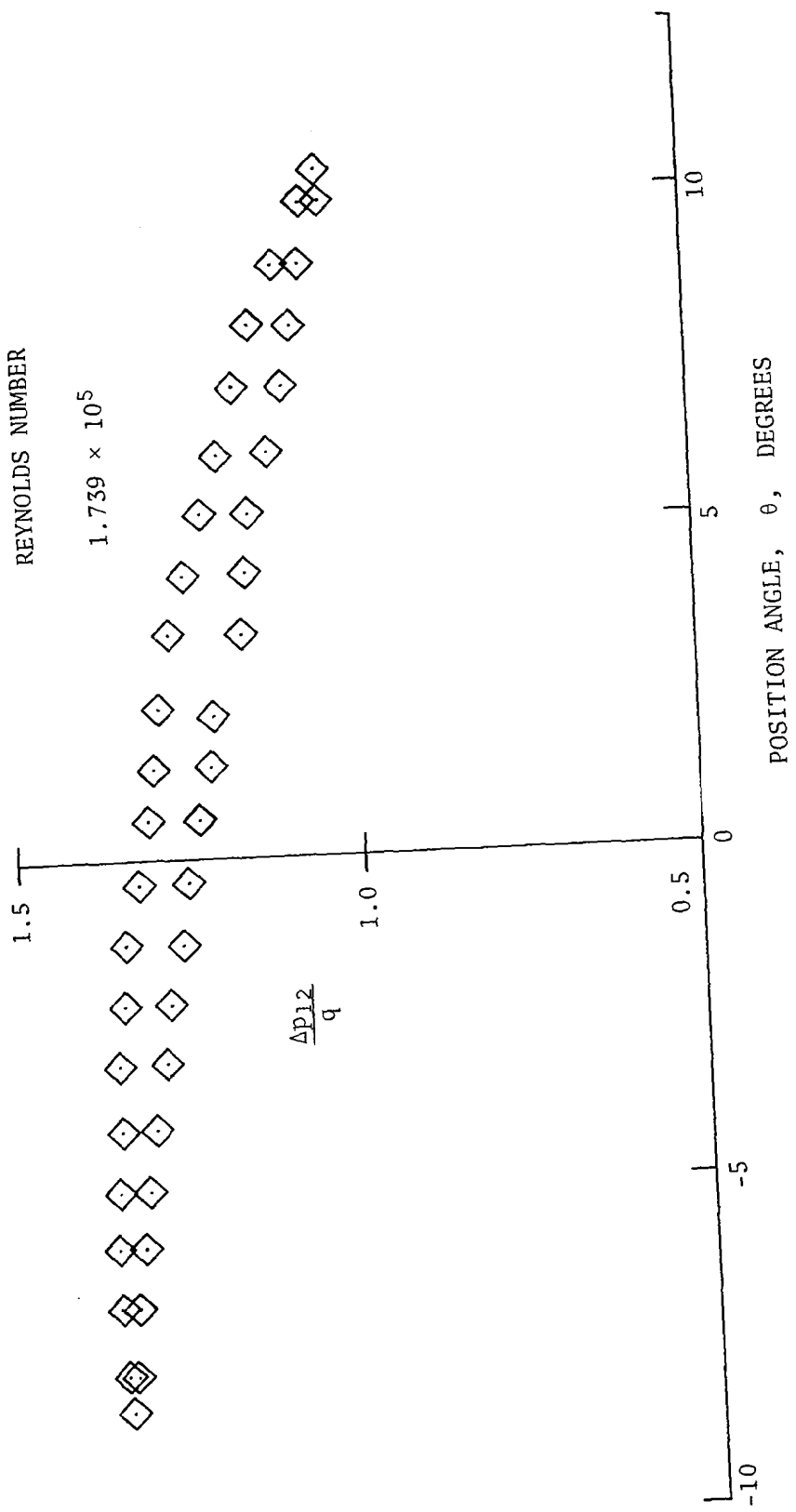
(c) Frequency $f = 3.46$.

Figure 26. (Concluded).



(a) Frequency $f = 2.92$.

Figure 27. Variation of pressure differential $\Delta p_{12}/q$ during a complete cycle under oscillating sensor motion at constant frequency and various R_e numbers.



(b) Frequency $f = 4.81$.

Figure 27. (Concluded).

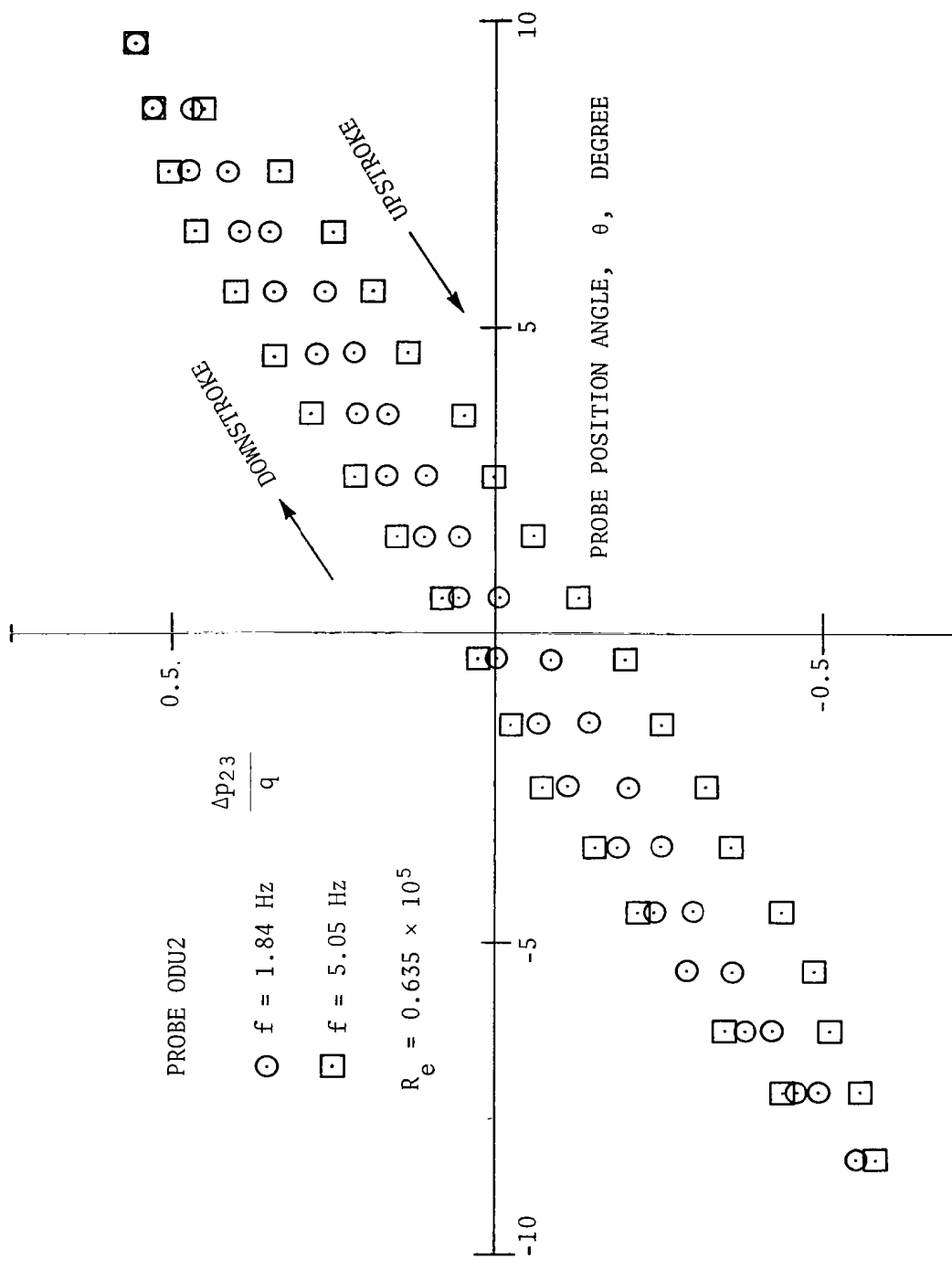
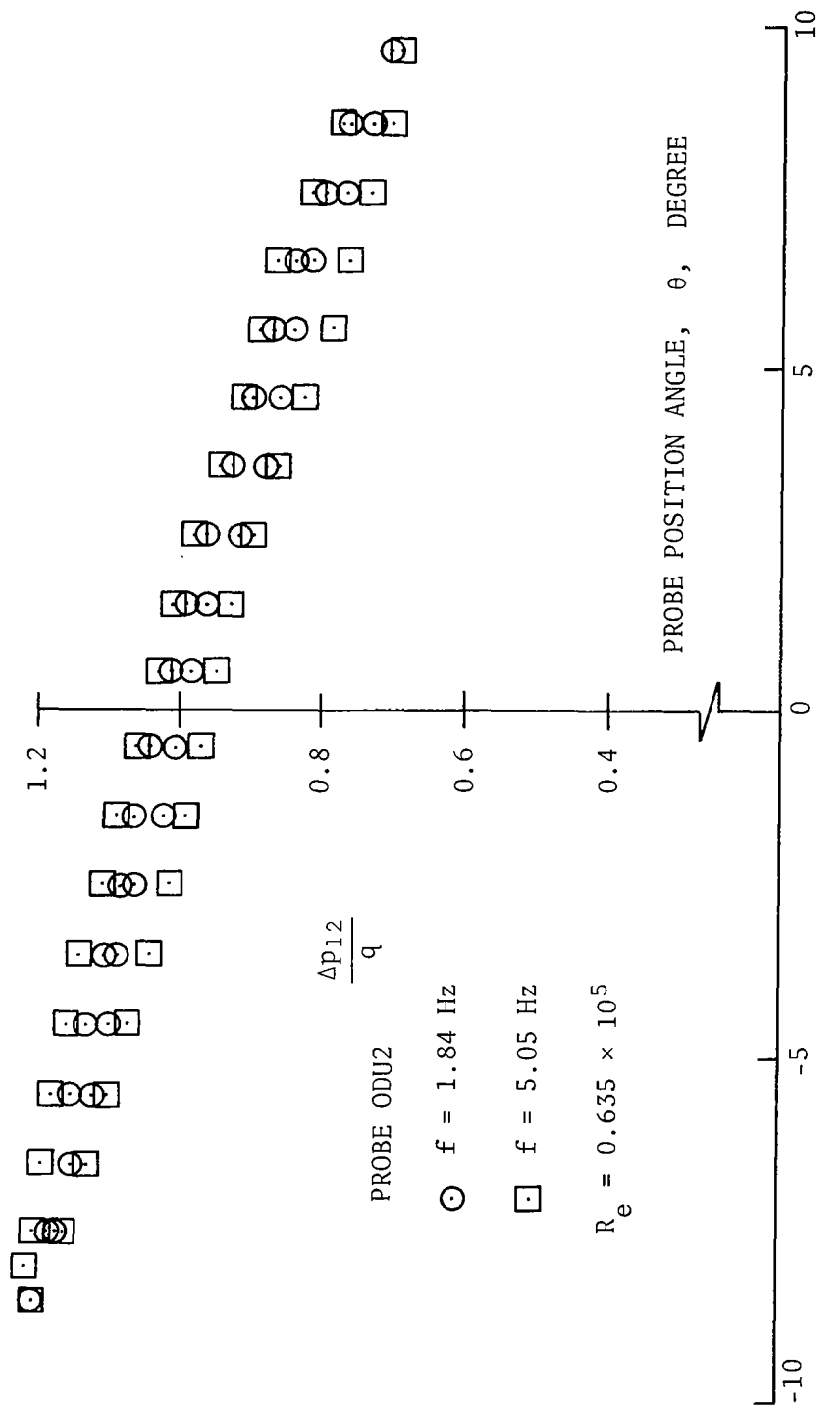


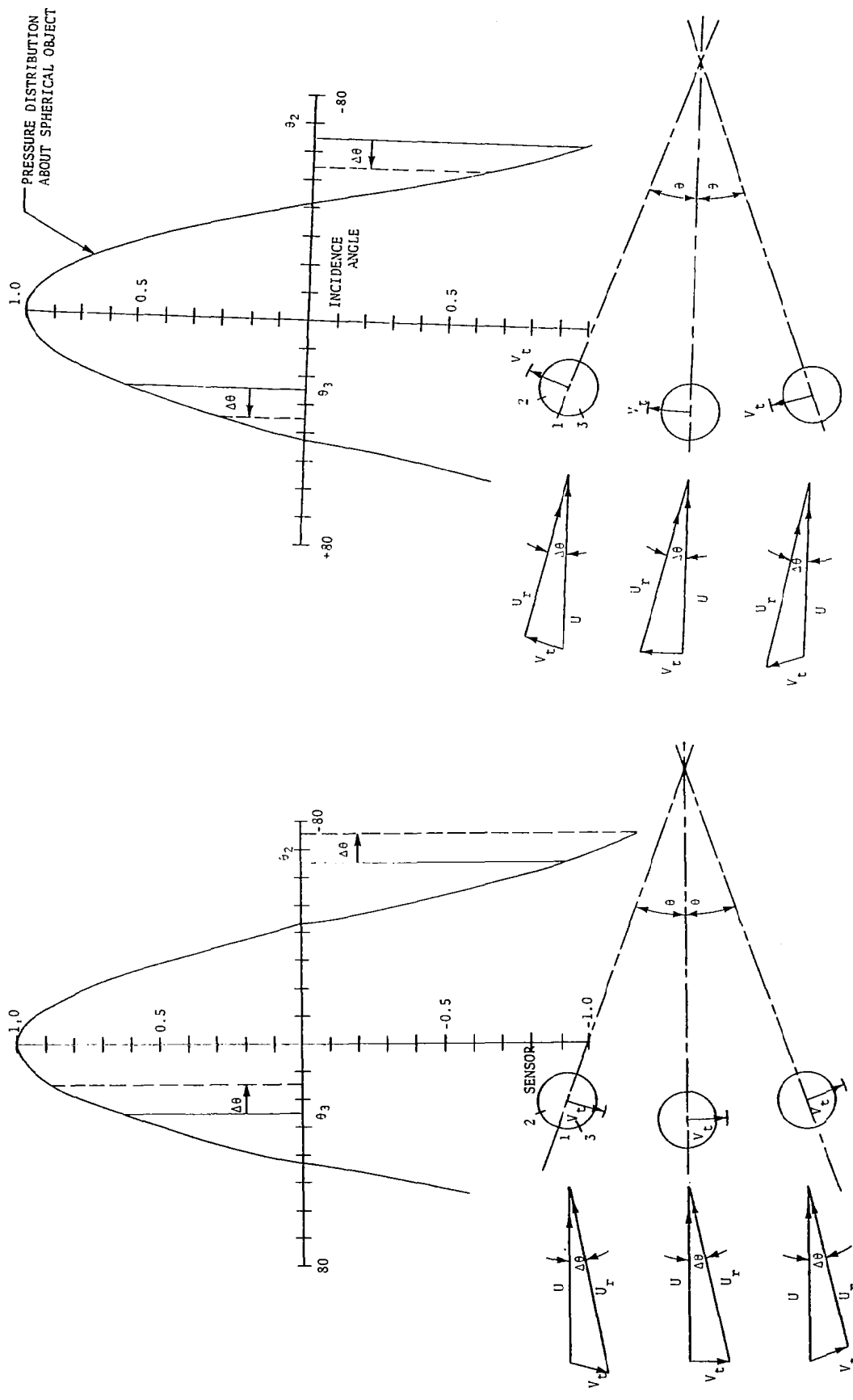
Figure 28. Variation of pressure differentials $\Delta p_{23}/q$ and $\Delta p_{12}/q$ during a complete cycle under oscillating sensor motion at constant Reynolds number $R_e = 0.635 \times 10^5$ and various frequencies.

(a) Pressure differential $\Delta p_{23}/q$.



(b) Pressure differential p_{12}/q .

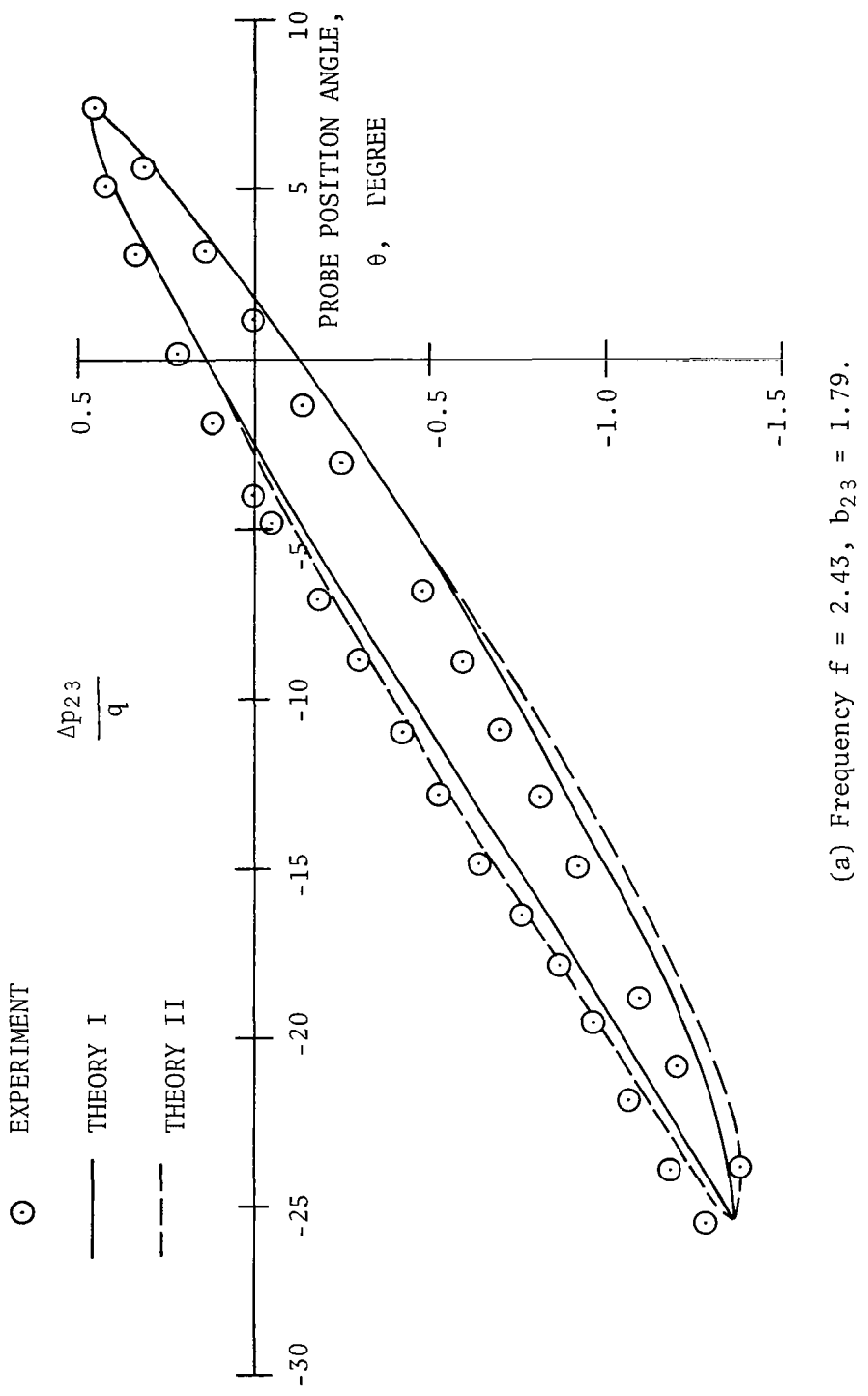
Figure 28. (Concluded).



(a) Superposition of velocity vectors during a down-stroke of sensor.

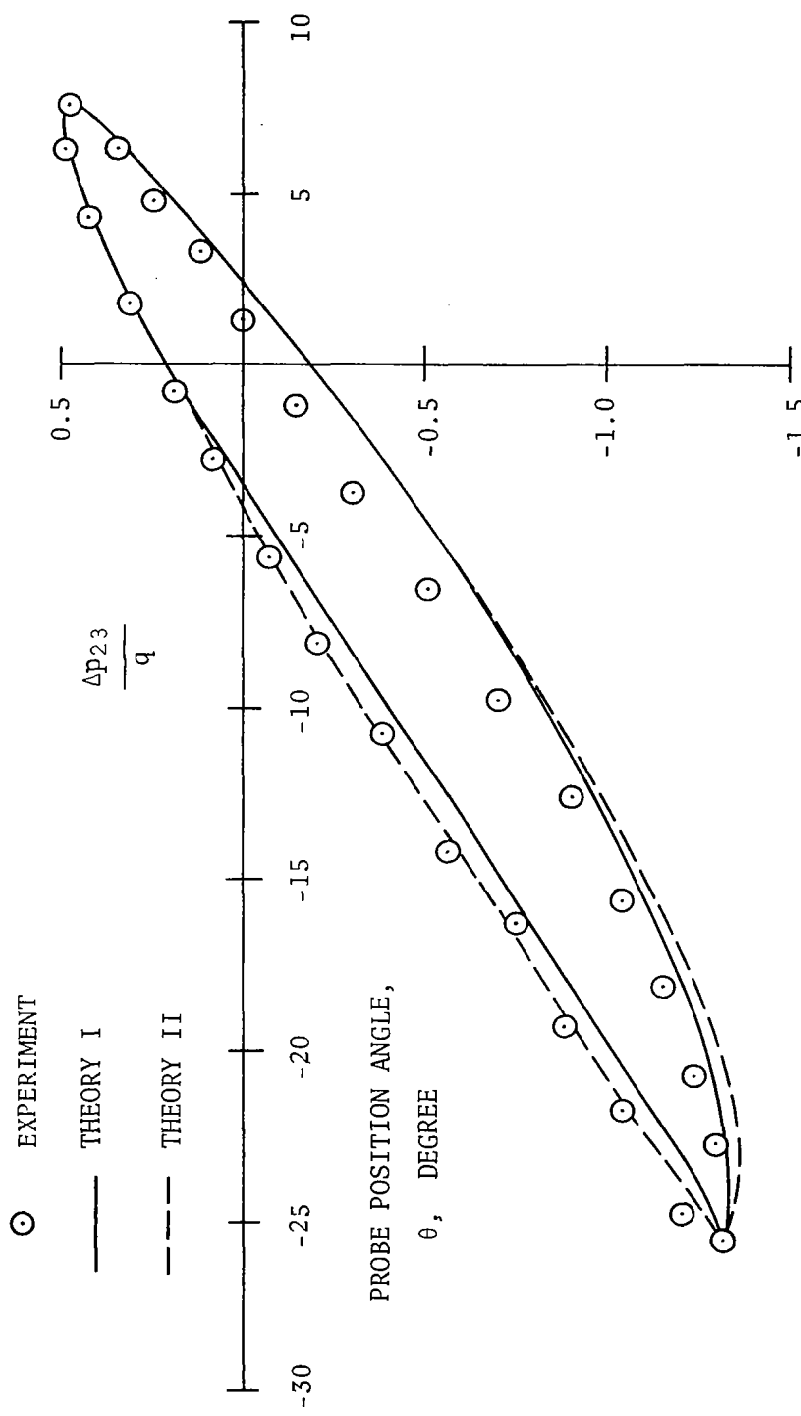
(b) Superposition of velocity vectors during an upstroke of sensor.

Figure 29. Superposition of velocity vectors.



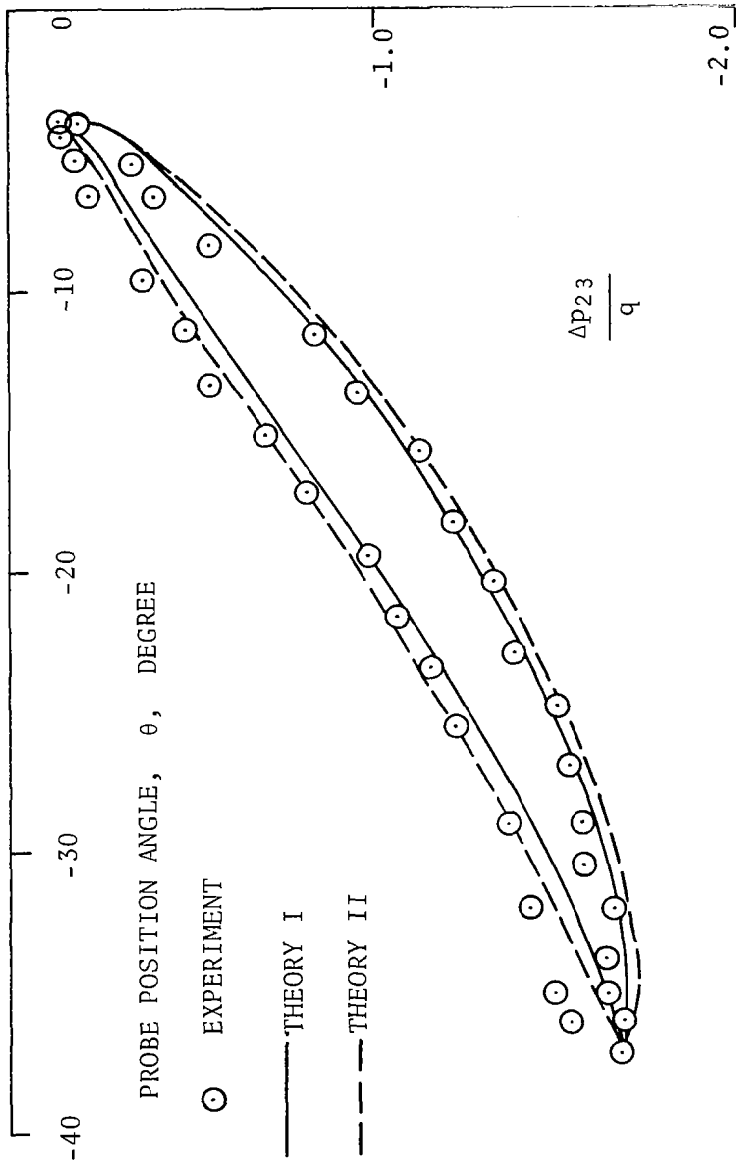
(a) Frequency $f = 2.43$, $b_{23} = 1.79$.

Figure 30. Comparison of experiment with theory of pressure of differential $\Delta p_{23}/q$ during a complete cycle at Reynolds number $R_e = 0.365 \times 10^5$ and assuming $b_{23} = 1.79$.



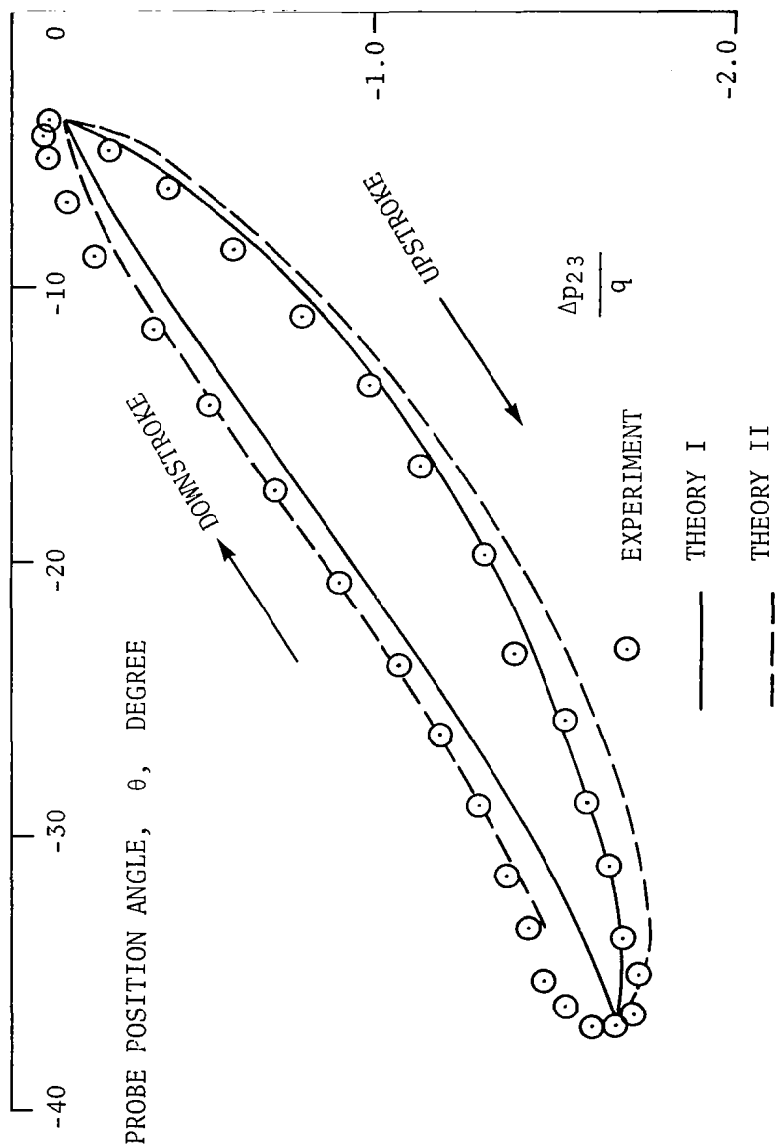
(b) Frequency $f = 3.57$, $b_{23} = 1.79$.

Figure 30. (Concluded).



(a) Frequency $f = 2.72$.

Figure 31. Comparison of experiment with theory of pressure differential P_{23}/q during a complete cycle at Reynolds number $R_e = 0.635 \times 10^5$ assuming $b_{23} = 1.79$ and displacement $\theta = \text{degrees}$.



(b) Frequency $f = 4.03$.

Figure 31. (Concluded).

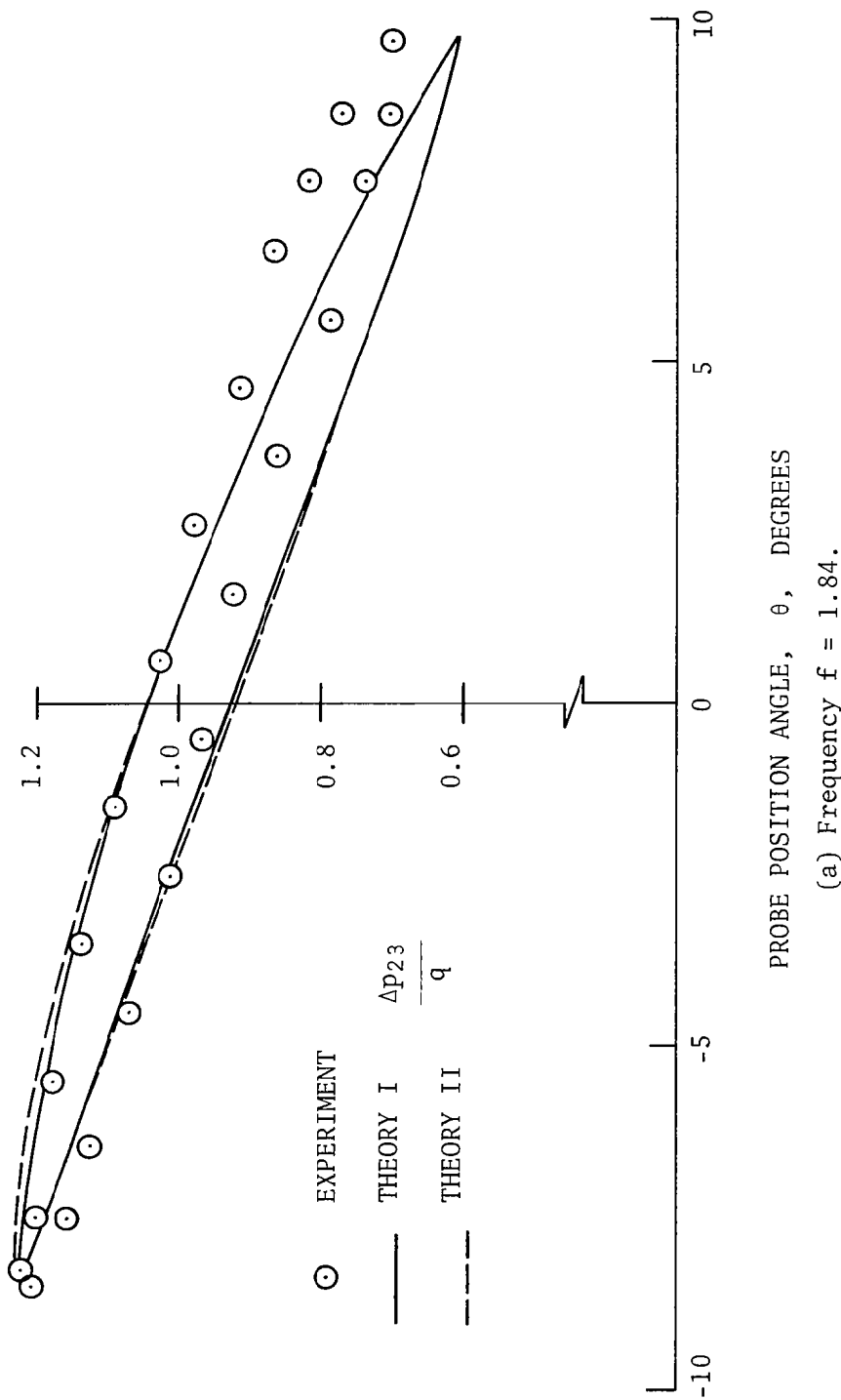
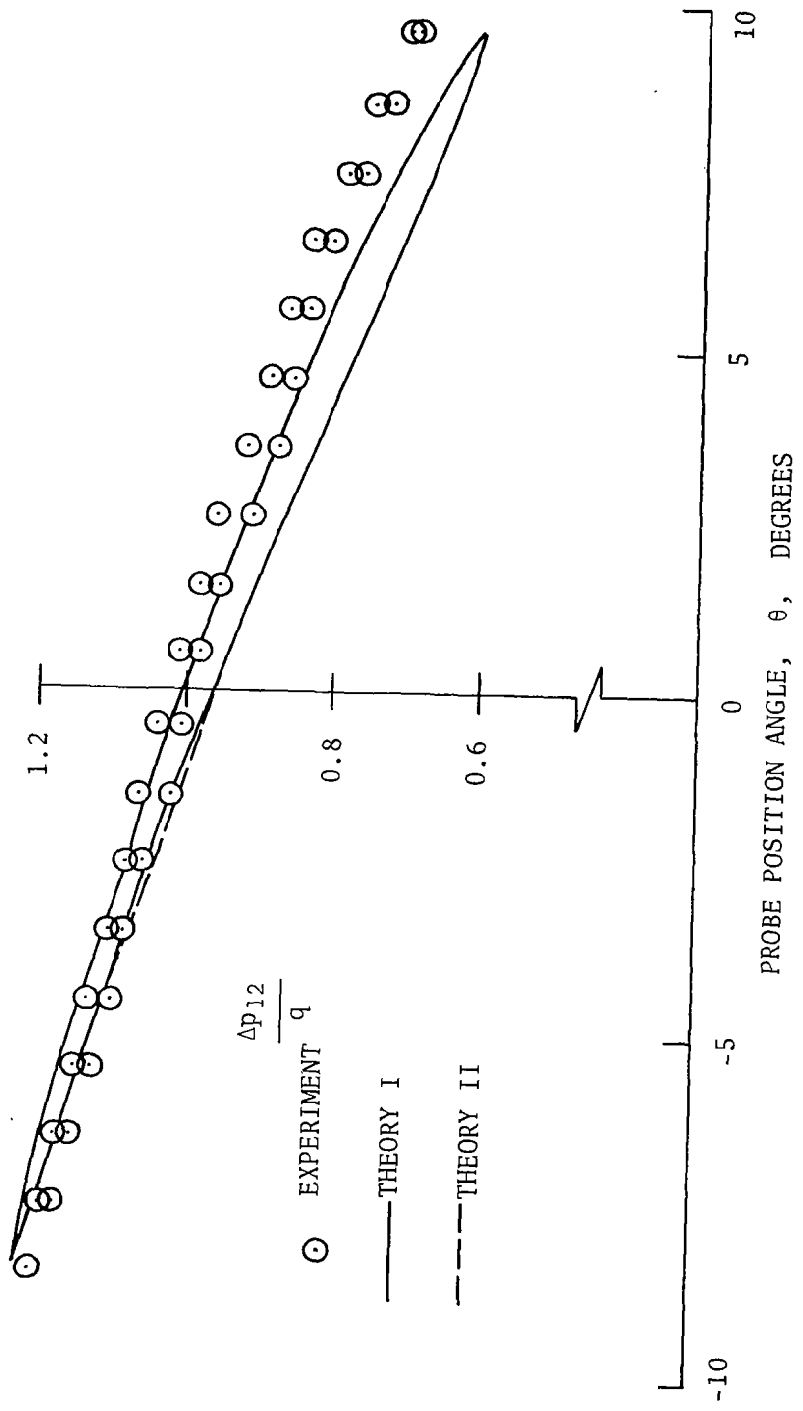


Figure 32. Comparison of experiment with theory of pressure differential $\Delta P_{12}/q$ during a complete cycle at Reynolds number $R_e = 0.635 \times 10^5$ and assuming $b_{12} = 2.03$.



(b) Frequency = 5.05 Hz.

Figure 32. (Concluded).

1. Report No. NASA CR-3297	2. Government Accession No.	3. Recipient's Catalog No.	
4. Title and Subtitle Sensor for Measuring Instantaneous Angle of Attack of Helicopter Blades		5. Report Date June 1980	
7. Author(s) P. S. Barna		6. Performing Organization Code	
9. Performing Organization Name and Address Old Dominion University Research Foundation P. O. Box 6369 Norfolk, Virginia 23665		8. Performing Organization Report No.	
12. Sponsoring Agency Name and Address National Aeronautics and Space Administration Washington, DC 20546		10. Work Unit No.	
15. Supplementary Notes Langley Technical Monitor: David D. Kershner Final Report		11. Contract or Grant No. NSG-1143	
16. Abstract Systematic investigations were performed on a variety of probes to determine their potential for possible application as sensors attached to helicopter blades to measure both the instantaneous angle of attack as well as the dynamic head during actual flight operations. After some preliminary considerations a sensor of essentially spherical shape, about 30 mm in diameter, was designed. The sensor was provided with three pressure ports, and it housed two pressure transducers required for sensing the prevailing pressures acting outside on the surface.		13. Type of Report and Period Covered Contractor Report 1/13/75 - 7/31/79	
The sensors were subsequently tested in the laboratory under a variety of flow conditions to determine their aerodynamic characteristics. Two series of tests were performed: in the first series the sensor was fixed in space while exposed to steady uniform flow, while in the second series the sensor was made to oscillate, thus simulating the cyclic pitch change of the helicopter blades. While the cyclic pitch frequencies were of about the same magnitude as encountered in flight, the flow velocities during tests fell well below those experienced in a rotating blade. The tests showed that the sensors performed satisfactorily under low subsonic flow conditions with frequencies not exceeding five Hz.		14. Sponsoring Agency Code	
17. Key Words (Suggested by Author(s)) Sensor Instantaneous angle of attack under unsteady conditions		18. Distribution Statement Unclassified-unlimited	
Subject Category 06			
19. Security Classif. (of this report) Unclassified	20. Security Classif. (of this page) Unclassified	21. No. of Pages 81	22. Price* \$6.00

* For sale by the National Technical Information Service, Springfield, Virginia 22161

NASA-Langley, 1980